

Modelling of Liquid Droplet Dynamics in a High DC Magnetic Field

Stuart Easter

Centre for Numerical Modelling and Process Analysis
School of Computing and Mathematical Sciences
University of Greenwich

A thesis submitted in partial fulfilment of the
requirements of the University of Greenwich
for the degree of Doctor of Philosophy

February 2012

Declaration

I certify that this work has not been accepted in substance for any degree, and is not concurrently being submitted for any degree other than that of Doctor of Philosophy being studied at the University of Greenwich. I also declare that this work is the result of my own investigations except where otherwise identified by references and that I have not plagiarised the work of others.

.....

Stuart Easter (Author)

Date:

.....

Dr. Valdis Bojarevics (Supervisor)

Date:

.....

Prof. Koulis Pericleous (Supervisor)

Date:

Acknowledgements

I would like to thank my supervisors Dr. Valdis Bojarevics and Prof. Koulis Pericleous for their advice, encouragement, and guidance throughout my PhD.

I would like to acknowledge the School of Computing and Mathematical Sciences for providing the funding for the initial three years of my research and I would like to thank my parents for the financial support provided by them in the remaining time it took to complete my thesis.

Abstract

The oscillating droplet technique is an experimental technique that is used to measure the surface tension and viscous damping coefficients of a liquid droplet. This technique has been the subject of much analysis; theoretical, numerical, and experimental with a number of different external forces used to confine the droplet. These external forces are found to modify the oscillation frequency and damping rates, which need to be quantified in order for the measurement technique to be used. The dynamics of the droplet are three-dimensional but previous numerical work has largely focused on axisymmetric cases. This work uses numerical techniques to extend the previous analysis to include the full three-dimensional effects.

In this work a three-dimensional numerical model is designed, developed and applied to study the dynamics of a liquid droplet both in free space and with a high DC magnetic field used to balance gravitational forces. The numerical model is a grid point formulation of the pseudo-spectral collocation method discretised in a spherical coordinate system with the implicit Euler method used to advance the solution in time. A coordinate transformation method is used to ensure the direct surface tracking required for modelling the surface shape oscillations.

The study covers the laminar fluid flow regime within a droplet exhibiting translational and surface shape oscillations providing a greater understanding of the physical behaviour of the droplet along with a qualitative and quantitative comparison with theoretical results. Initially a droplet oscillating in free space is considered, with a range of surface oscillation modes used to demonstrate the three-dimensional dynamics. Then the influence of electromagnetic forces on a diamagnetic droplet is studied, this includes the field from a solenoid magnet used to levitate a diamagnetic droplet. Finally the dynamics of an electrically conducting droplet in an external static magnetic field are modelled. In each case a number of methods are used to analyse the surface displacement in order to determine the surface tension and viscous damping coefficients.

The numerical study of a freely oscillating droplet shows good agreement with the low order theoretical results for droplets in the limit of low viscosity. The high accuracy of the surface tracking method allows the non-linear effects of mode coupling and frequency shift with amplitude to be observed. There is good agreement with the theoretical values available for inviscid axisymmetric oscillations and the numerical study provides the opportunity to determine these effects for three-dimensional viscous oscillations.

The magnetic field from a solenoid is used to study the levitation of a diamagnetic droplet and the oscillation frequencies of the droplet are compared with a theoretical model. The magnetic field is analysed and the accuracy of the field calculation used when determining the modification to the oscillation frequencies is considered with the use of a theoretical model. Analysis is made into the splitting of the frequency spectrum due to the magnetic field.

The theoretical model that is available for an electrically conducting droplet in a static magnetic field predicts different fluid flow within the droplet and oscillation frequency and damping rate changes. These changes are compared qualitatively and quantitatively with the numerical model results with good agreement.

Contents

Declaration	ii
Acknowledgements	iii
Abstract	iv
Contents.....	vi
Figures	ix
Tables	xi
Nomenclature	xiii
1. Introduction	1
1.1 Overview	1
1.2 Research Background	4
1.3 Thesis Objectives.....	5
1.4 Thesis Outline.....	6
2. Literature Review.....	7
2.1 Overview	7
2.2 Freely Oscillating Droplets.....	7
2.2.1 Theoretical	7
2.2.2 Numerical	12
2.2.3 Experimental.....	14
2.3 External Forces	16
2.3.1 General Theoretical Work	16
2.3.2 Acoustic	18
2.3.3 Aerodynamic.....	19
2.3.4 Electro-static	20
2.3.5 Electro-magnetic (AC).....	22
2.3.6 Electro-magnetic (DC).....	29
2.3.6.1 Conducting Droplet in a DC Electromagnetic Field	35
2.4 Summary \ Conclusions.....	37
3. Numerical Model.....	39
3.1 Overview	39
3.2 Fluid Dynamics	39

3.3	Co-ordinate Transformation	41
3.4	Unit Vectors.....	43
3.5	Boundary Conditions.....	44
3.5.1	Kinematic Boundary Condition	45
3.5.2	Stress Boundary Conditions.....	45
3.5.3	General Representation for Stress.....	45
3.5.4	Curvature	47
3.6	Implementation.....	48
3.6.1	Overview	48
3.6.2	Initialisation	51
3.6.3	Pre-Solve	55
3.6.4	Iterative Solution	56
3.6.5	Post-Solve.....	56
3.6.6	Post-Simulation Analysis.....	57
3.6.7	Default Settings	61
4.	Droplet Oscillations in Free Space.....	64
4.1	Overview	64
4.2	Oscillation Mode: $L = 2, M = 0$	65
4.2.1	Nonlinear Terms	70
4.2.2	High Amplitude Effects.....	73
4.3	Oscillation Mode: $L = 2, M = 1$	74
4.3.1	Nonlinear Terms	78
4.4	Oscillation Mode: $L = 2, M = 2$	83
4.4.1	Nonlinear Terms	87
4.5	Summary \ Conclusions.....	91
4.6	Further Work	92
5.	Diamagnetic Droplets.....	93
5.1	Overview	93
5.2	Numerical Model Considerations.....	93
5.3	Magneto-Gravitational Potential Energy.....	94
5.4	$L = 2$ Mode Energy Potential	95
5.5	Solenoid Magnet Potential	100
5.6	Solenoid Magnet Potential, Nitrogen Atmosphere.....	106
5.7	Solenoid Magnet Potential, Air Atmosphere.....	109

5.8	Summary \ Conclusions.....	117
5.9	Further Work	118
6.	Conducting Droplets	119
6.1	Overview	119
6.2	Numerical Model Considerations.....	120
6.3	Oscillation Mode: $L = 2, M = 0$	121
6.4	Oscillation Mode: $L = 2, M = 1$	123
6.5	Oscillation Mode: $L = 2, M = 2$	128
6.6	Oscillation Mode: $L = 3, M = 0$	131
6.7	Summary \ Conclusions.....	135
6.8	Further Work	135
7.	Research Summary and Further Work.....	136
7.1	Research Summary	136
7.2	Further Work	137
Appendix A –	Derivative Operators	139
A.1	Coordinate Transformation	139
A.2	First Radial Derivative	139
A.3	First Theta Derivative.....	139
A.4	First Phi Derivative.....	139
A.5	First Time Derivative	140
A.6	Second Radial Derivative	140
A.7	Second Theta Derivative	140
A.8	Second Phi Derivative	140
Appendix B –	Preconditioned Bi-Conjugate Gradient Stabilised Method...	142
Appendix C –	Publications Produced by this Research.....	144
References	145

Figures

Figure 1.1 – Surface Tension Forces	1
Figure 2.1 - Acoustic Levitation, Abe et al (2006).....	18
Figure 2.2 - Aerodynamic Levitation, Millot et al (2002).....	20
Figure 2.3 – TEMPUS Coils, Berry et al (2005).....	23
Figure 2.4 – Experimental Apparatus, Adachi et al (2008).....	27
Figure 2.5 – Drop-shaft capsule and EM coils, Fujii et al (2000a & 200b)	28
Figure 2.6 – a) Levitating Frog, b) Levitating Water Droplet.....	31
Figure 3.1 – Spherical Coordinate System	40
Figure 3.2 – Numerical Model Process	50
Figure 3.3 – Default Mesh.....	63
Figure 4.1 - Pressure Contour Lines and Velocity Vectors, (Y^0_2)	67
Figure 4.2 - Surface Displacement with Power Spectra, (Y^0_2)	69
Figure 4.3 - Surface Shape Coefficients with Power Spectra, (Y^0_2).....	71
Figure 4.4 - Frequency as a function of amplitude, (Y^0_2)	74
Figure 4.5 - Pressure Contour Lines and Velocity Vectors, (Y^l_2)	76
Figure 4.6 - Surface Displacement with Power Spectra, (Y^l_2)	77
Figure 4.7 - Surface Shape Coefficients with Power Spectra, (Y^l_2).....	81
Figure 4.8 - Pressure Contour Lines and Velocity Vectors, (Y^2_2)	85
Figure 4.9 - Surface Displacement with Power Spectra, (Y^2_2)	86
Figure 4.10 - Surface Shape Coefficients with Power Spectra, (Y^2_2).....	89
Figure 5.1 – Eigenfrequencies of the ($L = 2$) Modes.....	97
Figure 5.2 –Surface Shape Coefficients, (Y^0_2, Y^l_2, Y^2_2).....	100
Figure 5.3 – Solenoid Magnet	102
Figure 5.4 - Magneto-Gravitational Potential, (Nitrogen).....	103
Figure 5.5 – Energy Potential (z-axis), (Nitrogen).....	104
Figure 5.6 – Energy Expansion Coefficients, (Nitrogen).....	104
Figure 5.7 – Radial Derivative of the Energy Expansion Coefficients, (Nitrogen)	105
Figure 5.8 – Droplet in Solenoid Magnet, (Nitrogen).....	107
Figure 5.9 – Surface Shape Coefficients, (Nitrogen)	108
Figure 5.10 - Magneto-Gravitational Potential, (Air)	111

Figure 5.11 – Energy Potential (z-axis), (Air).....	112
Figure 5.12 – Energy Expansion Coefficients, (Air).....	112
Figure 5.13 – Radial Derivative of the Energy Expansion Coefficients, (Air)	113
Figure 5.14 – Droplet in Solenoid Magnet, (Air)	114
Figure 5.15 – Surface Shape Coefficients, (Air)	116
Figure 6.1 – Surface Shape Coefficient with Power Spectra, (Y^0_2).....	122
Figure 6.2 – Surface Shape Coefficient with Power Spectra, (Y^l_2).....	125
Figure 6.3 - Pressure Contour Lines and Velocity Vectors, (Y^l_2)	127
Figure 6.4 – Surface Shape Coefficient with Power Spectra, (Y^2_2).....	129
Figure 6.5 – Surface Shape Coefficient with Power Spectra, (Y^0_3).....	132
Figure 6.6 - Pressure Contour Lines and Velocity Vectors, (Y^0_3)	134

Tables

Table 3.1 – Numerical Model, Default Settings	62
Table 4.1 – Material Properties (Water).....	64
Table 4.2 – Initial Conditions, (Y^0_2)	66
Table 4.3 – Velocity & Reynolds Number Maximum, (Y^0_2)	68
Table 4.4 – Theoretical Results, (Y^0_2)	69
Table 4.5 – Numerical Results, (Y^0_2)	69
Table 4.6 – Theoretical Results, (Y^0_2)	72
Table 4.7 – Numerical Results, (Y^0_2)	72
Table 4.8 – Initial Conditions, (Y^1_2)	75
Table 4.9 – Velocity & Reynolds Number Maximum, (Y^1_2)	77
Table 4.10 – Theoretical Results, (Y^1_2)	78
Table 4.11 – Numerical Results, (Y^1_2)	78
Table 4.12 – Numerical Results, (Y^1_2)	82
Table 4.13 – Initial Conditions, (Y^2_2)	83
Table 4.14 – Velocity & Reynolds Number Maximum, (Y^2_2)	86
Table 4.15 – Theoretical Results, (Y^2_2)	87
Table 4.16 – Numerical Results, (Y^2_2)	87
Table 4.17 – Numerical Results, (Y^2_2)	90
Table 5.1 – Initial Conditions, (Y^0_2, Y^1_2, Y^2_2)	98
Table 5.2 – Material Properties (Water).....	98
Table 5.3 – Frequency Calculations, (Y^0_2, Y^1_2, Y^2_2)	100
Table 5.4 – Initial Conditions, (Nitrogen).....	106
Table 5.5 – Series Expansion Coefficients and Derivative at R_0 , (Nitrogen)	109
Table 5.6 – Frequency Calculations, (Nitrogen).....	109
Table 5.7 – Material Properties (Air)	110
Table 5.8 – Initial Conditions, (Air).....	114
Table 5.9 – Series Expansion Coefficients and Derivative at R_0 , (Air)	117
Table 5.10 – Frequency Calculations, (Air).....	117
Table 6.1 – Material Properties (Silicon).....	119
Table 6.2 – Initial Conditions, (Y^0_2)	121
Table 6.3 – Theoretical Results, (Y^0_2)	122

Table 6.4 – Numerical Results, (Y^0_2)	123
Table 6.5 – Initial Conditions, (Y^I_2)	124
Table 6.6 – Theoretical Results, (Y^I_2)	125
Table 6.7 – Numerical Results, (Y^I_2)	125
Table 6.8 – Initial Conditions, (Y^2_2)	128
Table 6.9 – Theoretical Results, (Y^2_2)	129
Table 6.10 – Numerical Results, (Y^2_2)	130
Table 6.11 – Initial Conditions, (Y^0_3)	131
Table 6.12 – Theoretical Results, (Y^0_3)	133
Table 6.13 – Numerical Results, (Y^0_3)	133

Nomenclature

The symbols used are summarised in the following table:

Symbol	Definition	Unit
\mathbf{V}	Velocity Vector	m s^{-1}
t	Time	s
ρ	Density	kg m^{-3}
P	Pressure	N m^{-2}
ν	Kinematic Viscosity	$\text{m}^2 \text{s}^{-1}$
\mathbf{F}_{vol}	Momentum Body Force (per unit volume)	N m^{-3}
x, y, z	Cartesian Coordinates	m
r, θ, ϕ	Spherical Polar Coordinates	m
u, v, w	Velocity Components	m s^{-1}
f_r, f_θ, f_ϕ	Body Force Components (per unit volume)	N m^{-3}
$S(\theta, \phi, t)$	Transient Surface Shape Function	-
$X(\theta, \phi)$	Static Surface Shape Function	-
R_0	Spherical Droplet Radius	m
$\bar{r}, \bar{\theta}, \bar{\phi}, \bar{t}$	Transformed Coordinates	m
$\mathbf{e}_n, \mathbf{e}_{\tau 1}, \mathbf{e}_{\tau 2}$	Surface Unit Vectors	-
$\mathbf{r}_s(\theta, \phi, t)$	Surface Position Vector	m
Π	Stress Tensor	N m^{-2}
Γ	Surface Tension Coefficient	N m^{-1}
K	Surface Curvature	m^{-1}
e	Strain Rate Tensor	-
r_i, θ_j, ϕ_k	Grid Points	m
D_k^n	Differentiation Matrix	-
$Y_L^M(\theta, \phi)$	Spherical Harmonic	-
s_L^M	Transient Surface Expansion Coefficient	-
x_L^M	Static Surface Expansion Coefficient	-
P_L^M	Associated Legendre Polynomial	-
N_L^M	Normalisation Coefficient	-
ω_L^M	Surface Oscillation Frequency	s^{-1}
γ_L^M	Surface Oscillation Damping Coefficient	s^{-1}
L	Polar Number	-
M	Azimuthal Number	-

Re	Reynolds Number	-
$ \mathbf{V} $	Magnitude of Velocity	$m\ s^{-1}$
\mathbf{J}	Electric Current Density	$A\ m^{-2}$
σ	Electrical Conductivity	$S\ m^{-1}$
$\mathbf{B}(r, \theta, \phi)$	Magnetic Field	T
B_0	Magnitude of Constant Magnetic Field	-
ϕ_E	Electric Potential	V
χ_V	Volumetric Magnetic Susceptibility	-

1. Introduction

1.1 Overview

The dynamics of a liquid droplet displaced from equilibrium is of interest from a pure scientific point of view as well as for the impact it has on various industrial applications. Some early theoretical works on the dynamics of a liquid drop were developed through an analogy with the earth, a solid core with the oceans as a liquid outer layer performing oscillatory motion due to gravitational forces (Kelvin: 1863a, 1863b, 1890). A liquid droplet can also exhibit surface oscillations but with a different restoring force, surface tension. Surface tension arises due to an imbalance of forces between the interior atoms\molecules and those at the surface. Particles in the interior receive equal forces from the surrounding particles, whereas the surface particles receive a net force directed towards the interior of the material, as illustrated in Figure 1.1. The droplet is in equilibrium when the forces between the particles are balanced, but if the droplet is displaced from this equilibrium, oscillations occur as the forces adjust to move the droplet back towards equilibrium.

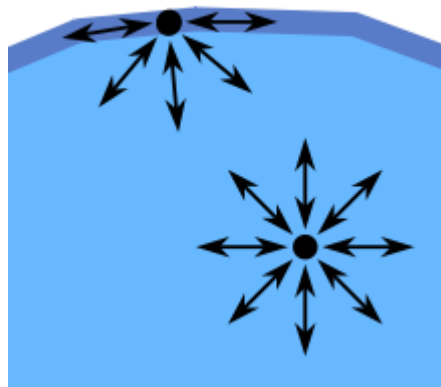


Figure 1.1 – Surface Tension Forces

The relationship between the frequency of the surface oscillations and the restoring force of surface tension provide a measure of the cohesive force characterised by the surface tension coefficient (Rayleigh: 1879). The surface tension coefficient is an important input

parameter for numerical modelling of industrial processes and it can be measured using a number of different experimental techniques. However these techniques are limited in their application, with most techniques not applicable to high temperature, highly reactive materials such as liquid metals. The determination of the surface tension coefficient through experimental measurement of the surface oscillation frequency is known as the oscillating drop technique. The surface oscillations are damped by viscous forces and the oscillating drop technique also relates to the measurement of the viscous damping coefficient through a formula determined by theoretical analysis (Lamb: 1881, 1975).

The oscillating drop technique has been used in a variety of experimental conditions. In some cases the droplet oscillates almost in isolation from the surroundings, for example in a drop-shaft, parabolic flight, or microgravity experiment where the gravitational forces are insignificant. These experimental techniques are limited in different ways, e.g. financial expense or length of measurement time. The measurements have also been performed on droplets confined with a range of external forces, acoustic, aerodynamic, electromagnetic (AC and DC), and electrostatic, which can be used to compensate gravitational forces. Each method has its own advantages and disadvantages and is usually restricted to particular groups of materials. However there are some common factors in their application to the oscillating drop technique. The use of this technique relies on a theoretical formula that relates the oscillation frequency or damping rate to the coefficients of surface tension or viscosity respectively. The external forces have an impact on the surface oscillations and so need to be taken into account in the theoretical analysis. The measurement requires the surface dynamics to be captured, which is usually accomplished by collecting a time-series of images or a signal generated by a photo-detector (Egry: 2005a).

The experimental techniques are most beneficial to high temperature, highly reactive materials such as liquid metals and have wider application than just the oscillating drop technique. The non-contact nature allows further properties of materials to be studied over a wide range of temperatures, including, density, thermal conductivity, specific heat, thermal expansion, and electrical conductivity.

In general the dynamics of a liquid droplet is a well studied problem. A large number of numerical studies have been conducted into the oscillation of a liquid droplet but the

majority of the studies have been restricted to axisymmetry. Axisymmetric studies of viscous free droplets have been conducted by Foote (1973), Alonso (1974), Basaran (1992), and Meradji et al (2001), while Patzek (1991) has considered inviscid drops and Lundgren & Mansour (1988) used an approximation to model droplets with weak viscous effects. Some three-dimensional studies have been conducted for a free droplet; Pozrikidis (2001) considers inviscid drops, while Watanabe (2006, 2008, 2009) includes the effects of viscosity.

Axisymmetric studies with the inclusion of AC electromagnetic forces have been conducted by Berry (2005) and Chapelle et al (2008) and for both AC and DC electromagnetic forces by Bojarevics & Pericleous (2003, 2009a). Three dimensional modelling with the inclusion of AC electromagnetic and electrostatic forces has been conducted by Li (2006).

This list is not exhaustive as the study of liquid droplet dynamics is important to a number of different applications and the use of different numerical techniques has different advantages and disadvantages. However these studies are representative of studies particular to the quantification of the surface oscillations and its application to the oscillating drop technique.

The use of the oscillating droplet technique is the only option for measuring surface tension and viscosity of some materials and is often used even though concerns have been expressed over the validity of the correction formulae that are available when the droplets are confined using external forces, Egry (1999, 2005a).

This provides research opportunities for investigating the full non-linear three dimensional viscous dynamics of a liquid droplet both with and without external forces. In particular there is the opportunity to study the application of the oscillating drop technique when DC electromagnetic forces are used to confine the droplet.

1.2 Research Background

The spectral collocation method with direct free surface tracking has been used extensively at the University of Greenwich to study various applications involving the electromagnetic processing of materials. A review of the use of this numerical technique for modelling the electromagnetic processing of materials is given by Bojarevics and Pericleous (2007b) and Pericleous and Bojarevics (2007), with results presented for AC/DC electromagnetic levitation of liquid droplets, induction melting in a cold crucible, and MHD aspects of aluminium electrolysis.

The details of the numerical modelling approach to the axisymmetric electromagnetic levitation of liquid droplets are given in Bojarevics and Pericleous (2003) and a detailed description of the method of mutual inductance used to model the AC electromagnetic induction in Bojarevics and Pericleous (2007a).

Bojarevics and Pericleous (2003, 2009a) used the numerical model to study liquid droplets in a combination of AC and DC magnetic fields. A number of test cases were considered including;

- The un-damped surface oscillation considered by Rayleigh (1879) and the damped surface oscillation considered by Lamb (1881, 1975) for a free droplet
- A droplet in a uniform DC field
- A conducting droplet in a combined AC\DC electromagnetic field

The modification in surface oscillation frequency due to a DC electromagnetic field used to confine a diamagnetic liquid droplet was derived by Easter, Bojarevics, and Pericleous (2009) and compared with the result produced by the axisymmetric numerical model. Bojarevics, Easter, and Pericleous (2010) considered the variation in surface oscillation of a diamagnetic liquid droplet levitated in the DC electromagnetic field of solenoids with different geometry.

The effect of internal flow on material property measurements was considered by Bojarevics and Pericleous (2009b) for electrically conducting droplets in an AC

electromagnetic field. The $k-\omega$ model was used to capture turbulent flow within the droplet, which was found to be present even for low magnetic field strengths resulting in additional damping of the surface oscillations. The Joule heating associated with the induction currents in AC electromagnetic levitation results in thermo-capillary convection, which was shown to alter the dynamics of the droplet. The effect of droplet rotation, often observed in experiment was found to modify the surface oscillation frequency in agreement with the theoretical results of Busse (1984).

Other work by the group has involved modelling the thermal conductivity measurement process in AC electromagnetically levitated droplets; In Bojarevics, Roy, Easter, and Pericleous (2009) the turbulent flow generated by the AC field was shown to disrupt the measurement process, but the convective flow could be damped with the addition of a DC field allowing the measurement to be obtained successfully. Further examination of the turbulence effects and the damping effect of different DC fields was made by Bojarevics, Easter, and Pericleous (2009). The vertical stability and impact of translational oscillations on the measurement process were covered in Roy, Easter, Bojarevics, and Pericleous (2011).

1.3 Thesis Objectives

The spectral collocation method with coordinate transformation for direct surface tracking provides an accurate method for modelling liquid droplet oscillations subject to external forces, Bojarevics and Pericleous (2003 & 2009a). The objectives of this work are to develop a numerical model that follows the same approach as the axisymmetric modelling of Bojarevics and Pericleous but extends the model to include three-dimensional effects with the inclusion of high DC electromagnetic forces.

A number of case studies will be presented that demonstrate the capability of the numerical model to investigate three-dimensional effects. In each case the objectives are to provide a clear explanation of the current understanding of the physical process involved and to enhance the understanding of the theoretical formulae and validate their application to experimental results.

The key motivation for studying liquid droplet oscillations is its application to the oscillating drop method for determining the surface tension and viscous damping coefficients. Therefore each case will include detailed analysis of the oscillation frequency and damping rate using a variety of numerical techniques.

1.4 Thesis Outline

This thesis consists of seven sections. In section 2 a review of the literature is made, which covers the theoretical, numerical, and experimental developments in the study of liquid droplet dynamics in free space and in the presence of external forces. In section 3 the design, development, and implementation of a numerical model is outlined. In section 4 the numerical model is applied to the study of a freely oscillating droplet with qualitative and quantitative analysis of the internal fluid flow and surface oscillation modes. In section 5 the numerical model is applied to the study of a diamagnetic droplet in free space and levitated in terrestrial gravity with the use of a solenoid coil. A quantitative comparison is made between the theoretical predictions and numerical results for the deformed shape of the droplet and the oscillation frequencies. In section 6 the numerical model is applied to the study of a conducting droplet in a static magnetic field. A quantitative comparison is made between the theoretical predictions and numerical results for the surface oscillation frequencies and damping rates. In section 7 a summary is given and conclusions formulated for the research conducted along with opportunities for further work.

2. Literature Review

2.1 Overview

The study of liquid droplet dynamics has been of scientific interest for over a 100 years with some of the earliest theoretical work by W. Thompson (Lord Kelvin: 1863a, 1863b, 1890) and J. W. Strutt (Lord Rayleigh: 1879) being motivated by the analogy with the behaviour of the oceans surrounding the Earth. It is desirable to gain understanding of the internal fluid dynamics and free surface interaction (surface oscillation and damping) of isolated droplets as well as droplets subject to external stimulation. In microgravity or when combined with external positioning forces, liquid droplets can also be used to study physical processes including heat transfer and solidification as well as providing a means of measuring physical properties of materials in a situation where there is no contamination from the surrounding media.

In §2.2 the dynamics of liquid droplets in free space are discussed, including details of internal fluid flow and damped surface oscillations, beginning with the theoretical background information then moving on to discuss the numerical studies that have been completed and experimental observations and measurements. In §2.3 the use of external forces to confine\levitate the liquid droplets is introduced and the advantages and disadvantages of different methods are outlined with reference to the key theoretical, numerical, and experimental work that has been completed in each area.

2.2 Freely Oscillating Droplets

2.2.1 Theoretical

Some of the earliest recorded work on the oscillation of liquid droplets was the derivation of the normal mode oscillation frequencies by Lord Rayleigh (1879). In an appendix of ‘On the Capillary Phenomena of Jets’ Rayleigh considered the axisymmetric oscillations (vibrations) of an inviscid liquid droplet in free space with a spherical equilibrium shape by balancing the surface potential energy and the kinetic energy of the fluid and showed that

the normal mode surface shapes can be described by an expansion of the Legendre polynomials (P_L):

$$r_s = a_0 + a_1 P_1(\cos \theta) + a_2 P_2(\cos \theta) + \dots \quad (2.1)$$

The normal mode frequencies were found to be related to the degree of the Legendre polynomial (L), the equilibrium droplet radius ($a_0 = R_0$), as well as the surface tension coefficient (Γ), and density (ρ) of the material:

$$\omega_L^2 = \frac{L(L-1)(L+2)\Gamma}{\rho R_0^3} \quad (2.2)$$

A more generic basis for modelling three-dimensional viscous oscillations is to expand the surface position as the sum of static (X) and time-dependent (S) components, both given as expansions of spherical harmonic functions $Y_L^M(\theta, \phi)$.

$$r_s(\theta, \phi, t) = R_0[1 + X(\theta, \phi) + S(\theta, \phi, t)] \quad (2.3)$$

$$X(\theta, \phi) = \sum_{L=0}^{L=\infty} \sum_{M=-L}^{M=L} x_L^M Y_L^M(\theta, \phi) \quad (2.4)$$

$$S(\theta, \phi, t) = \sum_{L=0}^{L=\infty} \sum_{M=-L}^{M=L} s_L^M(t) Y_L^M(\theta, \phi) \quad (2.5)$$

The static term is only required when external forces are present and is often combined with the time-dependent component, i.e. in raw experimental data and numerical results. The time dependence of the surface shape coefficients s_L^M is assumed to be harmonic with exponential damping:

$$\cos(\omega_L^M t) \exp(-\gamma_L^M t) \quad (2.6)$$

A derivation using these definitions shows that the formula for the oscillation frequency is still valid in the non-axisymmetric case; the oscillation frequencies are degenerate, i.e. not dependent on the azimuthal number of the spherical harmonic (M). This early research

highlighted the relationship between surface tension and oscillation frequency that would later form the basis of a technique for measuring the surface tension coefficient of materials.

Our understanding of the role of viscous forces in the dynamics of liquid droplets originates in the work by Kelvin (1863a, 1863b, 1890), which primarily considered the oscillations and damping of a globe due to the forces of gravity. This work was extended by Lamb (1881, 1975), with the more general analysis shown to be applicable for a viscous spheroid with surface tension as the restoring force instead of gravity. The key result being the identification of the damping coefficient of the normal mode oscillations due to viscous forces, valid in the case of ‘small viscosity’ ($\nu \ll \omega R_0^2$):

$$\gamma_L = \frac{(L-1)(2L+1)\nu}{R_0^2} \quad (2.7)$$

The reciprocal of (2.7) gives the viscous damping time, the time for the oscillation amplitude to decrease by $(1/e)$. This relationship also highlights the possibility of a measurement technique, this time for the coefficient of viscosity from an experimental measurement of damping rate of the oscillations. The rate of damping increases considerably as the mode number increases, so that from the perspective of experimental observations the oscillations are limited to the lower order modes, which decay more slowly.

Chandrasekhar (1958) again considered the oscillations of a viscous globe, extending the analysis to include finite viscosity. Later, Reid (1960) showed that the general results of Chandrasekhar are also equivalent for a viscous spheroid where the restoring force is due to surface tension instead of gravity. This is due to the fact that the damping coefficient is independent of the forces trying to maintain a spherical equilibrium, either gravitational or surface tension (cf. 2.7). Results of Chandrasekhar’s analysis include a transcendental equation for the complex quantity sigma ($\sigma_L = \gamma_L + i \omega_L$) that defines the oscillation frequency and damping rate:

$$\omega_L^2 - \left[\frac{2(L^2 - 1)}{x^2 - 2xq_L} - 1 + \frac{2L(L - 1)}{x^2} \left(1 - \frac{(L + 1)q_L}{\frac{x}{2} - q_L} \right) \right] \sigma_L^2 = 0 \quad (2.8)$$

Where $(x = \sqrt{\sigma_L R_0^2 / \nu})$, $(q_L = J_{L+3/2}(x) / J_{L+1/2}(x))$, and J_i are the Bessel functions of order i .

The damping rate is dependent on the material properties (density, viscosity) as well as the size of the droplet (R_0). The analysis also showed that for a given material there is a critical droplet size above which damped periodic oscillations occur (under-damping) and below which aperiodic damping occurs. Below the critical radius two aperiodic modes of decay exist, a slow ‘creeping’ mode that depends on the inertia of the fluid (over-damping) and a rapidly decaying ‘inertial’ mode (critical-damping).

Tang and Wong (1974) provided a detailed study of the Chandrasekhar equation (2.8) and its generic applicability to restoring forces of gravity, surface tension, and electrostatics.

All of these results are linear results and require small amplitude oscillations. As the amplitude of oscillation increases non-linear effects become more prominent. Tsamopoulos & Brown (1983) extended the theoretical work on axisymmetric inviscid droplets to ‘moderate’ amplitude using a Poincare-Lindstedt expansion technique. As the amplitude of oscillation is increased there is a shift in frequency due to nonlinear effects. The nonlinearity is shown to be ‘soft’ for the first three modes ($L = 2, 3$, and 4) resulting in a quadratic decrease in frequency with amplitude:

$$\begin{aligned} \omega_2^{0(2)} &= \omega_2^{0(0)} \left(1 - \frac{(s_2^0)^2}{2} 1.27752 \right) & L = 2 \\ \omega_3^{0(2)} &= \omega_3^{0(0)} \left(1 - \frac{(s_3^0)^2}{2} 2.08992 \right) & L = 3 \\ \omega_4^{0(2)} &= \omega_4^{0(0)} \left(1 - \frac{(s_4^0)^2}{2} 2.91361 \right) & L = 4 \end{aligned} \quad (2.9)$$

These formulae are actually valid to fourth order error because it is shown that the first and third order contributions are zero. Harmonic oscillation with a single mode of the form $(s_L \cos(\omega_L t) P_L)$ would result in a variation in volume, which for an incompressible fluid is forbidden as it would also constitute a variation in mass. In order to conserve volume (mass), more than a single mode of oscillation is required resulting in mode-coupling, which becomes more prominent as the amplitude of the dominant mode is increased. Tsamopoulos & Brown (1983) calculated the second order, changes to surface shape, and velocity for the first three modes ($L = 2, 3,$ and 4), which includes the mode-coupling required to conserve volume (mass) as the amplitude increases. For example the ($L = 2$) mode consists of the zeroth order spherical radius, first order harmonic oscillation at a given amplitude, and second order non-linear components (dependent on 2ω) proportional to the square of the amplitude:

$$\begin{aligned}
 r_s^{(0)} &= R_0 \\
 r_s^{(1)} &= s_2^0 \cos(\omega_2^0 t) P_2 \\
 r_s^{(2)} &= \frac{(s_2^0)^2}{2} \left\{ -\frac{1}{5} [1 + \cos(2\omega_2^0 t)] P_0 + \frac{11}{14} \left[1 - \frac{29}{33} \cos(2\omega_2^0 t) \right] P_2 \right. \\
 &\quad \left. + \frac{18}{35} \left[1 + \frac{3}{5} \cos(2\omega_2^0 t) \right] P_4 \right\}
 \end{aligned} \tag{2.10}$$

Natarajan & Brown (1986) investigated further the nonlinear effects in inviscid droplets using second order nonlinear analysis and demonstrated that a ‘quadratic internal resonance’ exists between 5th and 8th and also the 10th and 16th modes that are implied by:

$$\begin{aligned}
 \omega_8^M &= \pm 2\omega_5^M \\
 \omega_{16}^M &= \pm 2\omega_{10}^M
 \end{aligned} \tag{2.11}$$

The three-dimensional analysis showed that axisymmetric modes are unstable with respect to small non-axisymmetric perturbations and most non-axisymmetric initial conditions result in stochastic (random) motion with ‘the total surface energy exchanged between all components of the interacting modes’. The calculations suggest that the effects should be observable in centimetre sized water drops, which are above the modifying effects of

viscosity; however the effects generally occur on time-scales longer than the primary oscillation. Natarajan & Brown (1987), extended the previous work calculating the third order resonant interactions of the ($L = 3$) mode and the interaction of the ($L = 2$) and ($L = 4$) modes.

Prosperetti (1980) investigated small-amplitude oscillations in conditions where viscous effects are important by solving an initial value problem. An approach based on Laplace transforms was used to demonstrate that the previously obtained results using normal mode analysis (harmonic time-dependence) for ‘small viscosity’ are only reached asymptotically.

2.2.2 Numerical

The oscillations of freely oscillating droplets have been considered numerically using a number of different techniques each with their own advantages and disadvantages. A summary of the key numerical studies are considered in order to highlight their contribution and the openings for further work in this area.

Foote (1973) used the marker-and-cell (MAC) method to study axisymmetric, moderate amplitude, low viscosity droplets and made a comparison with the available theoretical results. The initial conditions used were zero velocity and initial surface shape given by the ($L = 2$) mode and also an actual oblate spheroid. The low amplitude cases showed good agreement with the analytical theory.

Alonso (1974) also used the marker-and-cell (MAC) method to demonstrate the oscillations of electrically charged and neutral droplets.

Lundgren & Mansour (1988) used the boundary integral method with ‘weak’ viscous terms included as first order terms in the stress boundary condition to model axisymmetric oscillations. The results showed that even low viscosity has an important effect on mode-coupling. In this work two types of initial condition are considered, the Rayleigh mode initial shape with zero velocity and the ‘impulsive’ spherical shape with initial velocity potential. Instabilities were found to arise in the higher amplitude \ velocity cases and so an artificial dissipation was used to suppress the numerical instabilities. The study mainly

focused on higher order modes (high frequency oscillations) and large amplitude oscillations with some analysis of the coupling between the fourth and fifth mode.

Patzek (1991) used the Galerkin weighted residual method to study axisymmetric inviscid droplet motion. The Rayleigh mode and ‘impulse’ initial conditions were considered. Energy conservation was determined and oscillation patterns were presented. Fourier analysis of the pole point was conducted for a number of initial conditions and the time spent in the prolate distortion phase was calculated. The results showed agreement with theoretical analysis at low amplitude but diverged from the theoretical results at high amplitude.

Basaran (1992) used a Galerkin/finite-element method to study the nonlinear oscillations of axisymmetric viscous droplets. The results showed that the ($L = 2$) mode spends more time in the prolate part of the cycle than inviscid droplets (agrees with experiment). The damping rate in the first period is greater with amplitude, and then the damping becomes constant. Two types of initial condition are considered prolate\oblate and Rayleigh mode surface shape, both with zero velocity and pressure. Volume correction factors are used to adjust the initial condition to satisfy mass conservation. Cases with even mode initial conditions do not display any transfer of energy to odd modes. In contrast cases with odd mode initial conditions show transfer of energy to both even and odd modes. The case with prolate initial condition is shown to be similar to the ($L = 2$) initial condition with positive amplitude although the behaviour of the cases with oblate initial condition is quite different to the ($L = 2$) initial condition with negative amplitude. Volume correction factors are used, which effectively results in an initial condition that has a dominant mode with an additional constant component. Formulae are given for the axisymmetric modes ($L = 2, 3, 4, 5$), which relate the constant component to the amplitude of the dominant mode; however a full derivation is not given.

Meradji et al (2001) modelled axisymmetric viscous droplets using the Galerkin Finite Element code (FIDAP). The ($L = 2$) mode initial condition was used and the oscillation frequency was compared with theoretical predictions after one oscillation period and comments were made regarding the prolate\oblate surface shapes.

Pozrikidis (2001) used the ‘generalised vortex method’ to study the three-dimensional oscillations of inviscid droplets. The initial conditions used were a spherical droplet shape with velocity potential at the surface. Instabilities were found to arise in the oscillation and it was found that the instabilities arise earlier when the time-step was reduced, something also observed by Lundgren & Mansour (1988). Smoothing of the surface was used to prevent the instabilities allowing a longer simulation time; however this resulted in a reduction in the amplitude, which should not occur in the inviscid case. The asymmetry of the ($L = 2, M = 0$) mode and the decrease in frequency (increase in period) associated with nonlinear effects were observed. Conservation of energy and volume were used to assess the performance of the numerical scheme. Loss of both volume and total energy were observed over seven oscillation periods. Similar results were obtained for the ‘transverse shear mode’ (2,1), the ‘toroidal mode’ (2,2), and the (3,0), (3,1), and (3,2) modes.

Watanabe (2006, 2008, 2009), used the Level Set Method to study the three-dimensional oscillation and rotation of a liquid droplet. The theoretical analysis for oscillating and rotating droplets have shown that there is a decrease in frequency with increasing amplitude but an increase in frequency with increasing rotation frequency, Watanabe investigated combinations of rotation and amplitude which can result in zero frequency shift.

Stein et al (2009) studied the laminar flow of a three-dimensional oscillating sphere with generated internal vortices.

2.2.3 Experimental

The analytical theory discussed so far applies to droplets oscillating in an inactive environment with no external forces. This is hard to achieve in practice but is most closely approximated by experiments in which the droplet is in free-fall.

The oscillating droplet technique has been used to determine the surface tension of liquid droplets in free-fall following the breakup of a fluid jet: Hiller and Kowalewski (1989), Becker et al. (1991), and Stuckrad et al. (1993). The oscillations were assumed to be axisymmetric and the coefficients of an expansion of Legendre polynomials describing the

surface dynamics were determined by image analysis and were found to be well represented by the first five oscillation modes. The results have been compared with measurements made using the ring method and showed relatively good agreement. The experiments have included surfactant solutions demonstrating the application of the oscillating droplet technique to investigate the transient surface tension that immediately follows the jet break-up. Becker et al. (1991) proposed a theoretical model for the large amplitude nonlinear oscillations that preceded the low amplitude linear oscillations. The experimental results showed good agreement with the theoretical models in both regimes. Becker et al. (1994a) conducted theoretical analysis of large amplitude non-linear oscillations and concluded that viscosity has a large impact on mode coupling and that even at low amplitude “resonant mode interaction” remains. Becker et al. (1994b) used phase space analysis to derive the nonlinear equations of motion associated with viscous droplet oscillations providing a less computationally intensive method of analysing nonlinear oscillations than a full numerical model. Kowalewski & Bruhn (1994) provided validation of the model proposed by Becker (1991) up to the aperiodic limit. Comparison was made between experimental results as well as the other theoretical and numerical results available.

It is also possible to study the oscillations of a droplet within another immiscible fluid. For example Azuma & Yoshihara (1999) performed experiments using a mercury droplet in sulphuric acid solution. Surface oscillations were excited using electrodes and observed in both static conditions and in free-fall. A theoretical model was proposed for the three-dimensional oscillations and compared with the experimental results.

One of the main advantages of performing experiments using a noncontact mechanism is the application to materials with high melting temperatures and high reactivity. In these cases the sample needs to be levitated and heated before the oscillation experiment is conducted. For example Matsumoto et al. (2005) measured the surface tension of under-cooled molten copper using the oscillating drop technique in a drop tube (shaft). The droplet was initially levitated using an AC coil in which 5 oscillation peaks were detected and then the droplet was released and the power spectra reduced to a single oscillation peak.

It is also possible to study droplet oscillations in parabolic flights or microgravity experiments conducted in space but these applications still require some form of weak positioning force. Although the positioning forces are weak in these conditions and have limited effect on the measurement process, they will be discussed in the individual sections arranged by the type of external force used.

2.3 External Forces

Although some experimental work has been carried out for freely oscillating droplets, practical applications usually require some form of positioning field to provide confinement \ levitation of the liquid droplet. This levitation \ confinement can be achieved in a number of different ways, each of which is described in the following sections, §2.3.2 Acoustic, §2.3.3 Aerodynamic, §2.3.4 Electro-static, §2.3.5 Electro-magnetic (AC), and §2.3.6 Electro-magnetic (DC). The different methods of levitation have a different effect on the dynamics of the drop due to the variation in the external force. These differences can provide both advantages and disadvantages to particular applications.

2.3.1 General Theoretical Work

The introduction of external forces, no matter how small, will have some effect on both the frequency and damping rate of the surface shape oscillations. A number of theoretical works have been conducted that adapt the theory of freely oscillating droplets to include the external forces. Some key developments were made by Suryanarayana and Bayazitoglu (1991), who considered inviscid droplets with acoustic and electromagnetic forces, but perhaps the most widely used in practical applications is the work of Cummings and Blackburn (1991).

Cummings and Blackburn (1991) considered inviscid droplets in an electromagnetic field in a generic context and also with some specific cases. The case where the magnetic field is assumed to remain independent of the change in droplet shape showed an increase in the mean square frequency of the fundamental oscillation mode that is dependent on the mean translational frequency:

$$\frac{1}{5} \sum_{M=-2}^{M=+2} (\omega_2^M)^2 = (\omega_R)^2 + 2 \overline{\omega_{tr}^2} \quad (2.12)$$

The change is independent of the spatial variation of the magnetic field and the static deformation of the droplet. Another case considered is that of a linear magnetic field aligned with the z-axis. In this case the degeneracy of the three ($L = 2$) mode frequencies is lifted and the individual frequencies are given by:

$$(\omega_2^0)^2 = (\omega_R)^2 + \overline{\omega_t^2} \left(3.832 - 0.1714 \left(\frac{z_0}{R_0} \right)^2 \right) \quad (2.13)$$

$$(\omega_2^{\pm 1})^2 = (\omega_R)^2 + \overline{\omega_t^2} \left(3.775 + 0.5143 \left(\frac{z_0}{R_0} \right)^2 \right) \quad (2.14)$$

$$(\omega_2^{\pm 2})^2 = (\omega_R)^2 + \overline{\omega_t^2} \left(-0.9297 + 2.5751 \left(\frac{z_0}{R_0} \right)^2 \right) \quad (2.15)$$

Where $\omega_R = \omega_2$ is the Rayleigh frequency (independent of azimuthal number M), $z_0 = g/(2 \overline{\omega_t^2})$, and ω_t is the frequency of the translational motion

This results in a modification to the Rayleigh mode frequency:

$$(\omega_R)^2 = \sum_{M=-2}^{M=+2} (\omega_2^M)^2 - \overline{\omega_t^2} \left(1.9 + 1.2 \left(\frac{z_0}{R_0} \right)^2 \right) \quad (2.16)$$

The introduction of viscosity to the theoretical analysis has been conducted by Bratz and Egry (1995) for arbitrary magnetic fields. Specific results were derived for the modification to the frequency and damping rate for high Reynolds number cases and also for a linear magnetic field. The degeneracy of the frequency and damping rate for the ($L = 2$) modes was found to be lifted by the magnetic field.

2.3.2 Acoustic

Standing acoustic waves have been used to provide the force to balance gravity. In these experiments an acoustic standing wave is produced by a superposition of an input wave introduced from a horn at the bottom of the cavity and the wave reflected from the opposite end of the cavity, illustrated in Figure 2.1.

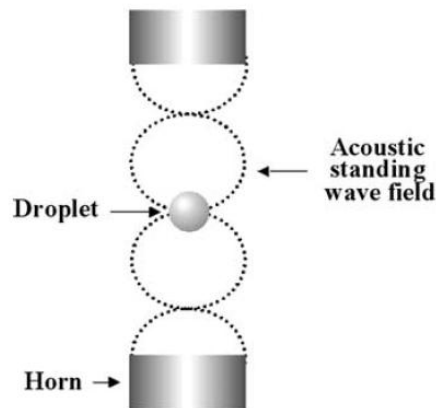


Figure 2.1 - Acoustic Levitation, Abe et al (2006)

Trinh and Wang (1982) performed a qualitative study of the internal flow field of droplets performing large amplitude surface oscillations observed using photographs of streak patterns of suspended dye particles obtained during their experiments. The fluid flow was shown to be more complicated than linear theory suggests with evidence of re-circulation at oscillation amplitudes as low as 8% R_0 . The re-circulation originated at the free surface due to viscous forces and propagated into the bulk of the droplet. In contrast to the decrease in frequency at larger amplitudes, the viscous damping rate was generally found to be constant.

Wang et al (1996) reported on experiments conducted using the Drop Physics Module (DPM) in the United States Microgravity Laboratory-I (USML-1) on the space shuttle Columbia. Experimental measurements of the frequency shift due to non-linear effects were shown to be in good agreement with the theoretical predictions of Tsamopoulos & Brown, (1983). The frequency was lower for rotating droplets subject to acoustic radiation pressure. The amount of time spent in the prolate phase of the cycle for the ($L = 2, M = 0$) mode was found to be significantly less than the classical case. The interpretation that the

droplet is spending more time in the prolate phase is a consequence of the type of analysis used. When the aspect ratio of the droplet is analysed it contains the superposition of the second order P_0 component and first order P_2 component in (2.10).

Trinh et al (1998) performed experiments to investigate the resonant oscillations of drops and bubbles in another immiscible fluid with ultrasonic radiation pressure used to drive the oscillations. Mode coupling was observed between several different modes with different driving mode frequencies. The frequencies were not always found at the integer multiples of the normal mode frequencies as predicted by the nonlinear theory.

Abe et al (2006) performed a combined numerical and experimental study of a large droplet levitated in acoustic wave field. A numerical simulation was used to calculate the pressure and velocity distribution due to the acoustic wave. The pressure field was compared with the experimental data showing good qualitative agreement. Experiments were performed in terrestrial gravity and also microgravity (a parabolic flight with 20 second duration). The droplets were introduced to the cavity using a syringe and the shape changes were captured by a CCD camera. The internal flow was obtained using particle image velocimetry (PIV). Due to the constraints of the levitation force experiments were limited to 4mm diameter for levitation in terrestrial gravity and 9.5mm in microgravity. Internal flow analysis revealed vortices were present in both terrestrial and microgravity cases.

2.3.3 Aerodynamic

It is also possible to levitate a liquid droplet using a stream of gas introduced from below creating an upward force on the droplet and opposing the gravitational force.

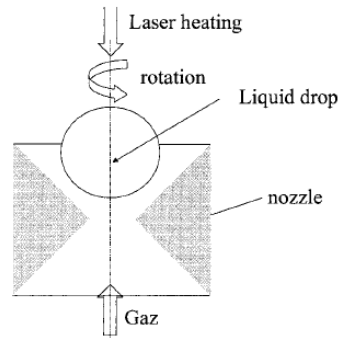


Figure 2.2 - Aerodynamic Levitation, Millot et al (2002)

Millot et al (2002) performed experiments to measure the surface tension of the liquid metal, Nickel surrounded by an Argon/Hydrogen mixture. The sample was heated from above by a CO₂ laser to up to 3000 °C to keep it in a liquid state and a nozzle was used to reflect light from the laser giving more uniform irradiation. The use of the nozzle was found to produce rotation and precession of the droplet. The levitated droplet was found to have a static deformation resulting in a splitting of the ($L = 2$) mode frequencies in agreement with the theoretical predictions of Cummings & Blackburn, (1991). When the droplets were also rotating, five frequencies were detected; the non-axisymmetric frequencies replaced with split frequencies. The existing theoretical analysis was extended to cover the rotation and precession of the droplet. The theoretical and experiment results showed good agreement as did a comparison with the experimental results of Egry et al (1995), obtained using electromagnetic levitation.

2.3.4 Electro-static

Electrostatic levitation provides another alternative positioning field for performing liquid droplet experiments. Electrically charged droplets can be levitated in an insulating medium with the use of a DC electric field aligned in the direction of the gravitational force.

The electrostatic forces change the dynamics of freely oscillating charged droplets resulting in a different frequency of oscillation. Rayleigh (1882) calculated the frequency of oscillation for an isolated charged droplet and determined that there is a critical level of charge above which the internal electrostatic forces will overcome the surface tension forces causing the droplet to rupture.

Electrostatic levitation is limited to small drops in earthbound experiments because of this limit on the amount of charge the droplet can hold before the internal forces overcome surface tension causing disintegration. In microgravity the confinement (positioning) force is lower and so larger droplets can be used. Electrostatic levitation is not restricted to electrically conducting materials like the electromagnetic (AC) levitation method. The electric field inside the droplet is constant and so there is no electrically induced fluid flow (convection). As there is no internal heating, materials with melting temperatures above room temperature require some other method of melting, usually achieved using lasers. However non-uniform laser heating can result in additional fluid flow effects; Marangoni flow and buoyancy (when gravitational forces are present) driven convection.

Many aspects of a freely oscillating liquid droplet are common to electro-statically levitated droplets but require some additional considerations. Adornato & Brown (1983) performed asymptotic analysis that showed a coupling between the ($L = 2$) and ($L = 3$) modes. Electrostatic forces are nonlinear along the surface causing deformation of the droplet, which is common regardless of the type of positioning force. A Galerkin finite element scheme was used to model droplets with large deformations, the theoretical and numerical surface shape calculations show good agreement.

Electrostatic positioning\confinement has been demonstrated experimentally in both terrestrial and microgravity conditions, Rhim (1987) described the electrostatic-acoustic levitation which was used for the first time to levitate liquid droplets in terrestrial conditions. The possible applications were discussed including the study of liquid droplet dynamics and the measurement of surface tension and viscosity. Rhim et al (1999) performed experiments to measure the surface tension and viscosity of molten metal's using electrostatic levitation. Paradis et al (2005) provided a summary of the work conducted using the electrostatic levitator at JAXA with a discussion of some of the technical challenges of electrostatic levitation including the design of the levitator required to give stable levitation for a wide range of samples. A summary was given for the experiments conducted that included surface tension and viscosity. The surface tension and viscosity measurements were conducted by introducing an ($L = 2$) mode oscillation using

an electric field superimposed on top of the levitating field. The results were found to be in good agreement with known results and new results were obtained for some materials.

2.3.5 Electro-magnetic (AC)

Probably the most widely used method of levitation\confinement is with the use of an AC electrical coil system. The magnetic field produced by the coil system results in induced electric (eddy) currents in an electrically conducting droplet, the combination of which gives rise to the electromagnetic force ($\mathbf{J} \times \mathbf{B}$). The induced electric currents result in Joule (ohmic) heating of the droplet, which it used to melt the material. The electromagnetic force deforms the droplet and creates convection currents that often result in turbulent fluid flow within the droplet.

Electromagnetic levitation has the advantage that it is possible to determine the temperature dependence of thermo-physical properties over wide temperature range due to the suppression of nucleation in the contact-less environment. A major disadvantage of this method of levitation is that the electromagnetic force results in large induced fluid flow that can be turbulent. A static magnetic field can be used to suppress the internal flow reducing the turbulent effects. The effects of the electromagnetic force can also be reduced by performing the experiments in microgravity where the force required to confine (position) the droplet is lower. The oscillation of the droplet can be measured using a photo-detector or through image analysis. When image analysis is used it is not possible to determine the full dynamics of the droplet unless images are taken from more than one direction.

Microgravity experiments have been performed with the use of the TEMPUS facility (container-less electromagnetic processing in weightlessness), built by the German space research agency (DLR). The facility has been used to perform a number of different experiments on the Spacelab missions IML-2 in July 1994 (Second International Microgravity Laboratory on Space Shuttle Columbia) and the MSL-1 (space shuttle flights STS-83 and STS-94) in 1997. The experiments performed include surface tension and viscosity measurements using the oscillating droplet technique. TEMPUS incorporates two sets of AC coils, one set for heating the sample and a second set for positioning the sample;

Figure 2.3. Initially both sets of coils are used and when the sample is melted the heating coils are turned off and just the less invasive positioning coils remain. Oscillations with amplitudes up to 10% are induced in the liquid sample using a pulse of the heating coils. Video cameras are used to capture the droplet dynamics from both top and side views and digital image processing is used to analyse the oscillations. A Fourier transform is applied to the oscillation signal to determine the frequency and the damping rate is determined directly from the signal.

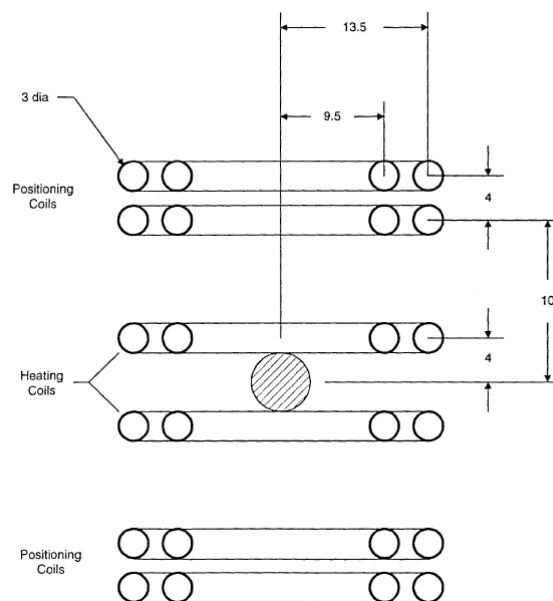


Figure 2.3 – TEMPUS Coils, Berry et al (2005)

Egry et al (1995) reported on experimental measurements of the surface tension of liquid gold (Au) and gold-copper alloy (Au-Cu) as a function of temperature in both ground based and microgravity conditions. The results in microgravity showed a single peak and so the Rayleigh formula was applied when determining the surface tension coefficient. The results of ground based measurements with gold and nickel with a range of different masses show multiple peaks. Analysis of the result using the Rayleigh formula showed a difference in the surface tension depending on the mass of the sample. When the same results were analysed using the Cummings and Blackburn formula (2.16) the mass dependence was eliminated and the value for the surface tension reduced, giving good agreement with the results of the microgravity experiments and also surface tension measurements made using the sessile drop technique.

In Egry et al (1998b) further surface tension measurements were made using the oscillating droplet technique in microgravity. The surface tension as a function of temperature was measured for gold, gold-copper, and zirconium-nickel in experiments using the TEMPUS facility and the results were shown to be in good agreement with earth based experiments with the same technique but only when the ground based measurements were analysed using the Cummings & Blackburn correction formula. The error in the surface tension measurement due to the resolution of power spectra was estimated to be ~3% of the value.

Also Egry et al (1999) reported experimental measurements of surface tension and viscosity made for Co-Pd, and Pd-Cu-Si alloys as a function of temperature.

Egry et al (2001) reviewed the results of material property measurements made during the MSL-1 mission and discussed the design of the next generation of electromagnetic levitator (MSL-EML) that was subsequently developed by the DLR in collaboration with the European Space Agency (ESA) and incorporated in the European Columbus Laboratory on the International Space Station (ISS).

Egry et al (2005b) considered the oscillations of a compound droplet consisting of two immiscible fluids. The theoretical and experimental analysis showed that the surface oscillation contains information on both liquids.

Schwartz (1998) presented the results of mathematical modelling analysis of the TEMPUS facility used to enable and improve the application of the oscillating droplet technique to measure surface tension and viscosity as part of the space shuttle missions.

Egry et al (1998a) discussed progress in non-contact physical property measurements that are required for calculation of the Marangoni number, used to characterise Marangoni convection. Results included surface tension measurements of pure metals in terrestrial conditions. Viscosity measurements were not given due to the lack of correction formulae for terrestrial conditions. The correction formulae are valid for small oscillation amplitudes (perturbations) but are not valid when turbulent damping occurs, which appears to be the case in terrestrial and microgravity conditions.

Brillo and Egry (2007) demonstrated the application of the oscillating droplet technique to the tertiary Cu-Co-Fe alloy in terrestrial gravity with use of the Cummings and Blackburn formula.

Li (2006) investigated the transport phenomena in droplets electro-magnetically levitated using the TEMPUS facility and also electro-statically levitated using the uniform electric field produced by a pair of electrodes. The levitation forces result in internal fluid flow and temperature gradients that produce Marangoni convection. These effects result in a disruption of the measurement of thermo-physical properties and so need to be reduced or eliminated. There is a lack of experimental methods that can be used to view the internal flow and so computational techniques are used. Boundary and finite element methods are used to solve Maxwell's equations and the finite element method for the transport processes (heat and fluid). The logarithmic method was used to determine the viscous damping coefficient. Numerical modelling was completed for both electromagnetic and electrostatic fields, including simulations of the TEMPUS facility. The surface tension coefficient was calculated to within 5-10%. It was concluded that turbulence modelling was an issue, with potential inaccuracy in the low turbulence regime.

The oscillating droplet technique has been used in terrestrial conditions at the National Physical Laboratory (NPL), UK, with Brooks and Queded (2005) producing results for a range of Steels with the Cummings and Blackburn formula applied to correct the results for terrestrial gravity. Brooks and Day (1999) performed measurements of liquid metal droplets, finding a split frequency spectrum consisting of 3-5 modes due to the combination of gravity and the e/m positioning field. The results were adjusted using the Cummings and Blackburn formula providing good agreement with corresponding microgravity results. When the same technique was applied to more complex commercial alloys it was shown that the spectra can consist of 7-9 frequencies, which they attribute to oxide formation on the surface of the droplet.

The application of the oscillating droplet technique to measure viscosity was discussed in the review article by Brooks et al (2005) covering the experimental methods available for measuring viscosity. Lamb's formula for the damping coefficient is valid for force free

drops only; it is based on a spherical droplet (no static deformation). It also assumes that there is no additional damping present, but the electromagnetic force can induce turbulent flow which contributes to the damping of the surface oscillations. “In terrestrial gravity the electromagnetic field deforms the droplet and there are multiple modes of oscillation that makes it hard to isolate the damping of a single mode”. Due to the largely unknown modification to the viscosity as a result of the electromagnetic positioning field, measurements are restricted to microgravity.

Also Egry et al (2005a) performed critical analysis of the oscillating droplet technique considering the influence of translational and/or rotational motion of the sample on the measurement. The methods of measuring the surface oscillation are discussed (photo-detector or video images). The viscosity can be determined from the half width in the peak of the Fourier transform or the log of the square of the surface displacement function (sometimes cross-sectional area or radius are used). Both methods were investigated and also a case where random noise has been added to more closely model the experimental measurement.

Egry (1998) commented that measurement techniques are not entirely satisfactory for liquid metals and that there is some scepticism of the oscillating drop technique because of unexpectedly high surface tension values measured.

Egry et al (1999) commented that despite attempts that have been made to determine the correction to the viscous damping rate due to the electromagnetic positioning field no terrestrial experiments have been reported that use the oscillating drop technique to measure viscosity.

Bardet et al (2006) and Schetelat (2007) use numerical modelling to study the effect of internal flow on the measurement of viscosity in terrestrial experiments. They conclude that the value of viscosity determined using the oscillating drop technique can be overestimated due to the effects of internal flow and results are particularly unreliable when turbulence is present.

Surface oscillation can also be an unwanted effect in thermo-physical property measurement. Density can be measured using the volume determined from the surface profile of a suspended liquid drop. In this case it is important to understand the possible implication of surface oscillation on these measurements. Adachi et al (2008) used AC electromagnetically levitated Silicon droplets to determine the density of the material by calculating the volume from the surface shape. The droplet oscillates in the magnetic field and the change in surface shape needs to be taken into account when determining the volume. The droplet was observed from the side using a high speed camera, Figure 2.4.

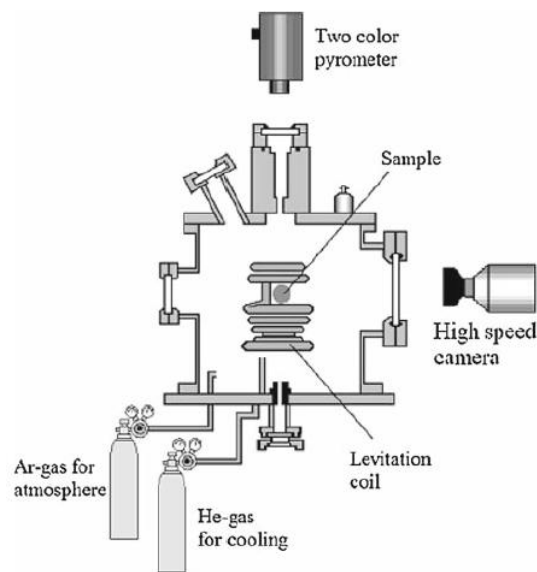


Figure 2.4 – Experimental Apparatus, Adachi et al (2008)

The shape was obtained from images and 2D analysis was used to find the surface modes in terms of Legendre polynomials up to sixth order (including zero). The static deformation causes splitting of the ($L = 2$) mode into its three components as predicted by Cummings and Blackburn, (1991). A separate experiment was performed with a static field ($|\mathbf{B}| = 0$ T to 2 T) used to damp the surface oscillations so that there was no volume fluctuation. Density calculations from the static droplet were found to show good agreement with the result from the oscillating drop, which was corrected using the 2D oscillation analysis.

Fujii et al (2000a & 2000b) performed experiments in a drop-shaft at the Japan Microgravity Centre (JAMIC), which allows experiments in 10^{-5} g for 10 seconds, Figure 2.5a. Quadrupole and dipole coils are used to heat and position the sample, Figure 2.5b

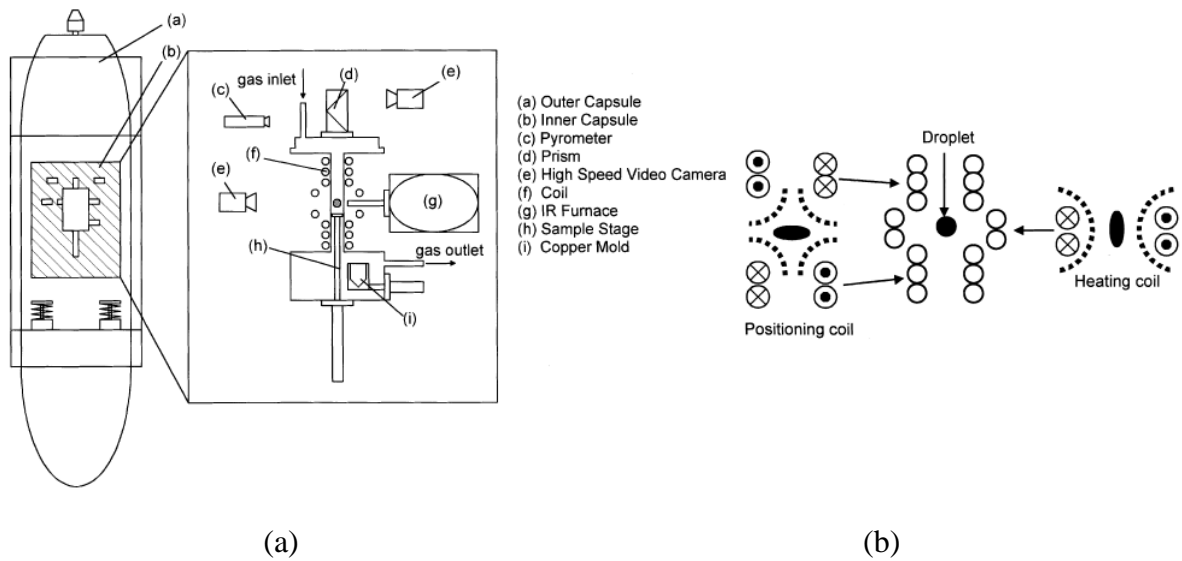


Figure 2.5 – Drop-shaft capsule and EM coils, Fujii et al (2000a & 2000b)

A Silicon droplet was introduced to the cavity and vertical and horizontal translational oscillations were observed. When these oscillations decreased the capsule was released. During the initial stages of freefall the strength of the gravitational force changes from $1g$ to $10^{-5}g$ and so the coil current was adjusted to maintain the central position of the droplet within the capsule. A high speed camera was used instead of a photodiode because it allows more detailed analysis of the droplet dynamics. The positioning and heating coils both produced an ($L = 2$) mode static deformation of the droplet. The electric current is in the opposite direction for the two sets of coils and so the ratio of electric current can be adjusted to minimise the static deformation making the droplet approximately spherical. When the static deformation was minimised a single peak was observed in the power spectra, whereas with only a slight distortion ($\sim 1\%$), five peaks were observed. When there was a significant distortion a single peak dominated the power spectra although the surface tension calculation was incorrect for that case.

Chen and Overfelt (1998) performed experiments to determine the surface tension of Nickel droplets of various sizes using the oscillating droplet technique. The experiments were performed on NASA's KC-135 research aircraft with the use of electromagnetic levitation. The experiments showed good agreement with the oscillation frequency derived by Rayleigh for small droplets but differed for larger droplets.

The surface tension and viscosity measurements are based on theoretical formulae which assume the fluid flow is laminar, but turbulence can occur due to large force gradients and oscillations at the free surface. Berry et al (2005), reported that no experimental method was available to visualise the fluid flow in an electromagnetically levitated metal droplet. An axisymmetric numerical model was used to model the effects of turbulence on a nickel droplet levitated using the TEMPUS facility. The multi-phase volume of fluid (VOF) method was used to represent the free surface. The numerical model employed 3 different methods to model the oscillations, laminar, k- ϵ , and k- ϵ RNG. The maximum velocity was found to be different for each model. The laminar model velocities were too high and resulted in unreasonably high deformation. The effective viscosity for the k- ϵ model was found to be unphysical, but more accurate when more turbulence was present. It was concluded that the k- ϵ RNG model is 'best' suited to modelling turbulent fluid flow in electromagnetically levitated droplets. A large error was found in the surface tension calculation, which was attributed to the VOF method, suggesting that a more robust free surface method is required for modelling droplet oscillations. The viscous damping coefficient determined by the numerical model was found to be ~ 12 times the expected value based on the Lamb formula. Experimental measurements reported for gold were 13 times the actual value, and similar for measurements using Au-Cu (gold-copper) alloy. This suggests that turbulence is the dominant damping mechanism and it is therefore important to develop a better understanding the transition to turbulence in electromagnetic levitation.

2.3.6 Electro-magnetic (DC)

Perhaps the most promising method of confinement for experimental measurements using the oscillating droplet technique is diamagnetic levitation with the use of a high static magnetic field. In this case the weak diamagnetic properties exhibited by many materials can be harnessed by a large magnetic field and used to balance the force of gravity.

Diamagnetism was first discovered by Michael Faraday (1846, 1855) when his experiments revealed a new class of materials with a weak repulsion to an external magnetic field. The repulsive force between the diamagnetic object and the external

magnetic field arises due to electrons in the material adjusting their orbits in the presence of the external magnetic field, inducing a dipole moment in the object. At first sight the theorem by Earnshaw (1842) suggests that stable levitation is not possible, but further analysis reveals that the theorem does not apply to diamagnetic materials. Even though diamagnetic levitation was possible in theory, due to the low magnetic susceptibility of materials, the high magnetic field required for levitation seemed at first impractical. However Braunbek (1942) was able to demonstrate diamagnetic levitation for the first time by suspending bismuth and graphite using an electromagnet.

Diamagnetic levitation of both solid and liquid materials was first demonstrated by Beaunon & Tournier (1991a & 1991b) at the Service National des Champs Intenses in Grenoble. Using a hybrid coil capable of producing a magnetic field up to 27 T in a 5 cm diameter room temperature bore they were able to calculate the magnetic susceptibilities of pure bismuth (Bi) and antimony (Sb) with good agreement with known values. Conditions for levitation were also established for plastic, wood, water, ethanol, and acetone, the observed values in agreement with a calculation using known values of susceptibility. Due to the limited bore size horizontal stability was not confirmed in these experiments, however further experiments were performed for graphite in an 8T magnet with a larger bore (12 cm), in which it was observed that the sample oscillated about the stable levitation point before coming to rest confirming horizontal stability.

In later work Beaunon et al. (1993) performed experiments to investigate some of the applications of diamagnetic levitation to material processing; control convection, phase separation, compensate gravity, and crystal growth.

Diamagnetic levitation of everyday objects received renewed attention following the work of Nobel Prize winning physicist Andrey Geim reported in the popular science magazines *Physics World* (Geim, 1997) and *Physics Today* (Geim (1998) published by the UK and American Institutes of Physics respectively. In these articles images of a hazelnut, a globule of water, and a frog (Figure 2.6) were shown levitated in a 10 T magnet at the University of Nijmegen, Holland.



Figure 2.6 – a) Levitating Frog, b) Levitating Water Droplet
(Geim, 1997)

An overview of diamagnetic levitation along with the conditions for stable levitation was given by Berry & Geim (1997) and Simon & Geim (2000)

The potential energy for a diamagnetic object with constant magnetic susceptibility in combined magnetic and gravitational fields is given by:

$$U_{vol} = \rho g z - \frac{\chi_V |\mathbf{B}|^2}{2 \mu_0} \quad (2.17)$$

The force on the object is related to the gradient of the energy:

$$F_{vol} = -\nabla U_{vol} = -\rho g \mathbf{e}_z + \frac{\chi_V}{\mu_0} \nabla |\mathbf{B}|^2 = 0 \quad (2.18)$$

The equilibrium condition can be given in terms of the magnetic field on the z-axis in the axisymmetric case:

$$\nabla |\mathbf{B}|^2 = -\frac{\mu_0 \rho g}{|\chi_V|} \quad (2.19)$$

The equilibrium condition is dependent on density not mass.

Berry & Geim (1997), gave detailed stability analysis for diamagnetic levitation in an axisymmetric magnetic field. A Taylor series approximation for the magnetic field was used to determine the size of stable region for solenoids with generic dimensions. Linear approximations were given for the magnetic field and the potential energy in terms of the generic solenoid dimensions. The energy contours surrounding the stable equilibrium position for a typical solenoid were presented and the change in characteristics with electric current described. Three key phases of stability were presented;

- 1.) When the magnetic field strength is low the object is not levitated
- 2.) As the field strength is increased a critical point is reached and stable levitation occurs
- 3.) As the field strength is increased further vertical stability is maintained but horizontal stability is lost

The motion of an object displaced from the stable equilibrium by a small amount will receive a restoring force resulting in an oscillation, which it is suggested could be chaotic, something that warrants further study.

Although diamagnetic levitation still introduces additional forces that need to be taken into account in the measurement process it has the advantage that it is cheaper than microgravity experiments performed in space and allows experiments to be performed over longer time-scales than is permitted by the less invasive measurements made in parabolic flights or free-fall experiments. In contrast to this the stable levitation area is small and so the volume that can be levitated is limited. Also, while the resulting total magnetic force on the droplet allows gravity to be compensated, there is some variation in the force and a component that acts towards the axis, which means that it is a good approximation to microgravity conditions but not completely equivalent. Diamagnetic levitation has the advantage over AC levitation that the force acts uniformly throughout the material as opposed to the AC case in which the force is concentrated in the skin layer resulting in induced convection (electromagnetic stirring). The applicability to liquid metals is also a problem as conducting fluids are often paramagnetic and not diamagnetic. Conducting paramagnetic liquids can be levitated by combined AC and DC fields but are unstable in DC fields alone.

Beaugnon et al. (2001), performed experiments relating to surface tension measurement and non-coalescence phenomena in an 18.5T Oxford-Instrument vertical solenoid magnet. The surface tension of ethanol was measured using the oscillating drop technique with droplets of different diameters. The ($L = 2$) mode was induced by air nozzles and a CCD camera was used to record the oscillation, followed by frame by frame analysis to determine the oscillation frequency from surface lighting variation. The magneto-gravitational potential was numerically calculated from winding data of the magnet and used to make estimates for the static deformation and frequency modification due to the external field. The analysis showed that the polar radius was shifted by $\sim 1\%$ and the frequency by $\sim 2\%$. The shift was reduced for smaller droplets and materials with larger surface tension. In a second experiment the non-coalescence phenomenon was observed where two droplets injected in to the levitation zone were observed to bounce but often not coalesce. The effect is attributed to thermo-capillary forces driving an air gap between the two droplets.

Hill & Eaves (2010) of Nottingham University, UK studied the oscillations of a water droplet diamagnetically levitated using a 16.5T vertical bore superconducting magnetic. The experiments were performed in both Nitrogen (no additional magneto-Archimedes buoyancy) and Air (with additional magneto-Archimedes buoyancy) atmospheres for droplets with radii ($R_0 \sim 1\text{cm}$). A pulse of air was used to excite multiple axisymmetric modes with (amplitudes $< 0.05 * R_0$) and so the non-linear effects associated with large amplitude oscillations (significant for amplitudes over $0.1 * R_0$) were not considered to affect the measurements in this case. The oscillations were measured by shining a light from below the magnet and measuring the variation in light using a photo-diode at the top of the magnet. A peak in the power spectra corresponding to the ($L = 1$) translational mode was observed and found to be independent of R_0 , the measured frequencies of the surface modes were found to be ~ 1 Hz higher than those expected for freely oscillating drops due to magneto-gravitational potential trap. The ratio of equatorial (horizontal) diameter to the polar (vertical) diameter were used to determine the static deformation of the droplet, which was found to be ‘almost spherical’, suggesting that the surface tension force is more dominant than the magnetic and gravitational force in this case. The effects of viscosity cause a decrease in frequency and can be determined by solution of the Chandrasekhar equation for the complex frequencies. In this case they are considered to be small in

comparison with the shift in frequency due to the trapping potential and so the results are unaffected. The effect of viscosity can be determined by comparison of exponential decay.

In addition to the experimental work the theory for oscillating droplets was extended to include the effects of an arbitrary axisymmetric magneto-gravitational potential. The analysis included the modified pressure, velocity potential, static deformation, and modified oscillation frequency of the droplet.

The numerical study of a diamagnetic droplet electromagnetically levitated using the DC field from a solenoid was presented by Easter, Bojarevics, and Pericleous (2011a) using the three-dimensional spectral collocation model developed in the present work. A direct comparison was made between the three-dimensional model and the axisymmetric model of Bojarevics and Pericleous (2003), showing good agreement for cases with axisymmetric conditions. Further cases were presented with non-axisymmetric initial conditions.

Weilert et al. (1996), performed experiments to study the dynamics of super fluid liquid helium droplets. When two droplets are introduced into the bore of the magnet they are pushed towards the energy minimum. While they could be expected to coalesce they are often observed to bounce and remain separate for some time (non-coalescence phenomenon). The non-coalescence phenomenon is explained by the slow evaporation of liquid, isolated droplets are found to evaporate uniformly, whereas for two drops the vapour escapes between the drops causing increase in pressure keeping the drops separate. An estimation of the shape deformation can be made from the surface curvature but the sample could only be viewed from above and so the shape could not be verified.

Weilert, Whitaker et al. (1997), perform experiments with temperatures as low as 1.5K, in which the droplets are observed to go up to three minutes without coalescing. The non-coalescence is only observed above the super-fluid transition temperature. When the two droplets finally coalesce they display complex oscillations consisting of a superposition of different modes sometimes rotation is also observed. The non-coalescence effect is attributed to the existence of a vapour layer due to evaporation separating the droplets. However this cannot happen in a super-fluid and so super fluid drops are always observed to coalesce in the practical experiments.

Some common characteristics of levitated droplets were observed; when the droplets were introduced to the solenoid there was an initial translational oscillation with a frequency of approximately 1 Hz. The drops oscillated around the energy minimum before coming to rest after approximately 10 seconds. The surface shape oscillations were also observed to damp out after a few seconds. The oscillations were induced by moving a ferromagnetic object outside the cryostat

Calculations were made for the magnetic field with the potential trap assumed to have ($L = 0$) and ($L = 2$) components, allowing the static deformation to be calculated, however the distortions predicted could not be observed because it was only possible to view the droplet from above the magnet. The calculations showed that surface tension dominated for small drops and so static deformation was small whereas large drops were quite deformed.

Whitaker, Weilert et al. (1998a & 1998b), studied the surface oscillation and rotation in Helium II droplets using an AC electric field to excite the oscillation and rotation. The oscillations were measured by capturing light from a laser using a photo-diode. Oscillations up to mode ($L = 15$) were observed. The damping of the oscillations was calculated using two different methods 1) width of the resonance peak, and 2) decay time. It was found that there was a larger energy loss than can be explained by viscosity indicating that another mechanism is in effect. Rotating drops were also observed.

The experimental work by this group highlight a new dimension for the oscillating drop technique and Whitaker (1999), extended the existing theoretical models for oscillation frequency, static deformation, and damping rate to incorporate the superfluid case using the two-fluid Landau model.

2.3.6.1 Conducting Droplet in a DC Electromagnetic Field

In a recent paper Priede (2011), considered the effect of a constant magnetic field on the oscillation frequency and damping rate of an electrically conducting drop. The magnetic field is a constant static field aligned with the z-axis, given in spherical coordinates by:

$$\mathbf{B}(r, \theta, \phi) = (B_0 \cos \theta, -B_0 \sin \theta, 0) \quad (2.20)$$

Where B_0 is the magnitude of the constant magnetic field. The magnetic field is shown to significantly alter the dynamics of the droplet with some interesting results. There are two distinct cases; the longitudinal modes when $(L - M)$ is odd and the transversal modes when $(L - M)$ is even. The frequencies for the odd and even modes respectively are given by:

$$\omega_L^M = \sqrt{\frac{(L-1)(L+2)\Gamma}{\rho R_0^3}} \quad (\text{Odd}) \quad (2.21)$$

$$\omega_L^M = M \sqrt{\frac{(L-1)(L+2)\Gamma}{L(L+1)-M^2} \frac{\Gamma}{\rho R_0^3}} \quad (\text{Even}) \quad (2.22)$$

The damping constant consists of two components, damping due to the magnetic field and damping due to viscosity. The damping contribution of the magnetic field for the odd and even modes respectively are given by:

$$\gamma_L^M = \frac{1}{6}(L-1)(L+2)((L-1)(L+2) + 2M^2) \frac{\sigma B_0^2 R_0^3}{\Gamma} \quad (2.23)$$

$$\gamma_L^M = \frac{(L-1)(L+2)(L^2 - M^2)((L+1)^2 - M^2)(3L(L+1) - 2M^2)}{6(L(L+1) - M^2)^2} \frac{\sigma B_0^2 R_0^3}{\Gamma} \quad (2.24)$$

The contribution to the damping constant due to viscous forces is given by:

$$\gamma_L^M = C_L^M \frac{\nu}{R_0^2} \quad (2.25)$$

Where (C_L^M) are coefficients determined by evaluation of an integral without a closed form solution. In the present work we are only concerned with the low order modes with coefficients:

$$C_2^1 = \frac{5}{2} \qquad C_2^2 = 5 \qquad C_3^0 = \frac{35}{3} \qquad (2.26)$$

In Easter, Bojarevics, and Pericleous (2011b), the three-dimensional spectral collocation model developed in the present work and the axisymmetric model of Bojarevics and Pericleous (2003) were used to model the surface oscillations of an electrically conducting droplet in a strong DC electromagnetic field. The numerical results showed that the strong DC field can have a significant impact on the surface oscillation frequencies and damping rates depending on the type of oscillation mode. The qualitative and quantitative behaviour of the droplet were shown to be in good agreement with the theoretical calculations of Priede (2011).

2.4 Summary \ Conclusions

The dynamics of a liquid drop has been the subject of much analysis, which has provided a good level of understanding of the internal fluid flow and free surface interaction.

In the case of freely oscillating droplets the theoretical analysis has been used to show that to a good first approximation the free surface shape can be represented by a series expansion of spherical harmonics. When displaced by a small amount, the free surface performs damped harmonic oscillation about the equilibrium spherical shape with frequency and damping rate determined in terms of the droplet size, material properties, and type of oscillation mode. The damping coefficient is only determined in closed form for the low viscosity case, but can be determined for all cases by solving a transcendental equation, which reveals that different types of damping occur depending on the size of the droplet. The theoretical, numerical, and experimental work conducted for liquid droplet oscillations all suggest that there are nonlinear components even at small amplitude. This can easily be explained by considering mass conservation, for an incompressible fluid this is equivalent to volume conservation. Assuming that a normal mode oscillation of the spherical harmonic form and then calculating the volume of the droplet reveals a variation in the volume, which exists for any amplitude no matter how small. The theoretical analysis of Tsamopoulos & Brown (1983) for inviscid droplets shows that second order corrections proportional to the square of the amplitude, which reduce this variation in

volume. Other nonlinear effects include a decrease in frequency with increasing amplitude of oscillation. The numerical modelling of freely oscillating droplets is often restricted to axisymmetric cases and lack the accuracy required to fully resolve the free surface behaviour.

The relationship between surface tension coefficient and oscillation frequency and viscous damping coefficient and surface oscillation damping rate form the basis of the oscillating droplet measurement technique. This technique in combination with the results for freely oscillating droplets is only applicable when any external forces acting on the droplet are negligible. This has led to experiments being performed in low gravity environments; however it is more desirable to perform the experiments in terrestrial conditions. A variety of different external forces have been used to confine the droplet in terrestrial conditions but due to the larger forces required to balance gravity the oscillation frequencies and damping rates are modified. The theoretical understanding of the impact of these external forces is limited, which has hindered the application of the technique in terrestrial conditions. In the case of a high DC field the effects of the positioning force are small and so this provides a good opportunity for the oscillating droplet technique. However in the case of conducting droplets the external field can greatly alter the dynamics of the droplet depending on the type of surface shape oscillation.

3. Numerical Model

3.1 Overview

The numerical modelling of liquid droplet dynamics will be carried out using a numerical code with a coordinate transformation that accurately tracks the position of the surface. The model follows the same approach as the axisymmetric modelling of Bojarevics and Pericleous (2003) but extends the model to include three-dimensional effects. The model solves the Navier-Stokes equations, which are outlined in §3.2. The coordinate transformation that is used for direct tracking of the surface position requires modified derivative operators, which are derived in §3.3. The unit normal and tangential unit vectors for the free surface are derived in §3.4 and used in the boundary conditions outlined in §3.5. In §3.6 an overview of the numerical method is given along with an explanation of how the coordinate transformation is applied and the resulting equations are discretised and implemented.

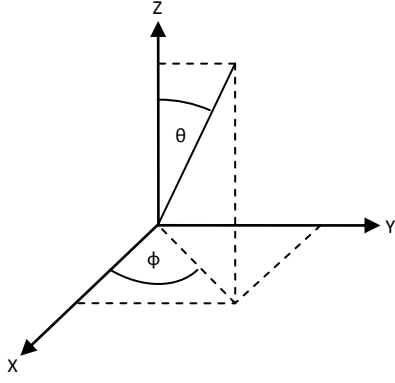
3.2 Fluid Dynamics

The equations to be modelled are the incompressible Navier-Stokes equations for constant viscosity. These equations describe conservation of mass and momentum and are given in general vector format valid in any orthogonal coordinate system inertial reference frame by:

$$\frac{\partial \mathbf{V}}{\partial t} + (\mathbf{V} \cdot \nabla) \mathbf{V} = -\frac{1}{\rho} \nabla P + \nu \nabla \cdot (\nabla \mathbf{V} + \nabla \mathbf{V}^T) + \frac{1}{\rho} \mathbf{F}_{vol} \quad (3.1)$$

$$\nabla \cdot \mathbf{V} = 0 \quad (3.2)$$

It is convenient to first consider the equations in spherical coordinates and then apply a coordinate transformation to transform the deformed droplet onto a sphere. The spherical coordinate system is illustrated in Figure 3.1.



$$x = r \sin \theta \cos \phi$$

$$y = r \sin \theta \sin \phi$$

$$z = r \cos \theta$$

Figure 3.1 – Spherical Coordinate System

In order to solve the equations numerically they need to be solved either as a coupled system or solved separately using an iterative technique. If the equations are solved separately then the continuity equation must be replaced by an explicit equation for pressure or a pressure correction equation. The Navier-Stokes equations in spherical coordinates are available from a number of sources: Landau and Lifshitz (1987), Hughes et al (1999), Happel and Brenner (1965), and Batchelor (1967). The momentum equations are given by:

$$\begin{aligned} \frac{\partial u}{\partial t} + \left(u \frac{\partial u}{\partial r} + \frac{v}{r} \frac{\partial u}{\partial \theta} + \frac{w}{r \sin \theta} \frac{\partial u}{\partial \phi} - \frac{v^2}{r} - \frac{w^2}{r} \right) \\ = -\frac{1}{\rho} \left(\frac{\partial P}{\partial r} \right) + \nu \left(\nabla^2 u - \frac{2u}{r^2} - \frac{2}{r^2} \frac{\partial v}{\partial \theta} - \frac{2v \cot \theta}{r^2} - \frac{2}{r^2 \sin \theta} \frac{\partial w}{\partial \phi} \right) \\ + \frac{1}{\rho} f_r \end{aligned} \quad (3.3)$$

$$\begin{aligned} \frac{\partial v}{\partial t} + \left(u \frac{\partial v}{\partial r} + \frac{v}{r} \frac{\partial v}{\partial \theta} + \frac{w}{r \sin \theta} \frac{\partial v}{\partial \phi} + \frac{uv}{r} - \frac{w^2 \cot \theta}{r} \right) \\ = -\frac{1}{\rho} \left(\frac{1}{r} \frac{\partial P}{\partial \theta} \right) + \nu \left(\nabla^2 v + \frac{2}{r^2} \frac{\partial u}{\partial \theta} - \frac{v}{r^2 \sin^2 \theta} - \frac{2 \cot \theta}{r^2 \sin \theta} \frac{\partial w}{\partial \phi} \right) \\ + \frac{1}{\rho} f_\theta \end{aligned} \quad (3.4)$$

$$\begin{aligned}
\frac{\partial w}{\partial t} + \left(u \frac{\partial w}{\partial r} + \frac{v}{r} \frac{\partial w}{\partial \theta} + \frac{w}{r \sin \theta} \frac{\partial w}{\partial \phi} + \frac{uw}{r} + \frac{vw \cot \theta}{r} \right) \\
= -\frac{1}{\rho} \left(\frac{1}{r \sin \theta} \frac{\partial P}{\partial \phi} \right) \\
+ v \left(\nabla^2 w - \frac{w}{r^2 \sin^2 \theta} + \frac{2}{r^2 \sin \theta} \frac{\partial u}{\partial \phi} + \frac{2 \cos \theta}{r^2 \sin^2 \theta} \frac{\partial v}{\partial \phi} \right) + \frac{1}{\rho} f_\phi
\end{aligned} \tag{3.5}$$

Where the Laplacian operator for a scalar function is given in spherical coordinates by:

$$\nabla^2 = \frac{\partial^2}{\partial r^2} + \frac{2}{r} \frac{\partial}{\partial r} + \frac{1}{r^2} \frac{\partial^2}{\partial \theta^2} + \frac{\cot \theta}{r^2} \frac{\partial}{\partial \theta} + \frac{1}{r^2 \sin^2 \theta} \frac{\partial^2}{\partial \phi^2} \tag{3.6}$$

If the equations are solved as a coupled system then the continuity equation can be used:

$$\frac{\partial u}{\partial r} + \frac{2u}{r} + \frac{1}{r} \frac{\partial v}{\partial \theta} + \frac{v \cot \theta}{r} + \frac{1}{r \sin \theta} \frac{\partial w}{\partial \phi} = 0 \tag{3.7}$$

If the equations are solved separately then the Poisson equation for pressure can be used, which is obtained by taking the divergence of (3.1):

$$\frac{1}{\rho} \nabla^2 P = -\nabla \cdot (\mathbf{V} \cdot \nabla) \mathbf{V} + \frac{1}{\rho} \nabla \cdot \mathbf{F}_{vol} \tag{3.8}$$

3.3 Co-ordinate Transformation

The shape of the droplet can be defined by the radial position of the surface in the spherical coordinate system. The radial position is defined by the deviation from a sphere of radius (R_0) using a function S :

$$r_s = R_0 [1 + S(\theta, \phi, t)] \tag{3.9}$$

A coordinate transformation is used so that the problem is equivalent to that of a fixed sphere. The space and time variables in spherical coordinates are related to those in the transformed coordinate system by the following relationships:

$$\bar{r} = \frac{r}{R_0 [1 + S(\theta, \phi, t)]} \quad \bar{\theta} = \theta \quad \bar{\phi} = \phi \quad \bar{t} = t \quad (3.10)$$

The coordinate transformation is performed by replacing the derivatives with the relevant transformed derivative operators that are obtained by applying the chain rule to the transformed variables. The resulting first derivative operators are given by:

$$\frac{\partial}{\partial r} = \frac{1}{R_0 (1 + S)} \frac{\partial}{\partial \bar{r}} \quad (3.11)$$

$$\frac{\partial}{\partial \theta} = \frac{\partial}{\partial \bar{\theta}} - \frac{\bar{r}}{(1 + S)} \frac{\partial S}{\partial \bar{\theta}} \frac{\partial}{\partial \bar{r}} \quad (3.12)$$

$$\frac{\partial}{\partial \phi} = \frac{\partial}{\partial \bar{\phi}} - \frac{\bar{r}}{(1 + S)} \frac{\partial S}{\partial \bar{\phi}} \frac{\partial}{\partial \bar{r}} \quad (3.13)$$

$$\frac{\partial}{\partial t} = \frac{\partial}{\partial \bar{t}} - \frac{\bar{r}}{(1 + S)} \frac{\partial S}{\partial \bar{t}} \frac{\partial}{\partial \bar{r}} \quad (3.14)$$

The second derivatives are also required for the spatial variables and are obtained by repeated application of the first derivative operators:

$$\frac{\partial^2}{\partial r^2} = \frac{1}{R_0^2 (1 + S)^2} \frac{\partial^2}{\partial \bar{r}^2} \quad (3.15)$$

$$\begin{aligned} \frac{\partial^2}{\partial \theta^2} = & \frac{\partial^2}{\partial \bar{\theta}^2} + \left[(1 + \bar{r}) \left(\frac{1}{(1 + S)} \frac{\partial S}{\partial \bar{\theta}} \right)^2 - \frac{\bar{r}}{(1 + S)} \frac{\partial^2 S}{\partial \bar{\theta}^2} \right] \frac{\partial}{\partial \bar{r}} \\ & + \left[\left(\frac{1}{(1 + S)} \frac{\partial S}{\partial \bar{\theta}} \right)^2 \bar{r} \right] \frac{\partial^2}{\partial \bar{r}^2} - \left[\frac{2 \bar{r}}{(1 + S)} \frac{\partial S}{\partial \bar{\theta}} \right] \frac{\partial}{\partial \bar{r}} \frac{\partial}{\partial \bar{\theta}} \end{aligned} \quad (3.16)$$

$$\begin{aligned} \frac{\partial^2}{\partial \phi^2} = \frac{\partial^2}{\partial \bar{\phi}^2} + & \left[(1 + \bar{r}) \left(\frac{1}{(1 + S)} \frac{\partial S}{\partial \bar{\phi}} \right)^2 - \frac{\bar{r}}{(1 + S)} \frac{\partial^2 S}{\partial \bar{\phi}^2} \right] \frac{\partial}{\partial \bar{r}} \\ & + \left[\left(\frac{1}{(1 + S)} \frac{\partial S}{\partial \bar{\phi}} \right)^2 \bar{r} \right] \frac{\partial^2}{\partial \bar{r}^2} - \left[\frac{2 \bar{r}}{(1 + S)} \frac{\partial S}{\partial \bar{\phi}} \right] \frac{\partial}{\partial \bar{r}} \frac{\partial}{\partial \bar{\phi}} \end{aligned} \quad (3.17)$$

Further details are given in Appendix A.

3.4 Unit Vectors

The boundary conditions and the movement of the surface are dependent on the unit vectors normal and tangential to the deformed surface position. The unit vectors can be derived in terms of the surface position (3.9). The normal vector is obtained by taking the gradient of the function $F = 0$, which is a parametric representation of points on the surface:

$$\mathbf{e}_n = \frac{\nabla F}{|\nabla F|} \quad (3.18)$$

$$\text{Where } F(r, \theta, \phi) = r - R_0(1 + S) = 0 \quad (3.19)$$

Applying the gradient operator in spherical coordinates to the function F gives the unit vector normal to the surface:

$$\mathbf{e}_n = \frac{(1 + S) \mathbf{e}_r - \frac{\partial S}{\partial \theta} \mathbf{e}_\theta - \frac{1}{\sin \theta} \frac{\partial S}{\partial \phi} \mathbf{e}_\phi}{\sqrt{(1 + S)^2 + \left(\frac{\partial S}{\partial \theta} \right)^2 + \left(\frac{1}{\sin \theta} \frac{\partial S}{\partial \phi} \right)^2}} \quad (3.20)$$

A vector in the plane tangential to the surface can be obtained by taking the derivative with respect to theta of the surface position vector:

$$\mathbf{r}_s(r, \theta, \phi) = R_0(1 + S) \mathbf{e}_r \quad (3.21)$$

Taking into account the derivative of the spherical coordinate unit vector \mathbf{e}_r gives:

$$\frac{\partial r_s(r, \theta, \phi)}{\partial \theta} = R_0 \frac{\partial S}{\partial \theta} \mathbf{e}_r + R_0(1 + S) \mathbf{e}_\theta + 0 \mathbf{e}_\phi \quad (3.22)$$

The tangent vector is normalised to give:

$$\mathbf{e}_{\tau 1} = \frac{\frac{\partial S}{\partial \theta} \mathbf{e}_r + (1 + S) \mathbf{e}_\theta + 0 \mathbf{e}_\phi}{\sqrt{(1 + S)^2 + \left(\frac{\partial S}{\partial \theta}\right)^2}} \quad (3.23)$$

A second vector in the tangent plane that is orthogonal to both the unit normal and the first tangential vector can be obtained using:

$$\mathbf{e}_{\tau 2} = \frac{\mathbf{e}_n \times \mathbf{e}_{\tau 1}}{|\mathbf{e}_n \times \mathbf{e}_{\tau 1}|} \quad (3.24)$$

Evaluating the cross product gives the second tangential vector:

$$\mathbf{e}_{\tau 2} = \frac{\frac{(1 + S)}{\sin \theta} \frac{\partial S}{\partial \phi} \mathbf{e}_r - \frac{1}{\sin \theta} \frac{\partial S}{\partial \theta} \frac{\partial S}{\partial \phi} \mathbf{e}_\theta + \left[(1 + S)^2 + \left(\frac{\partial S}{\partial \theta}\right)^2 \right] \mathbf{e}_\phi}{\sqrt{\left[(1 + S)^2 + \left(\frac{\partial S}{\partial \theta}\right)^2 \right] \left[(1 + S)^2 + \left(\frac{\partial S}{\partial \theta}\right)^2 + \left(\frac{1}{\sin \theta} \frac{\partial S}{\partial \phi}\right)^2 \right]}} \quad (3.25)$$

3.5 Boundary Conditions

The boundary conditions for the freely oscillating droplet are given in terms of the normal and tangential stresses at the surface and the kinematic condition for the surface displacement.

3.5.1 Kinematic Boundary Condition

The movement of the surface is defined by the kinematic condition:

$$\frac{\partial r_s}{\partial t} \cdot \mathbf{e}_n = \mathbf{V} \cdot \mathbf{e}_n \quad (3.26)$$

Using the definitions for the surface position vector (3.9) and the unit vector normal to the surface (3.20) the kinematic condition is given by:

$$R_0 \frac{\partial S}{\partial t} = u - \left(\frac{1}{(1+S)} \frac{\partial S}{\partial \theta} \right) v - \left(\frac{1}{(1+S) \sin \theta} \frac{\partial S}{\partial \phi} \right) w \quad (3.27)$$

3.5.2 Stress Boundary Conditions

The boundary normal and tangential stresses at the surface are determined by the surface unit vectors and the stress tensor:

$$\mathbf{e}_n \cdot \Pi \cdot \mathbf{e}_n = \Gamma K \quad (3.28)$$

$$\mathbf{e}_n \cdot \Pi \cdot \mathbf{e}_{\tau 1} = 0 \quad (3.29)$$

$$\mathbf{e}_n \cdot \Pi \cdot \mathbf{e}_{\tau 2} = 0 \quad (3.30)$$

The surface curvature (K) in (3.28) is derived in terms of the surface shape (see §3.5.4)

3.5.3 General Representation for Stress

The stress boundary condition in a generic form using the vectors \mathbf{A} and \mathbf{B} to represent the unit vectors is given by:

$$\mathbf{A} \cdot \Pi \cdot \mathbf{B} = \sum_{i=1}^{i=3} \sum_{j=1}^{j=3} a_i \Pi_{i,j} b_j \quad (3.31)$$

The stress tensor is linearly related to the strain rate tensor and the pressure by:

$$\Pi_{i,j} = 2 \nu \rho e_{i,j} - P \delta_{i,j} \quad (3.32)$$

The arbitrary vectors \mathbf{A} and \mathbf{B} are given in spherical coordinates by:

$$\mathbf{A} = (a_r, a_\theta, a_\phi) \quad \mathbf{B} = (b_r, b_\theta, b_\phi) \quad (3.33)$$

Evaluating (3.31) in spherical coordinates and taking into account the symmetry of the stress tensor gives:

$$\begin{aligned} \mathbf{A} \cdot \Pi \cdot \mathbf{B} = 2 \nu \rho [& (a_r b_r) e_{rr} + (a_\theta b_\theta) e_{\theta\theta} + (a_\phi b_\phi) e_{\phi\phi} \\ & + (a_r b_\theta + a_\theta b_r) e_{r\theta} + (a_r b_\phi + a_\phi b_r) e_{r\phi} \\ & + (a_\theta b_\phi + a_\phi b_\theta) e_{\theta\phi}] - P (a_r b_r + a_\theta b_\theta + a_\phi b_\phi) \end{aligned} \quad (3.34)$$

Where the components of the strain rate tensor are given by:

$$\begin{aligned} e_{rr} &= \frac{\partial u}{\partial r} & e_{\theta\theta} &= \frac{1}{r} \frac{\partial v}{\partial \theta} + \frac{u}{r} \\ e_{\phi\phi} &= \frac{1}{r \sin \theta} \frac{\partial w}{\partial \phi} + \frac{u}{r} + \frac{v \cot \theta}{r} & e_{r\theta} = e_{\theta r} &= \frac{1}{2} \left[\frac{\partial v}{\partial r} - \frac{v}{r} + \frac{1}{r} \frac{\partial u}{\partial \theta} \right] \\ e_{r\phi} = e_{\phi r} &= \frac{1}{2} \left[\frac{1}{r \sin \theta} \frac{\partial u}{\partial \phi} - \frac{w}{r} + \frac{\partial w}{\partial r} \right] & e_{\theta\phi} = e_{\phi\theta} &= \frac{1}{2} \left[\frac{1}{r} \frac{\partial w}{\partial \theta} - \frac{\cot \theta}{r} \frac{w}{r} \right. \\ & & & \left. + \frac{1}{r \sin \theta} \frac{\partial v}{\partial \phi} \right] \end{aligned} \quad (3.35)$$

Using the components of the strain rate tensor, the boundary condition can be re-arranged such that the terms relating to the velocity components and pressure are collected together providing a convenient form that is applicable to the normal and tangential stress conditions:

$$\begin{aligned}
\mathbf{A} \cdot \boldsymbol{\Pi} \cdot \mathbf{B} = & 2 \nu \rho \left[(a_r b_r) \left[\frac{\partial u}{\partial r} \right] + (a_r b_\theta + a_\theta b_r) \frac{1}{2} \left[\frac{1}{r} \frac{\partial u}{\partial \theta} \right] \right. \\
& + (a_r b_\phi + a_\phi b_r) \frac{1}{2} \left[\frac{1}{r \sin \theta} \frac{\partial u}{\partial \phi} \right] + (a_\theta b_\theta + a_\phi b_\phi) \left[\frac{u}{r} \right] \\
& + (a_r b_\theta + a_\theta b_r) \frac{1}{2} \left[\frac{\partial v}{\partial r} - \frac{v}{r} \right] + (a_\theta b_\theta) \left[\frac{1}{r} \frac{\partial v}{\partial \theta} \right] \\
& + (a_\theta b_\phi + a_\phi b_\theta) \frac{1}{2} \left[\frac{1}{r \sin \theta} \frac{\partial v}{\partial \phi} \right] + (a_\phi b_\phi) \left[\frac{v \cot \theta}{r} \right] \\
& + (a_r b_\phi + a_\phi b_r) \frac{1}{2} \left[\frac{\partial w}{\partial r} - \frac{w}{r} \right] \\
& + (a_\theta b_\phi + a_\phi b_\theta) \frac{1}{2} \left[\frac{1}{r} \frac{\partial w}{\partial \theta} - \frac{\cot \theta}{r} w \right] \\
& \left. + (a_\phi b_\phi) \left[\frac{1}{r \sin \theta} \frac{\partial w}{\partial \phi} \right] \right] - P (a_r b_r + a_\theta b_\theta + a_\phi b_\phi)
\end{aligned} \tag{3.36}$$

As with the previous equations the derivatives and the radial coordinate need to be replaced by their transformed counterpart. The components of the vectors \mathbf{A} and \mathbf{B} need to be replaced by their unit vector components (3.20), (3.23), (3.25).

3.5.4 Curvature

The normal stress boundary condition is proportional to the curvature of the surface with constant of proportionality given by the surface tension coefficient. The curvature of the surface can be determined in terms of the surface position function (3.9) by taking the divergence of the normal vector (3.20):

$$K = \nabla \cdot \mathbf{e}_n \tag{3.37}$$

The resulting expression for the curvature is given by:

$$\begin{aligned}
K = \frac{1}{|\nabla F| R_0} & \left\{ 2 - \frac{1}{(1+S)} \left[\frac{\partial^2 S}{\partial \theta^2} + \frac{\cos \theta}{\sin \theta} \frac{\partial S}{\partial \theta} + \frac{1}{\sin^2 \theta} \frac{\partial^2 S}{\partial \phi^2} \right] \right\} \\
& + \frac{1}{|\nabla F|^3 R_0} \frac{1}{(1+S)} \left\{ \left(\frac{\partial S}{\partial \theta} \right)^2 \left[(1+S) + \frac{\partial^2 S}{\partial \theta^2} \right] \right. \\
& + \left. \left(\frac{1}{\sin^2 \theta} \frac{\partial S}{\partial \theta} \frac{\partial S}{\partial \phi} \right) \left[\frac{\partial^2 S}{\partial \theta \phi} - \frac{\cos \theta}{\sin \theta} \frac{\partial S}{\partial \phi} \right] \right. \\
& \left. + \frac{1}{\sin^2 \theta} \frac{\partial S}{\partial \phi} \left[(1+S) \frac{\partial S}{\partial \phi} + \frac{\partial S}{\partial \theta} \frac{\partial^2 S}{\partial \theta \phi} + \frac{1}{\sin^2 \theta} \frac{\partial S}{\partial \phi} \frac{\partial^2 S}{\partial \phi^2} \right] \right\}
\end{aligned} \tag{3.38}$$

$$\text{Where } |\nabla F| = \sqrt{(1+S)^2 + \left(\frac{\partial S}{\partial \theta} \right)^2 + \left(\frac{1}{\sin \theta} \frac{\partial S}{\partial \phi} \right)^2} \tag{3.39}$$

3.6 Implementation

3.6.1 Overview

The numerical method chosen is the pseudo-spectral collocation method due to its high accuracy. There are several ways of implementing the collocation method:

- Modal - The system of equations is solved for the series coefficients and then the series is summed to find the actual physical values
- Nodal - The system of equations is solved directly for the actual physical values
- Combined Modal and Nodal – A combination of the modal and nodal implementations that can produce a more efficient code when a fast transformation method is available to change between the nodal and modal representations.

When solving equations that involve variable coefficients or nonlinear terms the increase in efficiency of the combined implementation is most advantageous, Boyd (2000) and Fornberg (1996). Fornberg (1996) explains the equivalence of the collocation method and an n^{th} order finite difference scheme, which is clear when considering the nodal implementation. The nodal approach is also taken by the key texts on spectral methods that include worked examples \ details of implementation (Trefethen (2000) and Kopriva (2009)).

It is almost essential to solve the coupled equations using an iterative method when there are four coupled equations as in the three-dimensional case because direct inversion is slow and requires too much memory even with a coarse grid. In this case the Navier-Stokes equations are split and the continuity equation is replaced with the Poisson equation for the pressure, coupled and splitting methods are described by Canuto et al (2007).

Due to the ease of implementation the nodal implementation is used and the general approach is based on the example of Kopriva (2009), in which the scalar Laplace equation is solved in Cartesian coordinates with the bi-conjugate gradient stabilized method and a second order finite difference method used as a pre-conditioner. Chebyshev basis functions are chosen for the radial direction and Fourier basis functions for the angular directions. An outline of the numerical model process is illustrated in Figure 3.2. The process can be split into four main sections; initialisation, pre-solve, iterative solution, and post-solve.

The initialisation step involves setting all variables and parameters for the model, the remaining steps form the transient loop which repeats for a given number of time-steps NDT to produce a simulation with a physical time of $T = NDT * DT$, where DT is the time increment for the implicit Euler method. The pre-solve step involves evaluation of the variables that are constant for the given time-step. The iterative solution step consists of an outer iteration loop containing solvers for each of the four uncoupled fluid flow variables. The Poisson equation is solved for pressure, then the momentum equations for the velocity components, u , v , and w . Each of these equations is solved using the iterative bi-conjugate gradient stabilised method with a second order finite difference pre-conditioner. The post-solve step involves the calculation of the new surface position and creation of the output file(s).

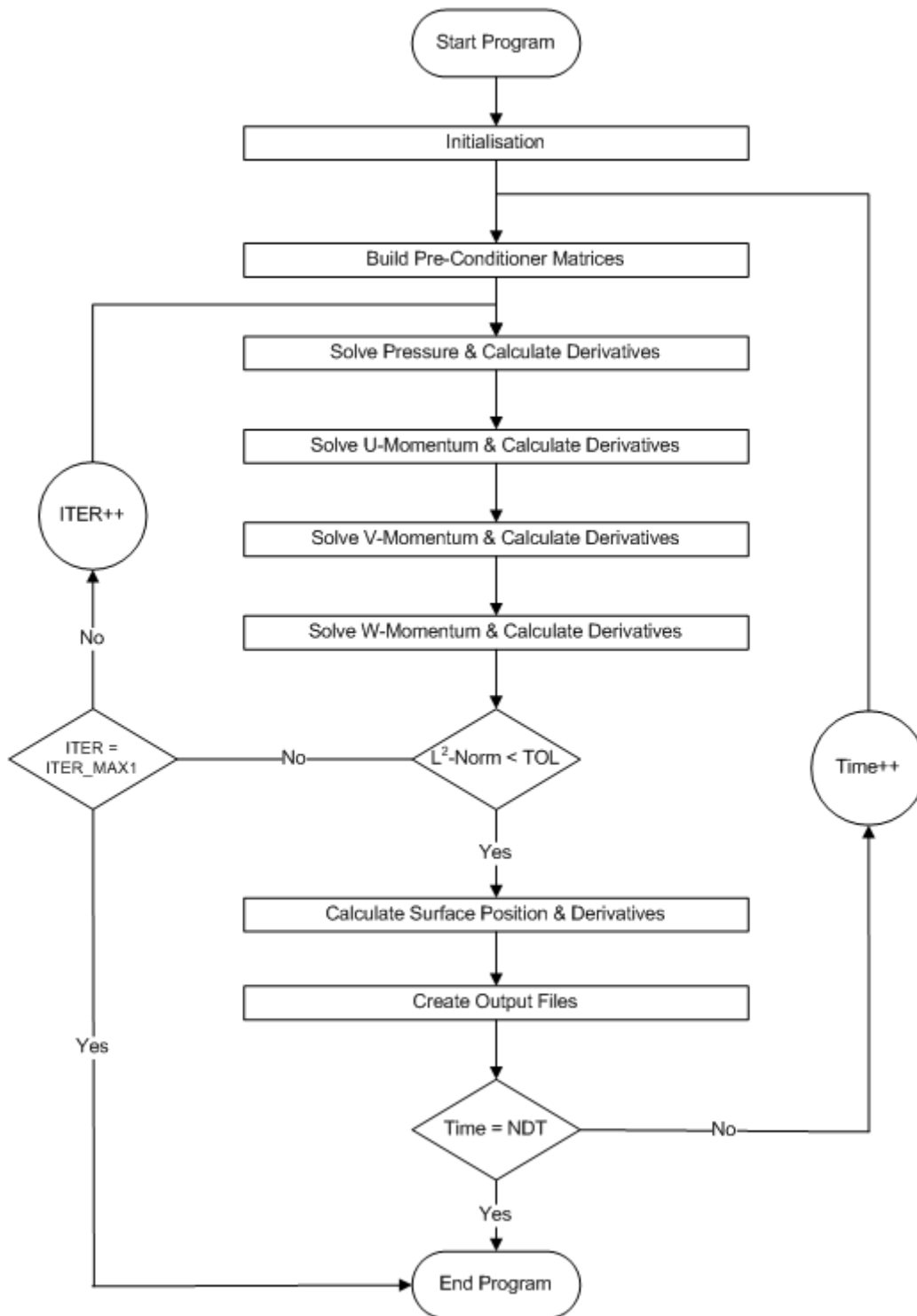


Figure 3.2 – Numerical Model Process

3.6.2 Initialisation

The first part of the initialisation step involves defining the quantities that remain constant for the length of the simulation;

- Material Properties: surface tension coefficient (Γ), density (ρ), kinematic viscosity (ν), and magnetic susceptibility (χ)
- Physical Parameters: gravitational constant (g), permeability of free space (μ_0)
- Transient Parameters: number of time-steps (NDT), time-step increment (DT)
- Outer Iteration Loop Parameters: maximum number of iterations (ITER_MAX1), L²-norm tolerance for pressure (P_TOL1), L²-norm tolerance for velocity (V_TOL1)
- Solver Iteration Parameters: maximum number of iterations (ITER_MAX2), L²-norm tolerance for Poisson equation (P_TOL2), L²-norm tolerance for momentum equations (V_TOL2)
- Output File Parameters: output file prefix (OutputNo), output frequency (OutputFreq)

The mesh density is defined by the number of points in each of the orthogonal coordinate directions, N_r, N_θ, N_ϕ . The mesh points can be arbitrarily spaced when the derivatives are approximated using the finite difference method but are given by a specific distribution when the derivatives are approximated using the spectral collocation method. In the case of the spectral collocation method with Chebyshev basis functions for the radial direction and Fourier basis functions for the angular directions the collocation points are:

$$r_i = \frac{1}{2} - \frac{1}{2} \cos\left(\frac{i \pi}{N_r}\right) \quad (i = 1, 2, \dots, N_r) \quad (3.40)$$

$$\theta_j = \left(j - \frac{1}{2}\right) \left(\frac{\pi}{N_\theta}\right) \quad (j = 1, 2, \dots, N_\theta) \quad (3.41)$$

$$\phi_k = (k - 1) \left(\frac{2 \pi}{N_\phi}\right) \quad (k = 1, 2, \dots, N_\phi) \quad (3.42)$$

The Chebyshev points are scaled to the domain (0,1] for the unit sphere and the collocation point at the origin is not included. The derivatives are calculated by the matrix-vector multiplication:

$$D_k^n(i, j) * F(i) \quad (3.43)$$

for $k = r, \theta, \phi$, and $n = 1, 2$

Where, D is a differentiation matrix with coefficients that are dependent on the grid points used. The cross-derivatives are calculated by repeated matrix multiplications. The rows of the differentiation matrix for a 1-sided approximation with arbitrary spaced grid points can be generated using an algorithm for calculating the weights to be applied to each of the neighbouring points, Press et al (2007). The level of approximation can be adjusted by varying the number of neighbouring points used when calculating the weights. This algorithm is used for the second order finite difference pre-conditioner, with weights applied to the individual point and two nearest neighbours. It is also used to calculate the Chebyshev weights using all points given by (3.40).

The periodic differentiation matrices for the first and second derivatives with an even number of Fourier points are given by Trefethen (2000):

$$D_\theta(i, j) = D_\phi(i, j) = \begin{cases} 0 & n = \text{mod}(i - j, N) = 0 \\ \frac{1}{2} (-1)^n \cot\left(\frac{n \pi}{N}\right) & n = \text{mod}(i - j, N) \neq 0 \end{cases} \quad (3.44)$$

$$D_\theta^2(i, j) = D_\phi^2(i, j) = \begin{cases} -\frac{N^2}{12} - \frac{1}{6} & n = \text{mod}(i - j, N) = 0 \\ -\frac{1}{2} (-1)^n \frac{1}{\sin^2\left(\frac{n \pi}{N}\right)} & n = \text{mod}(i - j, N) \neq 0 \end{cases} \quad (3.45)$$

Where N is the number of grid points N_θ or N_ϕ and $\text{mod}(a, b)$ is the remainder after division of a by b .

The initial conditions consist of a combination of pressure, velocity, and surface shape. If the initial surface shape is the equilibrium shape (a sphere in the absence of external forces) then either an initial velocity or a pressure distribution at the surface are required for oscillations to occur.

Alternatively a non-equilibrium surface shape can be used with zero velocity as the initial condition, oscillations will then occur with the initial surface shape corresponding to an extent of the oscillation, i.e. maximum amplitude. The cases considered involve an initial surface shape with zero velocity. The pressure is calculated at the first time-step and in order to improve convergence of the Poisson equation, the pressure is initialised such that $P = \frac{2\Gamma}{R_0}$ for the interior points and $P = \Gamma K$ for the surface points.

The initial surface shape is defined by the equilibrium spherical droplet radius (R_0), and an amplitude for each of the spherical harmonic modes entered as combinations of mode number and amplitude (L , M , and $AMPL$ [s_L^M]). The initial surface shape is then generated by summing the spherical harmonic series with the given amplitude coefficients:

$$S(\theta, \phi, t = 0) = \sum_{L=0}^{L=\infty} \sum_{M=-L}^{M=L} s_L^M(t = 0) Y_L^M(\theta, \phi) \quad (3.46)$$

Where the spherical harmonics are given by:

$$Y_L^M(\theta, \phi) = N_L^M P_L^M(\cos \theta) \sqrt{2} \cos M\phi \quad (M > 0) \quad (3.47)$$

$$Y_L^M(\theta, \phi) = N_L^{|M|} P_L^{|M|}(\cos \theta) \sqrt{2} \sin|M|\phi \quad (M < 0) \quad (3.48)$$

$$Y_L^0(\theta, \phi) = N_L^0 P_L^0(\cos \theta) \quad (M = 0) \quad (3.49)$$

N_L^M is the normalisation constant used so that the spherical harmonics are orthonormal:

$$N_L^M = \sqrt{\frac{2L+1}{4\pi} \frac{(L-M)!}{(L+M)!}} \quad (3.50)$$

The associated Legendre functions are calculated using a combination of initial conditions and recurrence relations:

$$P_0^0 = 1 \quad (3.51)$$

$$P_1^0 = \cos \theta \quad (3.52)$$

$$P_1^1 = -\sin \theta \quad (3.53)$$

$$P_L^L = (-1)^L \frac{(2L)!}{2^L L!} \sin^L \theta \quad (L \geq 0) \quad (3.54)$$

$$P_L^M = \frac{(2L-1) \cos \theta P_{L-1}^M - (L+M-1) P_{L-2}^M}{L-M} \quad (L \geq 2) \quad (3.55)$$

$$P_L^M = -\frac{\sin \theta}{2M \cos \theta} [P_L^{M+1} + (L+M)(L-M+1)P_L^{M-1}] \quad (M \geq 1) \quad (3.56)$$

An arbitrary set of initial modes and amplitudes will in general fail to conserve the volume of a sphere with radius R_0 and so a volume correction term is introduced in the form of a uniform expansion or compression determined by adjusting the s_0^0 coefficient. The volume of the liquid droplet with surface shape defined by (3.9) is:

$$V = \frac{4}{3} \pi R_0^3 = \int_0^{2\pi} \int_0^\pi \frac{r_s^3}{3} \sin \theta \, d\theta \, d\phi \quad (3.57)$$

It is assumed that the volume is not conserved by the current surface shape and a new shape that conserves volume is calculated. Letting $x = 1 + \delta s_0^0$ the argument of the integral becomes:

$$r_s^3 = R_0^3 (x + S)^3 = R_0^3 (x^3 + 3x^2 S + 3x S^2 + S^3) \quad (3.58)$$

Due to the orthonormal properties of the spherical harmonic series (3.46) the volume integral can be simplified using the following integral results:

$$\int_0^{2\pi} \int_0^\pi Y_L^M \sin \theta \, d\theta \, d\phi = \begin{cases} \sqrt{4\pi} & \text{if } L = 0 \text{ and } M = 0 \\ 0 & \text{otherwise} \end{cases} \quad (3.59)$$

$$\int_0^{2\pi} \int_0^\pi Y_{L1}^{M1} Y_{L2}^{M2} \sin \theta \, d\theta \, d\phi = \begin{cases} 1 & \text{if } L1 = L2 \text{ and } M1 = M2 \\ 0 & \text{otherwise} \end{cases} \quad (3.60)$$

The final integral is calculated numerically using adaptive Simpson quadrature as described in the Matlab help documentation for the function ‘dblquad’ and results in the cubic equation:

$$4\pi = 4\pi x^3 + (3\sqrt{4\pi} s_0^0) x^2 + \left(3 \sum_{L=0}^{L=\infty} \sum_{M=-L}^{M=L} (s_L^M)^2 \right) x + \int_0^{2\pi} \int_0^\pi S^3 \sin \theta \, d\theta \, d\phi \quad (3.61)$$

This cubic equation is solved to find x , from which the volume adjustment δs_0^0 can be determined. The s_0^0 coefficient is then used to modify the surface shape. The volume correction requires the surface expansion series to be considered as a finite number of terms (L_{max}). The number of terms is chosen such that the contribution of any higher order modes is negligible.

3.6.3 Pre-Solve

The pre-solve step involves calculation of the variables that remain constant during the iterative solution step. As the change in surface position determined by the kinematic condition is uncoupled from the solution of the fluid flow equations the surface position is constant during the solve step. Therefore the pre-solve step consists of the calculation of a number of multipliers that are dependent on the surface shape in order to improve the efficiency of the iterative solution step (i.e. surface derivatives).

The flow variable equations are solved using the preconditioned bi-conjugate gradient stabilised method, with a second order finite different pre-conditioner. This requires a matrix representing each equation and their boundary conditions at the surface to be generated and inverted. The equations and boundary conditions are the same as the full solve except for the derivative weights. These matrices are only required to be calculated once per time-step. The matrix inversion is accomplished by LU Decomposition followed

by forward and backward substitution using the UMFPACK sparse matrix routines as described in the Matlab help documentation for the function ‘lu’.

3.6.4 Iterative Solution

Each of the four equations (3.3), (3.4), (3.5), (3.8) are solved iteratively using the preconditioned bi-conjugate gradient stabilised method for solving a linear set of equations ($A*x = b$), where A is a square matrix, this algorithm is given in Appendix B. This requires the equations to be rearranged so that all terms involving the other flow variables and also the non-linear terms are included in the vector b . This vector is constant for the given iteration k and so is calculated once before calling the iterative solver. Following the calculation of each of the fluid flow variables the derivatives are calculated using matrix vector multiplication as described in §3.6.2.

3.6.5 Post-Solve

The new surface position is determined by evaluation of the kinematic condition (3.27) using the new velocity components. The coefficients of a spherical harmonic series equivalent to the surface shape function (3.46) are determined using the linear least squares method. This requires a matrix (D) to be calculated, which consists of the spherical harmonics up to (L_{max}) evaluated at each grid point on the surface. The grid point is constant for each row and the spherical harmonic is constant for each column.

$$D(i, j) = Y_L^M(\theta_i, \phi_i) \quad (3.62)$$

The coefficients are then determined by solving the set of equations:

$$[D^T D](s_L^M) = [D^T](S) \quad (3.63)$$

The coefficients are output to file for further analysis. It is possible for a small mass (volume) conservation error to be introduced due to the decoupling of the kinematic condition from the fluid flow variable calculation and/or negligibly small contributions to

the surface shape that cannot be fully resolved due to the finite number of mesh points. In order to improve long term stability of the transient calculations the volume correction procedure described in §3.6.2 is applied to the new surface position.

The volume should then be conserved but there is an error introduced through the numerical integration of the volume correction algorithm. A consistency check on the volume correction method can be made by numerical integration of the volume integral (3.57) using the new surface shape. The numerical integral is calculated using the trapezoidal integration method with the surface shape interpolated to a grid with mesh density four times the given value. A spline method is used for the interpolation.

The final part of the post-solve step involves writing the results to output files. A selection of surface points and the calculated volume are output. The fluid flow variables for velocity and pressure are converted from the transformed coordinates to Cartesian coordinates for plotting.

3.6.6 Post-Simulation Analysis

The surface oscillations are analysed with the use of a number of different methods. Each method is applied to an input function, $F(i * DT)$ with $(i = 0, 1, 2, \dots, N)$, an evenly spaced function of time generated by the numerical code. The function is either the time dependent surface displacement of a point on the surface of the droplet or a time dependent surface coefficient (S_L^M) as given in equation (3.46).

The first method is the Fourier transform. The Fourier transform algorithm assumes the input function can be represented as a series expansion of trigonometric functions defined in complex form using Euler's formula:

$$F(t) = \sum_{n=0}^N a_n e^{i\omega_n t} \quad (3.64)$$

The Fourier transform is applied and the amplitude a_n and frequency ω_n of the oscillation modes making up the input function are returned. The basic Fourier transform is applied

without the use of any window functions as described in the Matlab help documentation for the function ‘fft’. The number of oscillation modes determined by the Fourier transform algorithm can be increased above the number of points making up the input function so that the amplitude and frequency can be determined to a higher level of accuracy.

The second method is the Logarithmic method described by Egry et al. (2005a), which can be used to determine the damping coefficient from the input function (assumed to consist of a single damped oscillation mode):

$$F(t) = f(t) e^{-\gamma t} \quad (3.65)$$

This is achieved by first squaring the input function, and then taking the natural logarithm:

$$\ln(F^2) = \ln(f^2) - 2\gamma t \quad (3.66)$$

The first and second derivatives are then obtained for the resulting function so that the peak values can be extracted by finding a change in sign in the first derivative (indicating a turning point), then checking the sign of the second derivative to establish whether the turning point is a maxima or minima. The peak values are then fitted to a straight line using the first and last peak values, which allows the value of the damping coefficient to be determined from the gradient (-2γ) of the line.

The final method is Prony’s method, which is described by Hauer et al. (1990). Prony’s method assumes the input function can be given as an expansion of complex damped sinusoids:

$$F(t) = \sum_{n=1}^N B_n e^{\lambda_n t} \quad (3.67)$$

Where $\lambda_n = \pm i \omega_n + \gamma_n$

The solution procedure consists of 3 steps, which are summarised below. The input function is truncated if necessary so that it consists of an even number of points ($2N$), $F(i)$ with ($i = 1, 2, \dots, 2N$).

Step 1:

The first step is to construct the matrix-vector system $A*p = b$ and then solve the system using direct matrix inversion to find p . The elements of the matrix A and vector b are just values of the input function:

$$A(i, j) = - \begin{bmatrix} F(N) & \dots & F(1) \\ \vdots & \ddots & \vdots \\ F(2N - 1) & \dots & F(N) \end{bmatrix} \quad (3.68)$$

$$b(i) = \begin{pmatrix} F(N) \\ \vdots \\ F(2N) \end{pmatrix}$$

The direct matrix inversion is achieved using the Moore-Penrose pseudo-inverse as described in the Matlab help documentation for the function 'pinv'.

Step 2:

The second step is to find the roots (e^{λ_n}) of the polynomial:

$$y = x^N + \sum_{n=1}^N P_n x^{n-1} \quad (3.69)$$

Where P_n are the polynomial coefficients obtained by solving the matrix-vector system in step 1. The roots of the polynomial y are found using the Matlab function for determining polynomial roots as described in the Matlab help documentation for the function 'roots'. The roots (e^{λ_n}) of the polynomial are used to give the Lambda values in the expansion of complex damped sinusoids:

$$\lambda_n = \ln(e^{\lambda_n})/DT \quad (3.70)$$

Step 3:

The third step is to construct another matrix-vector system $A*B = c$ and then solve the system using direct matrix inversion to find B . The elements of the matrix A are the polynomial roots obtained in step 2 raised to a power and the elements of the vector c are values of the input function:

$$A(i,j) = \begin{bmatrix} (e^{\lambda_1})^1 & \dots & (e^{\lambda_N})^1 \\ \vdots & \ddots & \vdots \\ (e^{\lambda_1})^N & \dots & (e^{\lambda_N})^N \end{bmatrix} \quad (3.71)$$

$$c(i) = \begin{pmatrix} F(1) \\ \vdots \\ F(N) \end{pmatrix}$$

The direct matrix inversion is carried out using Matlab as described in the Matlab help documentation for the backslash function ‘\’. The λ_n values determined in step 2 and the B_n values determined in step 3 now define the expansion of complex damped sinusoids given by (3.67), however we are interested in the real series of damped sinusoids:

$$F(t) = \sum_{n=0}^N A_n \cos(\omega_n t + \varphi_n) e^{-\gamma_n t} \quad (3.72)$$

Where A_n is the amplitude, ω_n the frequency, φ_n the phase, and γ_n the damping coefficient of the n th oscillation mode. This real series exists if the results obtained in steps 2 and 3 consist of pairs of complex exponentials, such that:

$$F(t) = \sum_{n=1}^N B_a e^{\lambda_a t} + B_b e^{\lambda_b t} = \sum_{n=0}^N A_n \cos(\omega_n t + \varphi_n) e^{-\gamma_n t} \quad (3.73)$$

Where the complex pairs are defined by:

$$\begin{aligned}
B_a &= \frac{1}{2} A_n e^{i\phi_n} \\
B_b &= \frac{1}{2} A_n e^{-i\phi_n} \\
\lambda_a &= \omega_n + \gamma_n \\
\lambda_b &= -\omega_n + \gamma_n
\end{aligned} \tag{3.74}$$

Therefore the results obtained are sorted and the matched terms established. It is possible that there are a number of unmatched terms, which indicates that the input function is not exactly approximated by a sum of real damped sinusoids. This does not mean that the results should be neglected as the terms identified can still provide valuable information. The accuracy of the terms identified can be checked by summing the series (3.72), with the values that have been determined and comparing it to the input function.

Once the terms have been matched the oscillation frequencies, damping coefficients, phases, and amplitudes can be determined through:

$$\begin{aligned}
\omega_n &= \text{Im}(\lambda_a) \\
\gamma_n &= \text{Re}(\lambda_a) \\
\varphi_n &= \text{angle}(B_a) = \text{Im}(\ln(B_a)) \\
A_n &= 2 \text{abs}(B_a) = 2 \sqrt{\text{Re}(B_a)^2 + \text{Im}(B_a)^2}
\end{aligned} \tag{3.75}$$

The results consist of a number of pure exponential terms equivalent to $\omega_n = 0$ and a number of damped oscillation terms. The solution procedure involved a direct matrix inversion and so not all values of the input function are used. The default is for every 10th point to be used (i.e. DT/10).

3.6.7 Default Settings

The numerical simulations in the following results sections use the default settings given in Table 3.1 unless specified.

Parameter	Parameter Description	Value
DT	Time-Step Increment	0.000250
NDT	Number of Time-Steps	4000
ITER_MAX1	Maximum Number of Iterations (Outer)	40
P_TOL1	L ² -Norm Tolerance for Pressure (Outer)	+1.00e-5
V_TOL1	L ² -Norm Tolerance for Velocity (Outer)	+1.00e-5
ITER_MAX2	Maximum Number of Iterations (BiCGStab)	5000
P_TOL2	L ² -Norm Tolerance for Poisson Equation	+1.00e-10
V_TOL2	L ² -Norm Tolerance for Momentum Equations	+1.00e-10
Table 3.1 – Numerical Model, Default Settings		

The default number of points are, $N_r = 16, N_\theta = 16, N_\phi = 32$. The density of the mesh can be seen in Figure 3.3, which shows the surface mesh, the y-z plane through the centre of the droplet (identical to the x-z plane due to symmetry), and the x-y plane also through the centre of the droplet. The line joining the poles in the y-z plane is added for plotting purposes only and the points on that line are not used in the numerical simulation.

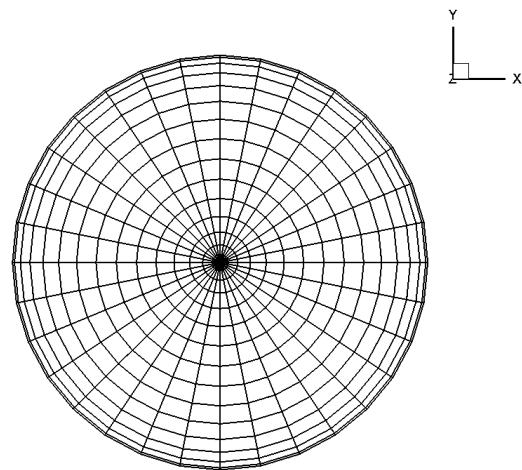
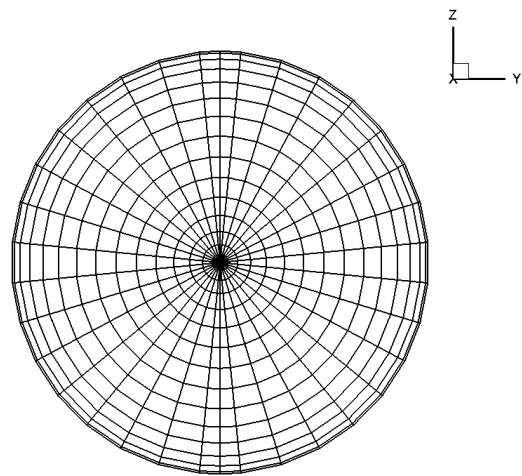
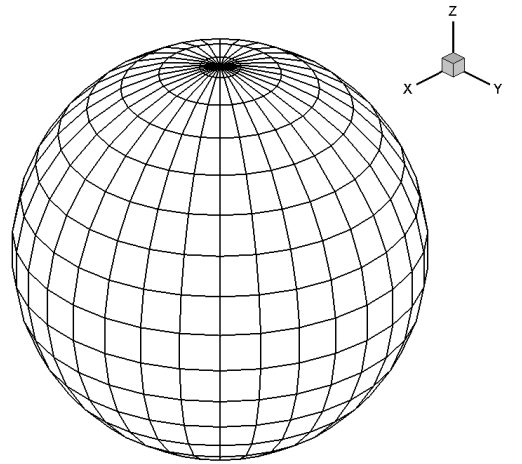


Figure 3.3 – Default Mesh

4. Droplet Oscillations in Free Space

4.1 Overview

In this section the numerical model outlined in section 3 will be used to investigate the dynamics of a droplet oscillating in free space with no external forces present. The main objective is to demonstrate the ability of the numerical model to simulate the different surface oscillation modes that occur due to surface tension forces in freely suspended droplets (i.e. where confinement forces are negligible, e.g. microgravity experiments).

Some aspects that will be considered are the normal mode frequencies and damping rates determined by Rayleigh (1879) and Lamb (1881, 1975). The frequency shift and mode coupling associated with high amplitude oscillations determined by Tsamopoulos and Brown (1983). The results are discussed in the context of application to the measurement of surface tension and viscosity

In §4.2 - §4.4 low amplitude oscillation of the three ($L = 2$) modes are considered in isolation with qualitative and quantitative comparisons of the velocity profile, frequency and damping rate of each mode made to the theoretical values.

The qualitative behaviour of the dynamics is independent of material. The material used for the simulations is water and the physical properties values used in the numerical model are:

Symbol	Quantity	Value	Units	Reference
Γ	Surface Tension Coefficient	+7.33e-2	N m ⁻¹	Hill and Eaves (2010)
ρ	Density	+9.99e+2	Kg m ⁻³	
ν	Kinematic Viscosity	+1.11e-6	m ² s ⁻¹	

Table 4.1 – Material Properties (Water)

The initial conditions for the numerical simulations in this section consist of a deformed surface shape and an internal velocity of zero ($\mathbf{V} = 0$). The surface shape is given by a

superposition of spherical harmonic surface shapes as described in section 3. In all numerical cases the unperturbed droplet radius is ($R_0 = 5.0$ mm). The general settings used in the numerical model are outlined in §3.6.7

4.2 Oscillation Mode: $L = 2, M = 0$

The first numerical test cases considered is for the axisymmetric Y_2^0 mode. The amplitude of the Y_2^0 mode corresponds to a maximum deformation of between 1% and 10% of the unperturbed droplet radius. Using the given description of the surface shape, the droplet cannot oscillate in this surface mode alone as it would violate mass conservation. In order to ensure that the initial condition conserves mass, an Y_0^0 mode coefficient is calculated and added to the dominant mode. The full initial condition is given by the superposition of these two spherical harmonic surface shapes:

$$r_s = R_0(1 + s_0^0 Y_0^0 + s_2^0 Y_2^0) \quad (4.1)$$

The spherical harmonics follow the definition given in section 3 and can be obtained using the recurrence relations used in the numerical model:

$$\begin{aligned} Y_0^0 &= N_0^0 \\ Y_2^0 &= N_2^0 \frac{1}{2}(3 \cos^2 \theta - 1) \end{aligned} \quad (4.2)$$

Taking into account the normalisation coefficients the surface shape coefficients for the initial condition are given in Table 4.2.

	$s_0^0 N_0^0$	$s_2^0 N_2^0$
Case 1	-2.00e-5	+1.00e-2
Case 2	-5.02e-4	+5.00e-2
Case 3	-2.02e-3	+1.00e-1
Table 4.2 – Initial Conditions, (Y_2^0)		

The time dependence of the surface shape coefficients s_L^M is assumed to be harmonic with exponential damping:

$$\cos(\omega_L^M t) \exp(-\gamma_L^M t) \quad (4.3)$$

The first approximation to the oscillation frequency and viscous damping coefficient for this oscillation mode are given by:

$$\omega_2^0 = \sqrt{\frac{8 \Gamma}{\rho R_0^3}} \quad (4.4)$$

$$\gamma_2^0 = 5 \frac{\nu}{R_0^2} \quad (4.5)$$

The oscillation of this mode is axisymmetric and so the surface shape and fluid flow profiles are the same for any plane parallel to the z-axis and passing through the centre of the droplet. The oscillation occurs about the unperturbed spherical shape as there is no static deformation, which only arises in the presence of external forces. Figure 4.1 shows plots of the flow variables in a plane parallel to the z-axis through the centre of the droplet at four points in the oscillation cycle for a droplet with the given initial condition. The results presented are for case 2, which has large enough amplitude to highlight the deformed surface shape and velocity profile. The solution is interpolated to evenly spaced grid points in the radial direction for plotting purposes.

Maximum deformation occurs when $\omega t = 0$ and $\omega t = \pi/2$, velocity is zero at these points in the cycle, kinetic energy = 0 and surface energy = maximum. Minimum deformation

(spherical droplet) occurs when $\omega t = \pi/4$ and $\omega t = 3\pi/4$, velocity is maximum at these points in the cycle, (kinetic energy = maximum and surface energy = minimum) with the hydrostatic reference pressure ($P = 2\Gamma/R_0$). This interchange between surface and kinetic energy with maximum and minima at these points in the oscillation cycle are a characteristic of all modes.

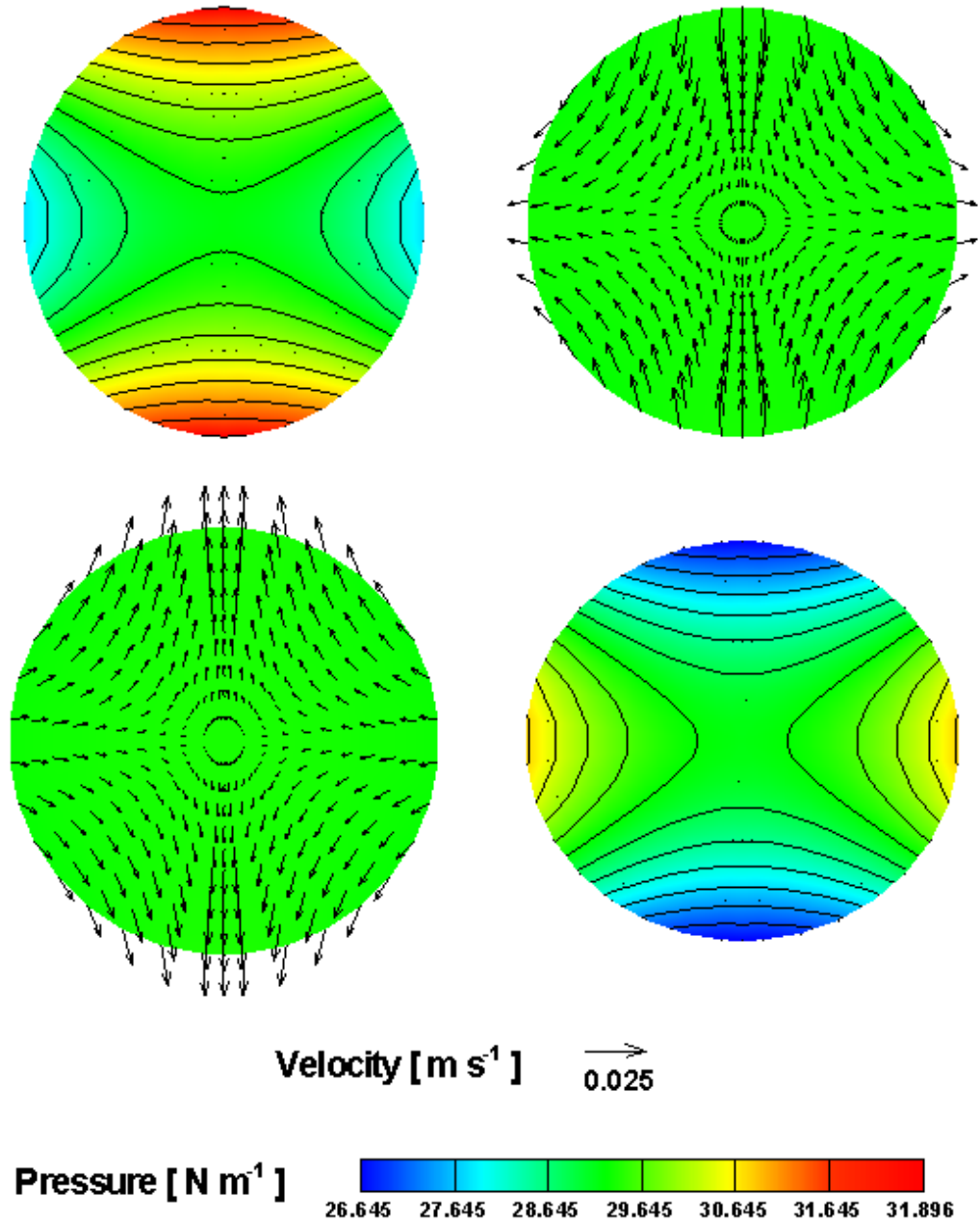


Figure 4.1 - Pressure Contour Lines and Velocity Vectors, (Y_2^0)

The flow is assumed to be laminar for the low amplitude oscillations considered in this study and so no turbulence model is used. The Reynolds number ($Re = \overline{|\mathbf{V}|} L/\nu$) is calculated at each time step and used to determine maximum value over the length of the simulation. The characteristic length scale used is the unperturbed spherical radius (R_0), the coefficient of viscosity is for water (given in Table 4.1), and the mean value of the velocity magnitude is taken from the numerical model at each time step. The maximum Reynolds number and the maximum of the velocity magnitude for simulations in the range of amplitudes considered are shown in Table 4.3, confirming that the flow is laminar in the cases considered.

	$ \mathbf{V} $ (max) [$m\ s^{-1}$]	Re (max)
Case 1	+3.41e-3	+6.29e+0
Case 2	+1.77e-2	+3.15e+1
Case 3	+3.67e-2	+6.31e+1

Table 4.3 – Velocity & Reynolds Number Maximum, (Y^0_2)

The displacement at the surface points of the droplet can be analysed using a Fourier transform as described in §3.6.6. Figure 4.2 shows the displacement of the surface point where the maximum deformation occurs ($\theta = 0, \phi = 0$) taken from the numerical simulation (case 1) and its Fourier transform. The theoretical value for the frequency is indicated in the power spectra with a dashed line.

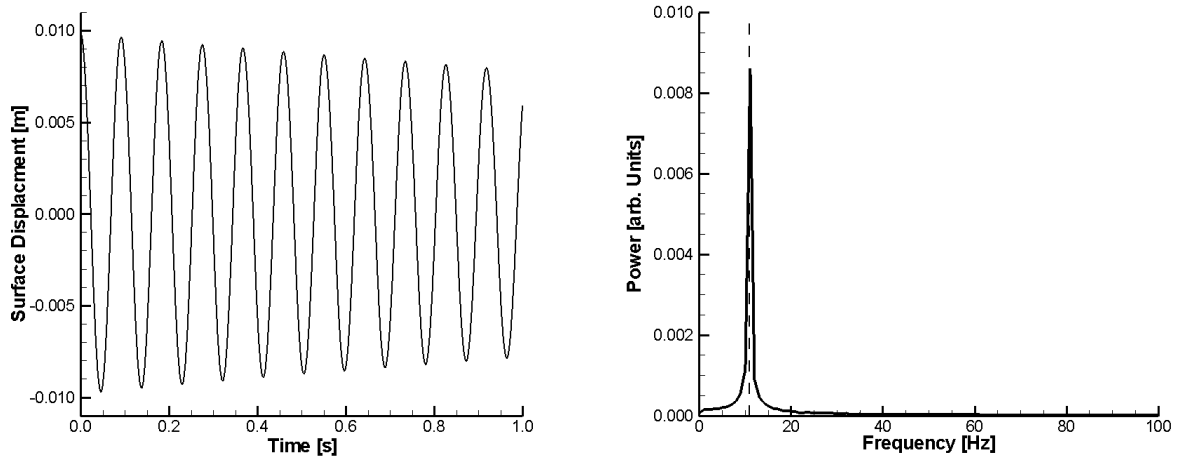


Figure 4.2 - Surface Displacement with Power Spectra, (Y_2^0)

The frequency and damping coefficient can be compared with the theoretical values determined using the Rayleigh and Lamb formulae, Table 4.4. The amplitude and frequency determined from the Fourier transform as well as the damping coefficient determined by applying the logarithmic method (described in §3.6.6) to the displacement function are given in Table 4.5. The Fourier transform results in a single peak with amplitude slightly lower than the initial condition due to viscous damping. The numerical frequency matches the theoretical value well, while the damping coefficient is slightly larger than the theoretical value.

Surface Mode	Amplitude [m]	Frequency [Hz]	Damping Coeff. [s^{-1}]
Y_2^0	+1.00e-2	+1.09e+1	+2.20e-1
Table 4.4 – Theoretical Results, (Y_2^0)			

Surface Mode	Amplitude [m]	Frequency [Hz]	Damping Coeff. [s^{-1}]
Y_2^0	+8.74e-3	+1.09e+1	+2.28e-1
Table 4.5 – Numerical Results, (Y_2^0)			

4.2.1 Nonlinear Terms

The power spectra of the surface point is dominated by the relatively large amplitude Y_2^0 mode, however theoretical considerations tell us that there should be additional small amplitude components that are present due to the nonlinear terms in the momentum equations. It is possible to analyse these components by separating the surface shape function into its spherical harmonic components and treating each of the modes individually.

The second order correction for the Y_2^0 mode determined by the inviscid analysis of Tsamopoulos and Brown (1983) suggests the existence of additional Y_0^0 , Y_2^0 , and Y_4^0 components that are proportional to the square of the amplitude but with twice the frequency:

$$r_s = R_0 \left[1 + s_2^0 \cos(\omega_2^0 t) Y_2^0 + \frac{(s_2^0)^2}{2} \left\{ -\frac{1}{5} [1 + \cos(2\omega_2^0 t)] Y_0^0 + \frac{11}{14} \left[1 - \frac{29}{33} \cos(2\omega_2^0 t) \right] Y_2^0 + \frac{18}{35} \left[1 + \frac{3}{5} \cos(2\omega_2^0 t) \right] Y_4^0 \right\} \right] \quad (4.6)$$

The numerical cases include the effects of viscosity, for which there is no theoretical formulae for the higher order corrections. However information can be obtained by comparing the amplitude, frequency, and damping coefficient of each component with the theoretical results that are available.

This analysis is performed using Prony's method (described in §3.6.6) for case 1. The numerical analysis reveals that the surface oscillation is dominated by the Y_2^0 mode with small components of the Y_0^0 and Y_4^0 modes. These coefficients and the power spectra of the oscillating terms obtained using Prony's method are shown in Figure 4.3. Integer multiples of the theoretical value for the frequency are indicated in the power spectra with dashed lines.

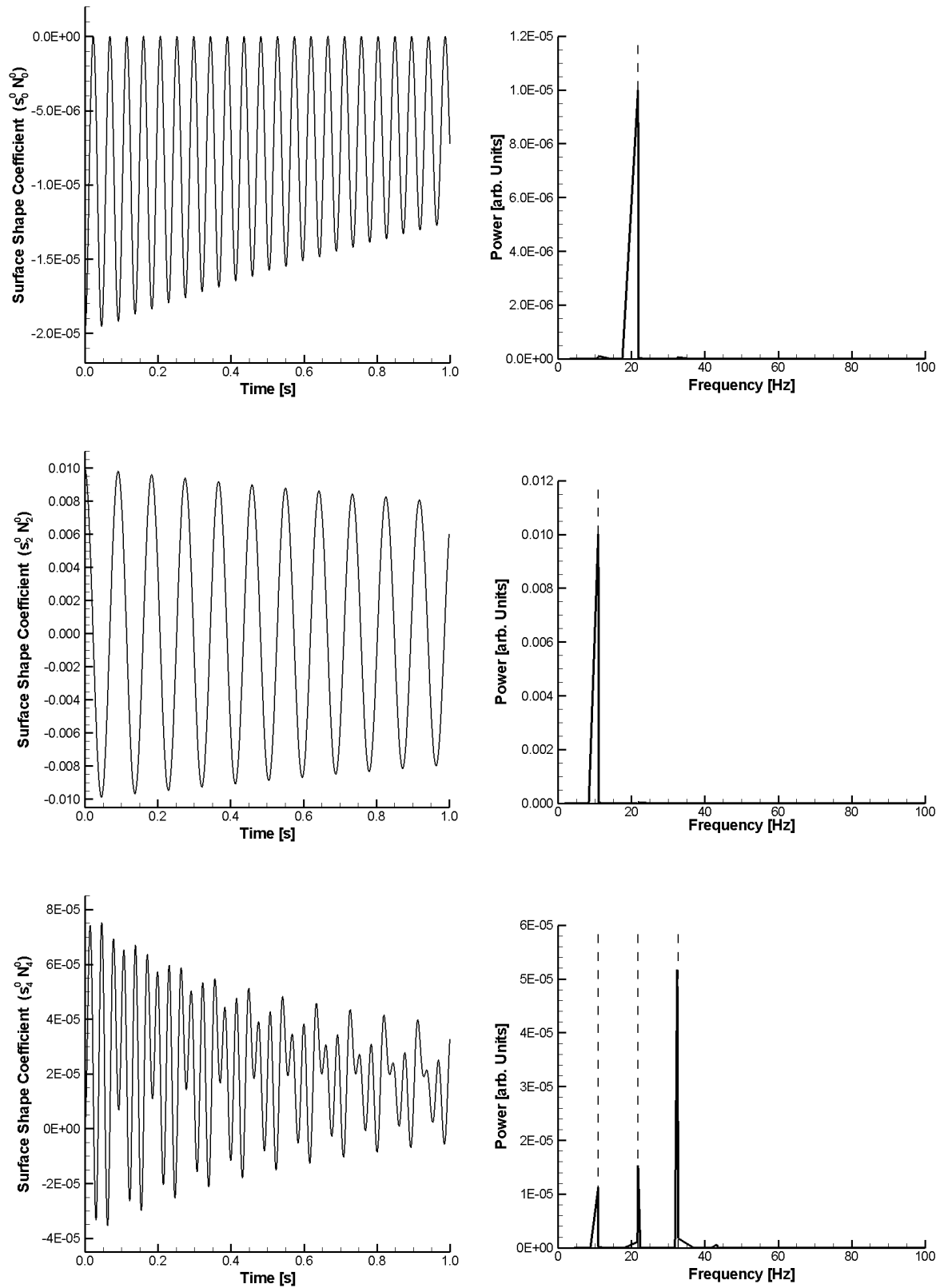


Figure 4.3 - Surface Shape Coefficients with Power Spectra, (Y_2^0)

The theoretical results are shown in Table 4.6 and the numerical results determined using Prony's method are shown in Table 4.7. The constant terms in (4.6) are displayed as rows in the tables with zero frequency and the damping coefficient is shown as undetermined because the analysis of Tsamopoulos and Brown did not include viscosity.

Surface Mode	Amplitude [m]	Frequency [Hz]	Damping Coeff. [s ⁻¹]
Y_0^0	-1.00e-5	+0.00e+0	Undetermined
	-1.00e-5	+2.18e+1	Undetermined
Y_2^0	+1.00e-2	+1.09e+1	+2.20e-1
	+3.93e-5	+0.00e+0	Undetermined
	-3.45e-5	+2.18e+1	Undetermined
Y_4^0	+2.57e-5	+0.00e+0	Undetermined
	-1.54e-5	+2.18e+1	Undetermined
Table 4.6 – Theoretical Results, (Y_2^0)			

Surface Mode	Amplitude [m]	Frequency [Hz]	Damping Coeff. [s ⁻¹]
Y_0^0	-9.99e-6	+0.00e+0	+4.65e-1
	-9.99e-6	+2.18e+1	+4.66e-1
Y_2^0	+1.00e-2	+1.09e+1	+2.33e-1
	+3.89e-5	+0.00e+0	+4.63e-1
	-3.48e-5	+2.18e+1	+4.67e-1
Y_4^0	-5.17e-5	+3.25e+1	+1.72e+0
	+2.58e-5	+0.00e+0	+4.66e-1
	+1.53e-5	+2.18e+1	+4.65e-1
	+1.12e-5	+1.09e+1	+2.37e-1
Table 4.7 – Numerical Results, (Y_2^0)			

Comparing the results in Tables 4.6 and 4.7, it can be seen that there is good agreement with the amplitude and frequency for each of the additional second order components. The

second order theoretical analysis was only conducted for inviscid droplets, whereas the numerical simulation includes viscosity. The results from the numerical simulation show that the second order components with twice the Rayleigh frequency also have a damping rate that is twice the Lamb damping rate.

The numerical results also reveal two additional components of the Y_4^0 mode. The frequency of the larger component is equal to the frequency of the Y_4^0 mode and also three times the frequency of the Y_2^0 mode and so it is not clear which normal mode it is part of. The damping coefficient of this component is not consistent with either the Y_4^0 mode or three times the damping of the Y_2^0 mode. The frequency of the smaller component is equal to the frequency of the Y_2^0 mode and the damping coefficient is also close to the Y_2^0 mode value.

4.2.2 High Amplitude Effects

The theoretical analysis of Tsamopoulos and Brown (1983) also indicated that the frequency of oscillation decreases as the amplitude increases:

$$\omega_2^0 = \sqrt{\frac{8 \Gamma}{\rho R_0^3} \left(1 - \frac{(S_2^0)^2}{2} \frac{37559}{29400} \right)} \quad (4.7)$$

It is possible to make a quantitative comparison between the theoretical result and the numerical results obtained from a Fourier transform of the surface point where the maximum deformation occurs. Figure 4.4 shows the theoretical and numerical values for the frequency with amplitudes up to 10% of the unperturbed droplet radius. The frequency decrease is small in this case and the accuracy is limited by the Fourier transform, however there is good qualitative agreement between the theoretical and numerical results.

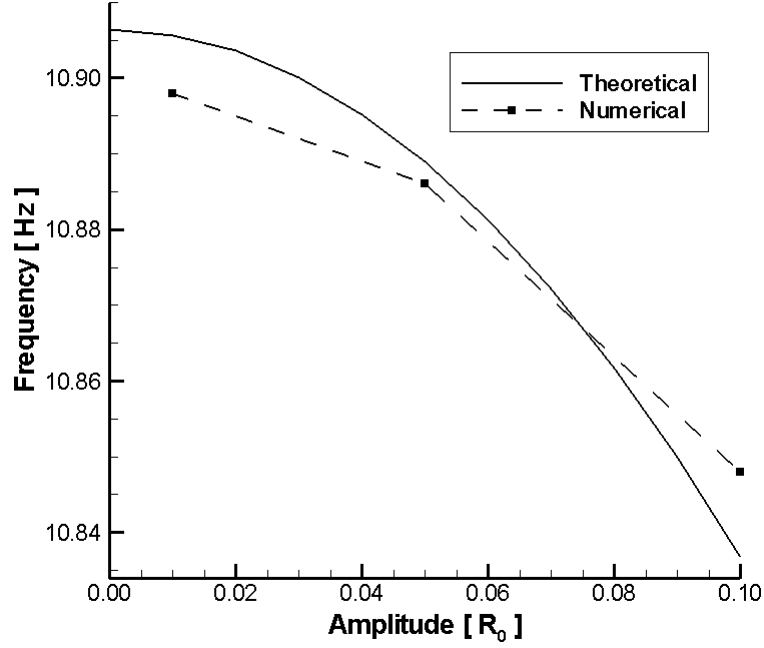


Figure 4.4 - Frequency as a function of amplitude, (Y_2^0)

4.3 Oscillation Mode: $L = 2, M = 1$

The next numerical test cases considered are for the non-axisymmetric Y_2^1 mode. The amplitude of the Y_2^1 mode corresponds to a maximum deformation of between 1% and 10% of the unperturbed droplet radius. As in the previous cases the Y_0^0 mode coefficient is calculated and added to the initial condition to ensure mass conservation, the full initial condition is given by the superposition of these two spherical harmonic surface shapes:

$$r_s = R_0(1 + s_0^0 Y_0^0 + s_2^1 Y_2^1) \quad (4.8)$$

The spherical harmonics follow the definition given in section 3 and can be obtained using the recurrence relations used in the numerical model:

$$\begin{aligned} Y_0^0 &= N_0^0 \\ Y_2^1 &= -N_2^1 \sqrt{2} (3 \sin \theta \cos \theta) \cos \phi \end{aligned} \quad (4.9)$$

The maximum value of the associated Legendre component of the Y_2^l spherical harmonic is $3/2$ and so the amplitude coefficients are multiplied by $2/3$ to give a similar level of deformation as the Y_2^0 mode test cases. Taking into account the normalisation coefficients the surface shape coefficients for the initial condition are:

	$s_0^0 N_0^0$	$s_2^1 N_2^1 \sqrt{2}$
Case 1	-2.67e-5	+6.67e-3
Case 2	-6.67e-4	+3.33e-2
Case 3	-2.67e-3	+6.67e-2
Table 4.8 – Initial Conditions, (Y_2^l)		

The theoretical values for the oscillation frequency and viscous damping coefficient are the same as Y_2^0 mode test cases because the formulae are independent of the azimuthal number.

The oscillation of this mode is non-axisymmetric, and fluid flow only occurs in the x-z planes. The surface shape and fluid flow profiles are the same for any x-z plane with magnitude depending on distance from the centre of the droplet. The oscillation occurs about the unperturbed spherical shape as there is no static deformation, which only arises in the presence of external forces. Figure 4.5 shows plots of the flow variables in the x-z plane in the centre of the droplet at four points in the oscillation cycle for a droplet with the given initial condition. The results presented are for case 2, which has large enough amplitude to highlight the deformed surface shape and velocity profile.

Maximum deformation occurs when $\omega t = 0$ and $\omega t = \pi/2$, velocity is zero at these points in the cycle, kinetic energy = 0 and surface energy = maximum. Minimum deformation (spherical droplet) occurs when $\omega t = \pi/4$ and $\omega t = 3\pi/4$, velocity is maximum at these points in the cycle, (kinetic energy = maximum and surface energy = minimum) with the hydrostatic reference pressure ($P = 2\Gamma/R_0$). This interchange between surface and kinetic energy with maximum and minima at these points in the oscillation cycle are a characteristic of all modes.

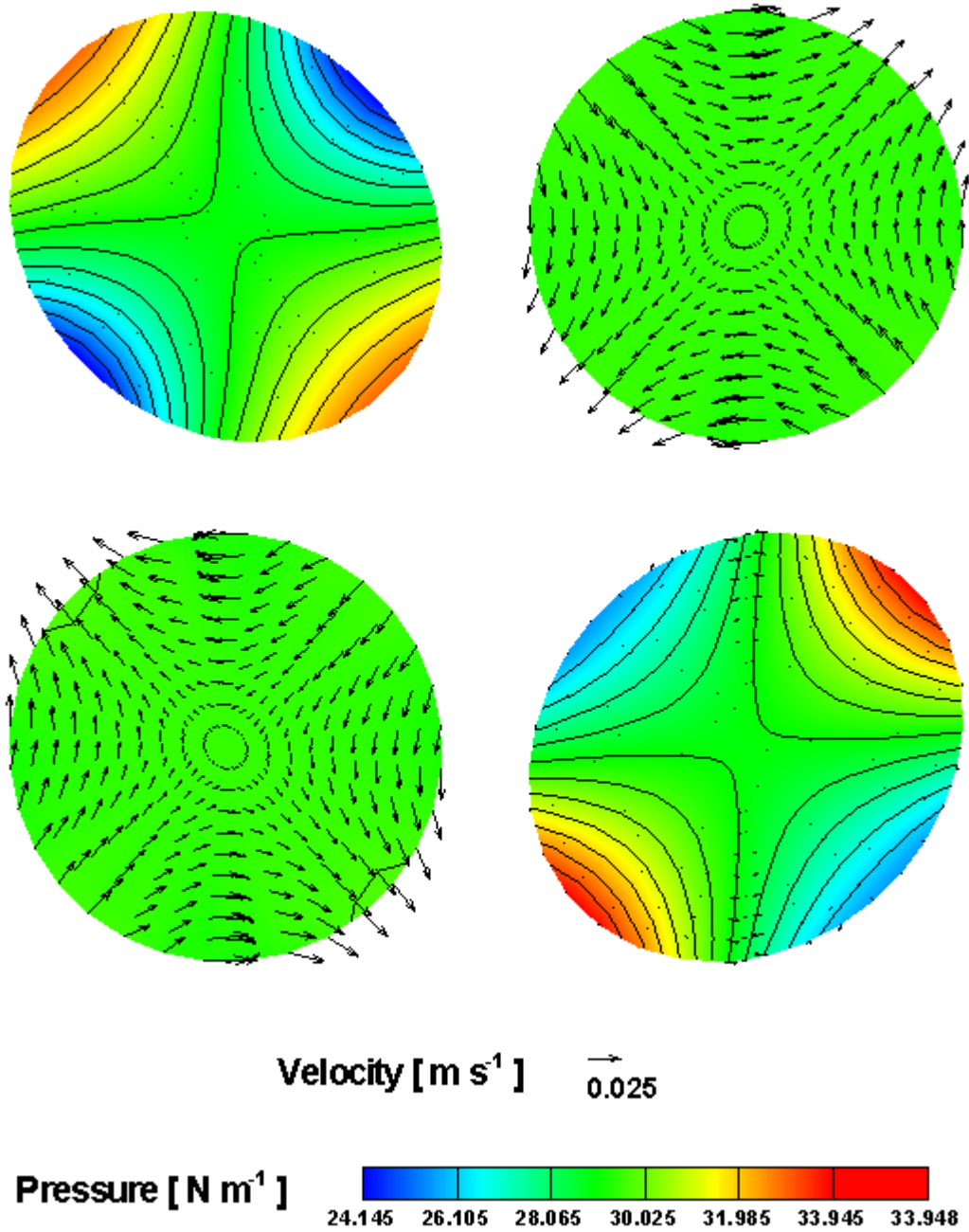


Figure 4.5 - Pressure Contour Lines and Velocity Vectors, (Y^l_2)

The flow is assumed to be laminar for the low amplitude oscillations considered in this study and so no turbulence model is used. The Reynolds number ($Re = |\bar{V}| L/\nu$) is calculated at each time step and used to determine maximum value over the length of the simulation. The characteristic length scale used is the unperturbed spherical radius (R_0), the

coefficient of viscosity is for water (given in Table 4.1), and the mean value of the velocity magnitude is taken from the numerical model at each time step. The maximum Reynolds number and the maximum of the velocity magnitude for simulations in the range of amplitudes considered are shown in Table 4.9, confirming that the flow is laminar in the cases considered.

	$ \mathbf{V} $ (max) [m s ⁻¹]	Re (max)
Case 1	+3.74e-3	+6.89e+0
Case 2	+2.36e-2	+3.45e+1
Case 3	+5.12e-2	+6.96e+1

Table 4.9 – Velocity & Reynolds Number Maximum, (Y^l_2)

The displacement at the surface points of the droplet can be analysed using a Fourier transform as described in §3.6.6. Figure 4.6 shows the displacement of the surface point where the maximum deformation occurs ($\theta = \pi/4, \phi = 0$), taken from the numerical simulation (case 1) and its Fourier transform.

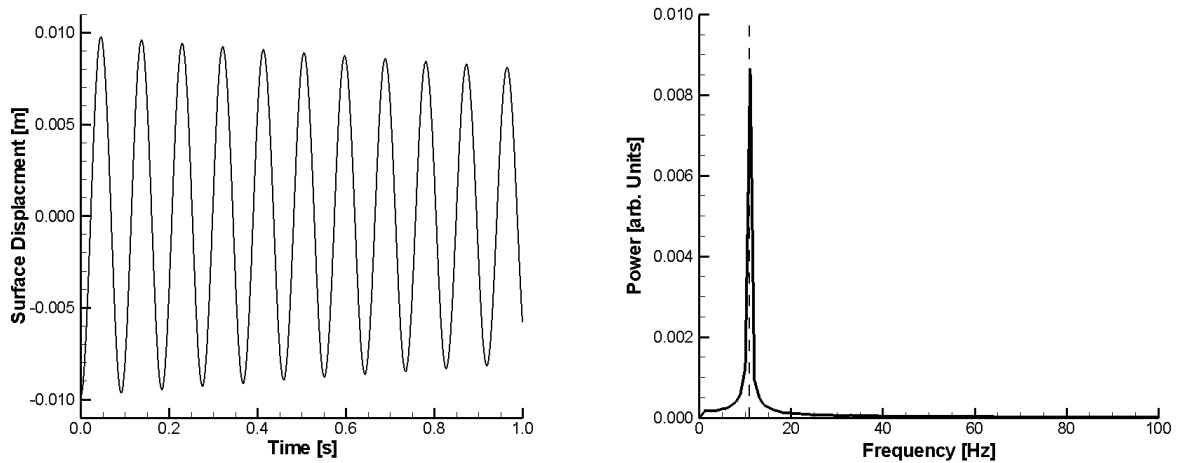


Figure 4.6 - Surface Displacement with Power Spectra, (Y^l_2)

The frequency and damping coefficient can be compared with the theoretical values determined using the Rayleigh and Lamb formulae that are the same for all ($L = 2$) modes, Table 4.10. The amplitude and frequency determined from the Fourier transform as well as

the damping coefficient determined by applying the logarithmic method (described in §3.6.6) to the displacement function are given in Table 4.11. The Fourier transform results in a single peak with amplitude slightly lower than the initial condition due to viscous damping. The numerical and theoretical values are in good agreement.

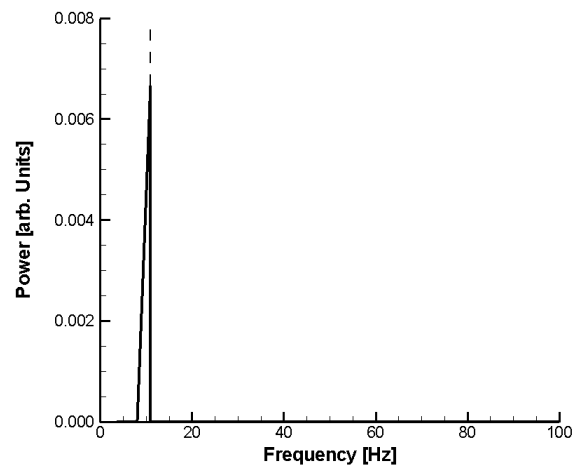
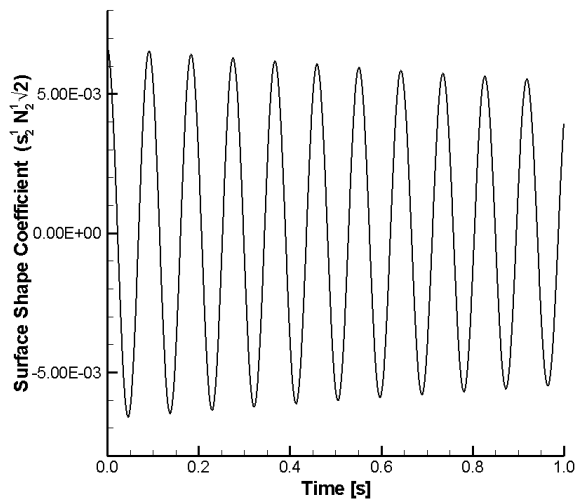
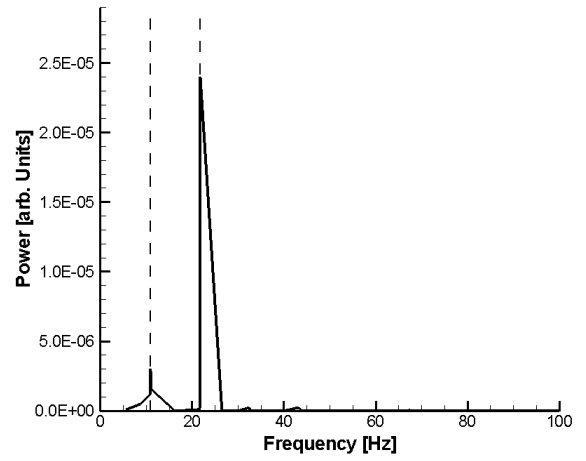
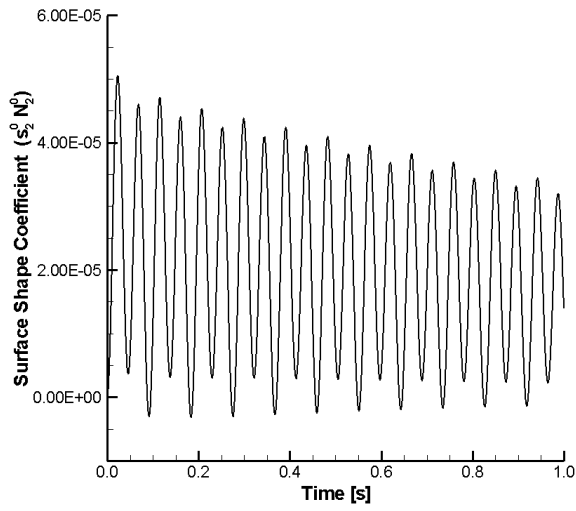
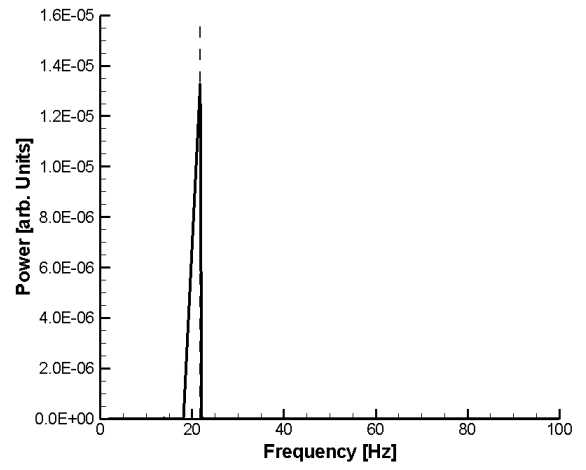
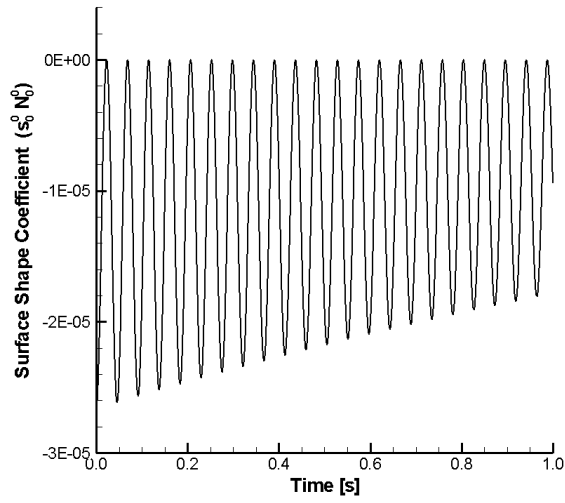
Surface Mode	Amplitude [m]	Frequency [Hz]	Damping Coeff. [s ⁻¹]
Y_2^l	+1.00e-2	+1.09e+1	+2.20e-1
Table 4.10 – Theoretical Results, (Y_2^l)			

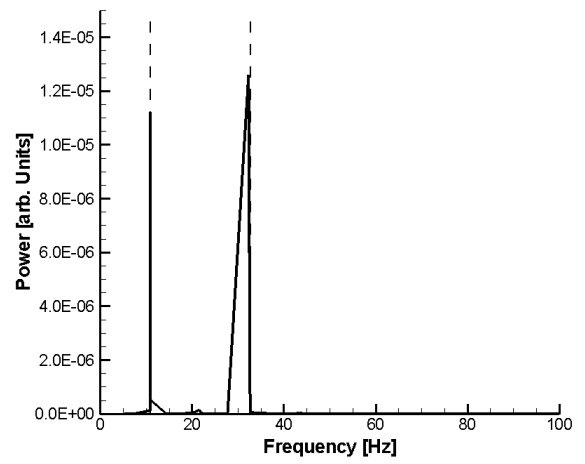
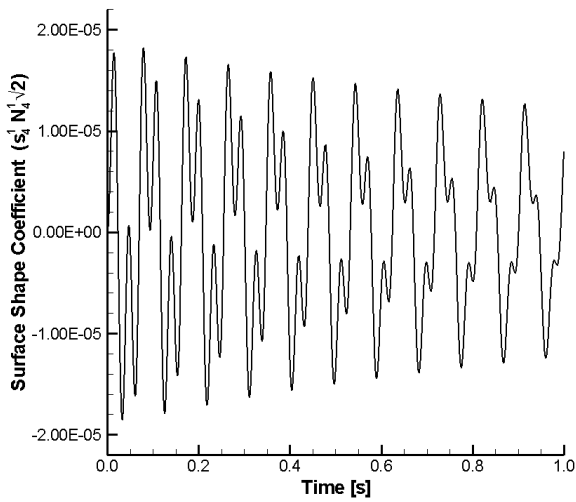
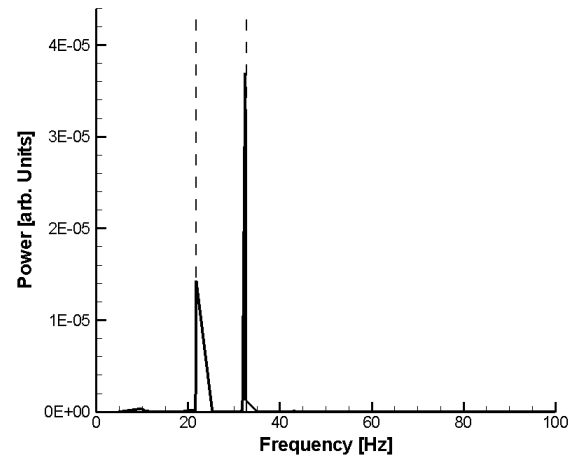
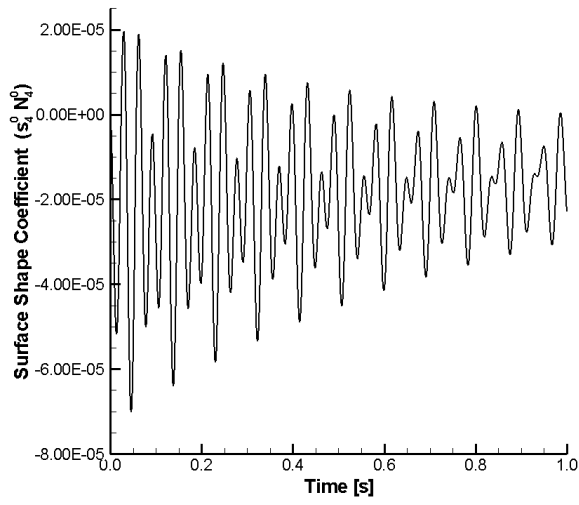
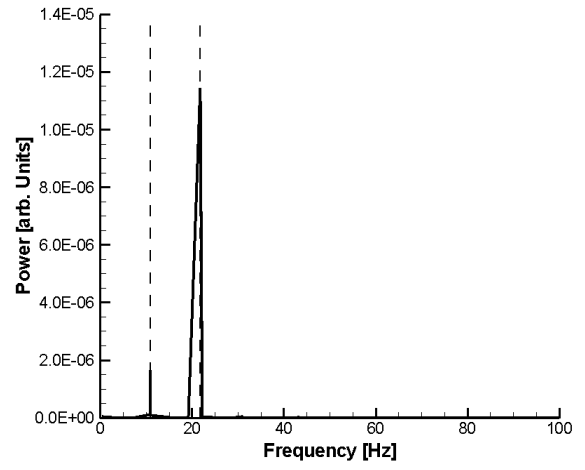
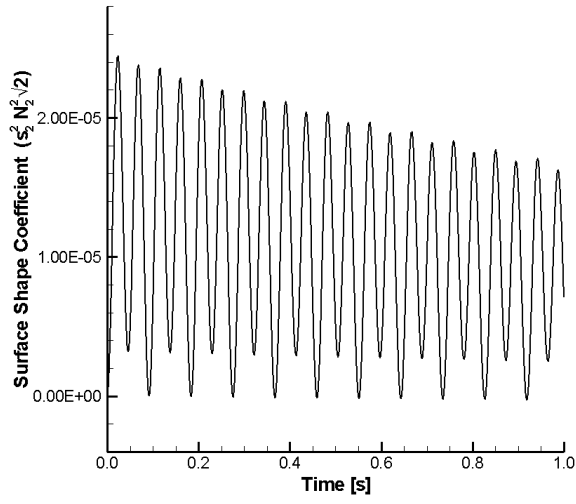
Surface Mode	Amplitude [m]	Frequency [Hz]	Damping Coeff. [s ⁻¹]
Y_2^l	+8.84e-3	+1.09e+1	+2.02e-1
Table 4.11 – Numerical Results, (Y_2^l)			

4.3.1 Nonlinear Terms

The power spectra of the surface point is dominated by the relatively large amplitude Y_2^l mode, however theoretical considerations tell us that there should be additional small amplitude components that are present due to the nonlinear terms in the momentum equations. It is possible to analyse these components by separating the surface shape function into its spherical harmonic components and treating each of the modes individually.

This analysis is performed using Prony’s method (described in §3.6.6) for numerical test case 1. The numerical analysis revealed that the surface oscillation is dominated by the Y_2^l mode with small amplitude components of various other modes with frequency multiples of the normal mode frequency. The most dominant terms after the Y_2^l mode are the Y_0^0 , Y_2^0 , Y_2^2 , Y_4^0 , Y_4^l , and Y_4^2 modes. These coefficients and their power spectra obtained using Prony’s method are shown in Figure 4.7.





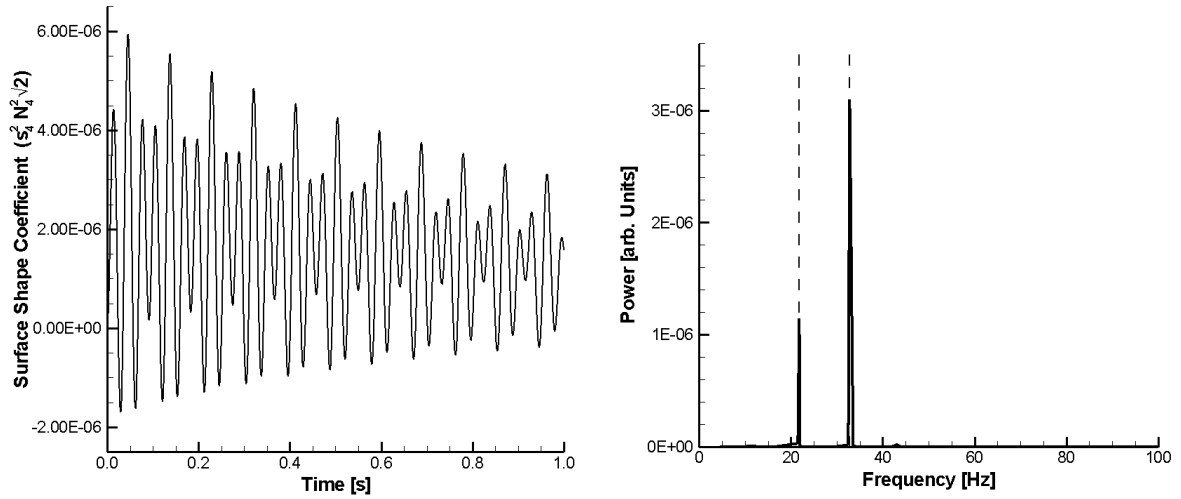


Figure 4.7 - Surface Shape Coefficients with Power Spectra, (Y_2^l)

The second order correction for the Y_2^l mode has not been established but the axisymmetric inviscid analysis of Tsamopoulos and Brown (1983) suggests the existence of additional components that are proportional to the square of the amplitude but with twice the frequency. The analysis performed for the Y_2^o mode showed good agreement with the theoretical calculations and so the same analysis is performed for the Y_2^l mode in order to determine the higher order corrections. The results of the analysis using Prony's method for the four most dominant modes are summarised in Table 4.12.

Surface Mode	Amplitude [m]	Frequency [Hz]	Damping Coeff. [s ⁻¹]
Y^0_0	+1.33e-5	+0.00e+0	+4.01e-1
	+1.33e-5	+2.18e+1	+4.01e-1
Y^0_2	-2.49e-5	+0.00e+0	+3.90e-1
	-2.40e-5	+2.18e+1	+4.01e-1
Y^l_2	+6.66e-3	+1.09e+1	+2.01e-1
Y^2_2	-1.31e-5	+0.00e+0	+4.02e-1
	+1.14e-5	+2.18e+1	+4.02e-1
Y^0_4	+1.43e-5	+2.18e+1	+3.95e-1
	+2.31e-5	+0.00e+0	+4.03e-1
	-3.70e-5	+3.25e+1	+1.72e+0
Y^l_4	-1.26e-5	+3.23e+1	+1.45e+0
	+1.12e-5	+1.09e+1	+1.99e-1
Y^2_4	+1.15e-5	+2.18e+1	+3.98e-1
	-1.92e-6	+0.00e+0	+4.02e-1
	+3.10e-6	+3.27e+1	+1.11e+0
Table 4.12 – Numerical Results, (Y^l_2)			

The results show that the amplitude of the Y^0_0 mode is half the input amplitude. The frequencies are multiples of those given by the Rayleigh formula. However the damping rate of the dominant mode is lower than that given by the Lamb formula. The damping rates of the higher order components are approximately twice the damping rate of the numerical value for the main mode. There is a Y^0_4 mode component, which has the same frequency and damping rate as the component found in the analysis of the Y^0_2 case.

4.4 Oscillation Mode: $L = 2, M = 2$

The next numerical test cases considered are for the non-axisymmetric Y_2^2 mode. The amplitude of the Y_2^2 mode corresponds to a maximum deformation of between 1% and 10% of the unperturbed droplet radius. As in the previous cases the Y_0^0 mode coefficient is calculated and added to the initial condition to ensure mass conservation, the full initial condition is given by the superposition of these two spherical harmonic surface shapes:

$$r_s = R_0(1 + s_0^0 Y_0^0 + s_2^2 Y_2^2) \quad (4.10)$$

The spherical harmonics follow the definition given in section 3 and can be obtained using the recurrence relations used in the numerical model:

$$Y_0^0 = N_0^0 \quad (4.11)$$

$$Y_2^2 = N_2^2 \sqrt{2} (3 \sin^2 \theta) \cos 2\phi$$

The maximum value of the associated Legendre component of the Y_2^2 spherical harmonic is 3 and so the amplitude coefficients are multiplied by 1/3 to give a similar level of deformation as the Y_2^0 and Y_2^1 mode test cases. Taking into account the normalisation coefficients the surface shape coefficients for the initial condition are:

	$s_0^0 N_0^0$	$s_2^2 N_2^2 \sqrt{2}$
Case 1	-2.67e-5	+3.33e-3
Case 2	-6.67e-4	+1.67e-2
Case 3	-2.67e-3	+3.33e-2
Table 4.13 – Initial Conditions, (Y_2^2)		

The theoretical values for the oscillation frequency and viscous damping coefficient are the same as Y_2^0 and Y_2^1 mode test cases because the formulae are independent of the azimuthal number.

The oscillation of this mode is non-axisymmetric, and fluid flow only occurs in the x-y planes. The surface shape and fluid flow profiles are the same for any x-y plane with magnitude depending on distance from the centre of the droplet. The oscillation occurs about the unperturbed spherical shape as there is no static deformation, which only arises in the presence of external forces. Figure 4.8 shows plots of the flow variables in the x-y plane in the centre of the droplet at four points in the oscillation cycle for a droplet with the given initial condition. The results presented are for case 2, which has large enough amplitude to highlight the deformed surface shape and velocity profile.

Maximum deformation occurs when $\omega t = 0$ and $\omega t = \pi/2$, velocity is zero at these points in the cycle, kinetic energy = 0 and surface energy = maximum. Minimum deformation (spherical droplet) occurs when $\omega t = \pi/4$ and $\omega t = 3\pi/4$, velocity is maximum at these points in the cycle, (kinetic energy = maximum and surface energy = minimum) with the hydrostatic reference pressure ($P = 2\Gamma/R_0$). This interchange between surface and kinetic energy with maximum and minima at these points in the oscillation cycle are a characteristic of all modes.

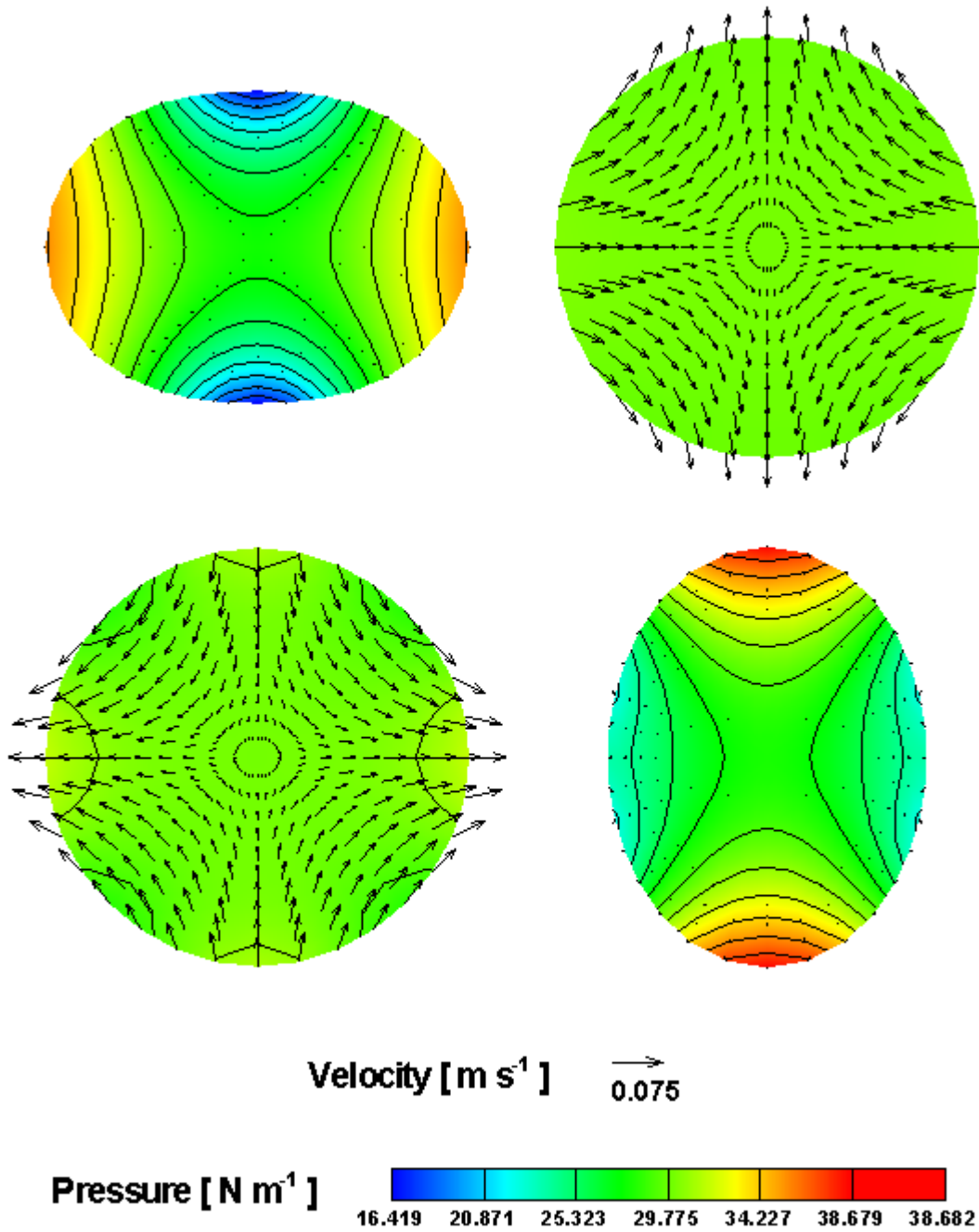


Figure 4.8 - Pressure Contour Lines and Velocity Vectors, (Y^2_2)

The flow is assumed to be laminar for the low amplitude oscillations considered in this study and so no turbulence model is used. The Reynolds number ($Re = \overline{|\mathbf{V}|} L/\nu$) is calculated at each time step and used to determine maximum value over the length of the simulation. The characteristic length scale used is the unperturbed spherical radius (R_0), the

coefficient of viscosity is for water (given in Table 4.1), and the mean value of the velocity magnitude at each time step taken from the numerical model. The maximum Reynolds number and the maximum of the velocity magnitude for simulations in the range of amplitudes considered are shown in Table 4.14, confirming that the flow is laminar in the cases considered.

	$ \mathbf{V} $ (max) [m s ⁻¹]	Re (max)
Case 1	+3.43e-3	+5.18e+0
Case 2	+1.79e-2	+2.58e+1
Case 3	+3.72e-2	+5.11e+1

Table 4.14 – Velocity & Reynolds Number Maximum, (Y_2^2)

The displacement at the surface points of the droplet can be analysed using a Fourier transform as described in §3.6.6. Figure 4.9 shows the displacement of the surface point where the maximum deformation occurs ($\theta = \pi/2, \phi = 0$), taken from the numerical simulation (case 1) and its Fourier transform.

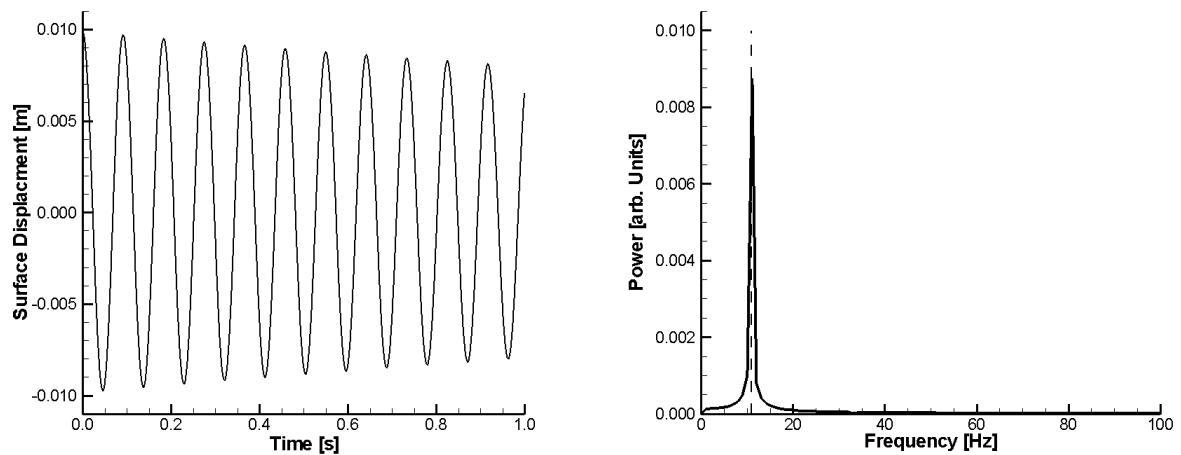


Figure 4.9 - Surface Displacement with Power Spectra, (Y_2^2)

The frequency and damping coefficient can be compared with the theoretical values determined using the Rayleigh and Lamb formulae that are the same for all ($L = 2$) modes, Table 4.15. The amplitude and frequency determined from the Fourier transform as well as the damping coefficient determined by applying the logarithmic method (described in

§3.6.6) to the displacement function are given in Table 4.16. The Fourier transform results in a single peak with amplitude slightly lower than the initial condition due to viscous damping. The numerical and theoretical values show good agreement.

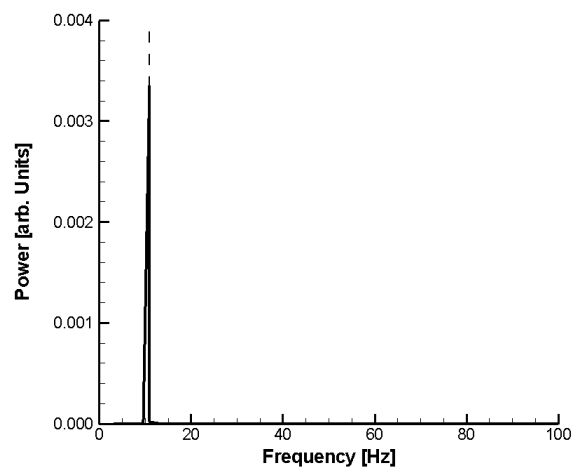
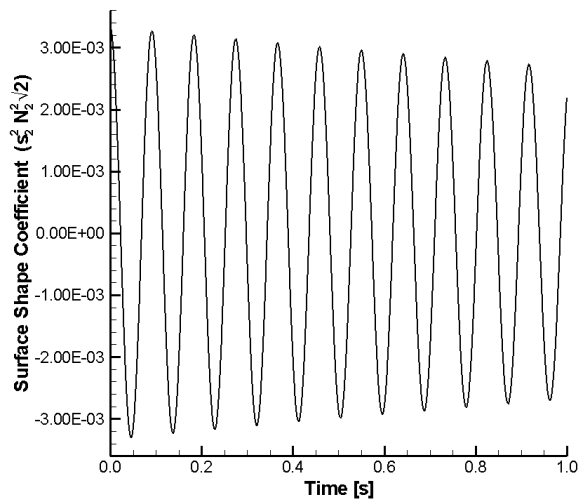
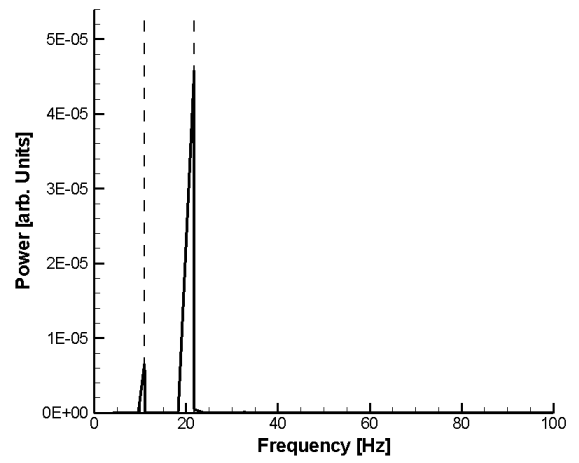
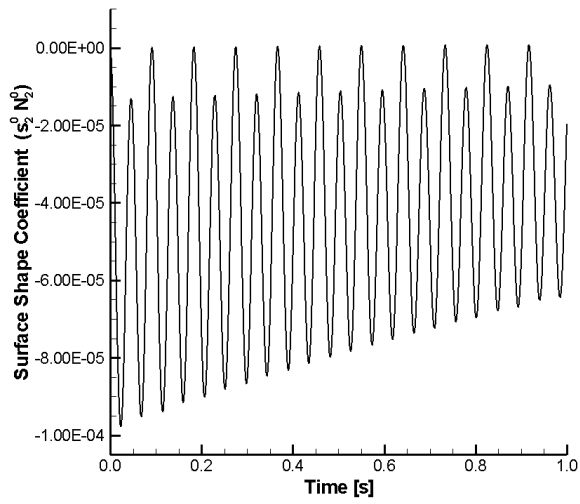
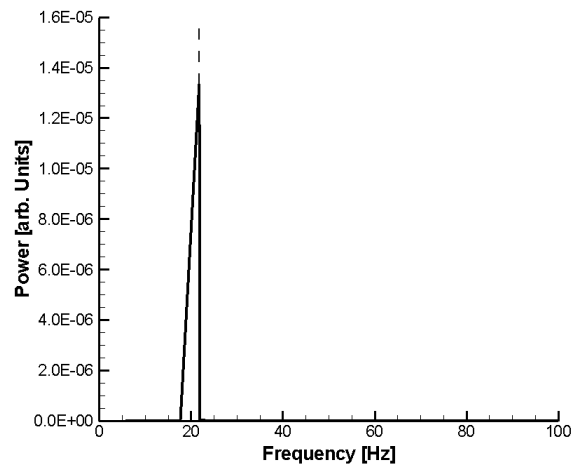
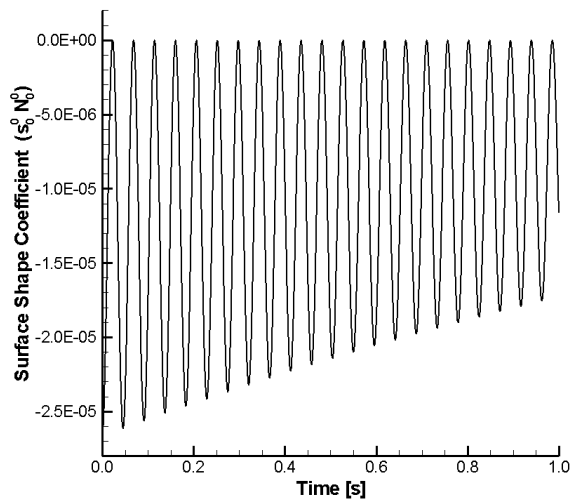
Surface Mode	Amplitude [m]	Frequency [Hz]	Damping Coeff. [s ⁻¹]
Y_2^2	+1.00e-2	+1.09e+1	+2.20e-1
Table 4.15 – Theoretical Results, (Y_2^2)			

Surface Mode	Amplitude [m]	Frequency [Hz]	Damping Coeff. [s ⁻¹]
Y_2^2	+8.85e-3	+1.09e+1	+2.14e-1
Table 4.16 – Numerical Results, (Y_2^2)			

4.4.1 Nonlinear Terms

The power spectra of the surface point is dominated by the relatively large amplitude Y_2^2 mode, however theoretical considerations tell us that there should be additional small amplitude components that are present due to the nonlinear terms in the momentum equations. It is possible to analyse these components by separating the surface shape function into its spherical harmonic components and treating each of the modes individually.

This analysis is performed using Prony’s method (described in §3.6.6) for numerical test case 1. The numerical analysis revealed that the surface oscillation is dominated by the Y_2^2 mode with small amplitude components of various other modes with frequency multiples of the normal mode frequency. The most dominant terms after the Y_2^2 mode are the Y_0^0 , Y_2^0 , Y_4^0 , Y_4^2 , and Y_4^4 modes. These coefficients and their power spectra obtained using Prony’s method are shown in Figure 4.10.



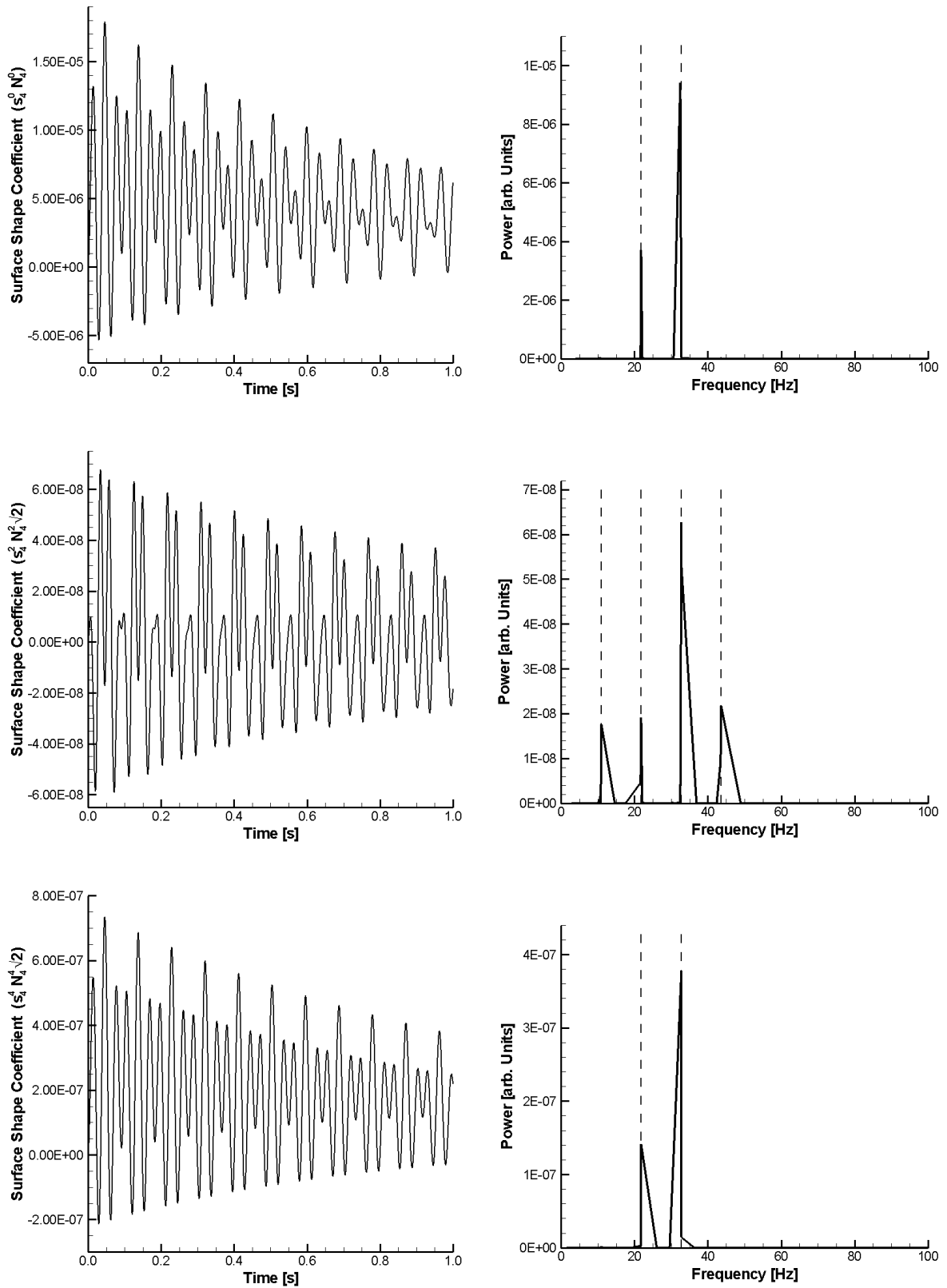


Figure 4.10 - Surface Shape Coefficients with Power Spectra, (Y^2)

The second order correction for the Y_2^2 mode has not been established but the axisymmetric inviscid analysis of Tsamopoulos and Brown (1983) suggests the existence of additional components that are proportional to the square of the amplitude but with twice the frequency. The analysis performed for the Y_2^0 mode showed good agreement with the theoretical calculations and so the same analysis is performed for the Y_2^2 mode in order to determine the higher order corrections. The results of the analysis using Prony's method for the four most dominant modes are summarised in Table 4.17.

Surface Mode	Amplitude [m]	Frequency [Hz]	Damping Coeff. [s ⁻¹]
Y_0^0	-1.33e-5	+0.00e+0	+4.35e-1
	+1.33e-5	+2.18e+1	+4.35e-1
Y_2^0	-5.24e-5	+0.00e+0	+4.34e-1
	+4.58e-5	+2.18e+1	+4.34e-1
	+6.56e-6	+1.09e+1	+2.35e-1
Y_2^2	+3.35e-3	+1.09e+1	+2.20e-1
Y_4^0	+5.71e-6	+0.00e+0	+4.34e-1
	+3.71e-6	+2.18e+1	+4.35e-1
	+9.41e-6	+3.25e+1	+1.72e+0
Y_4^4	-2.38e-7	+0.00e+0	+4.34e-1
	+1.42e-7	+2.18e+1	+4.32e-1
	-3.78e-7	+3.27e+1	+1.10e+0
Table 4.17 – Numerical Results, (Y_2^2)			

The results show that the amplitude of the Y_0^0 mode is half the input amplitude. The frequencies are multiples of those given by the Rayleigh formula. The damping rate of the dominant mode shows better agreement with the Lamb formula than the previous cases. The damping rates of the higher order components are approximately twice the damping rate of the numerical value for the main mode. There is a Y_4^0 mode component, which has the same frequency and damping rate as the component found in the analysis of the Y_2^0 case.

4.5 Summary \ Conclusions

The numerical model designed and created in this work has been applied to modelling of freely oscillating droplets for a range of three-dimensional surface oscillation modes.

The characteristics of the fluid flow within the droplet have been presented and discussed for each of the surface oscillation modes. The magnitude of velocity and Reynolds number estimates suggest that the flow is laminar in the low to moderate amplitude cases presented. Different methods of determining the composition of the surface oscillation modes in terms of amplitude, frequency, and damping rate have been applied in each of the cases studied. This analysis has shown that the frequency and damping rate of the dominant component of the surface oscillation agrees well with the low order formulae determined by the theoretical analysis of Rayleigh and Lamb.

The high accuracy of the coordinate transformation used for the surface modelling has provided the opportunity to study the higher order formulae determined by Tsamopoulos and Brown (1983). What may seem like noise is actually valuable information in the form of higher order terms in the surface expansion that are due to the nonlinear terms in the momentum equations and that are required for mass (volume) conservation. The additional components are not just found at moderate to large amplitude, they are present in low amplitude oscillations with a continuous variation as the amplitude is increased. The results for the axisymmetric mode have been compared directly with the theoretical values with good agreement. The numerical model results suggest a straight forward extension to the theoretical formula to include the effects of viscosity, something which has not previously been considered. The higher order corrections to the non-axisymmetric modes have not previously been considered and the results presented constitute the first calculation of these components.

With regards to the application to the measurement of surface tension and viscosity it is concluded that the non-linear components do not disrupt the analysis for the lowest amplitude oscillations but for higher amplitude oscillations they should be taken into account.

The work in this section has demonstrated the value of numerical modelling in confirming theoretical predictions and experimental observations. It is possible to use the numerical model to extend the theoretical analysis to the non-axisymmetric, viscous, and non-linear regimes and provide valuable insight in to the physical processes.

4.6 Further Work

The study conducted in this section could be extended to include other mode coupling phenomena including the resonant coupling described by Natarajan & Brown (1986). There is also the opportunity to extend the analytical formulae of Tsamopoulos & Brown (1983) to include three-dimensional effects even if it is only for the ($L = 2$) modes, which could then be compared with the numerical results obtained in this study. The nonlinear analysis of Tsamopoulos & Brown (1983) could also be extended to include the effects of viscosity for both axisymmetric and three-dimensional cases, which could again be compared with the numerical results already obtained in this work.

5. Diamagnetic Droplets

5.1 Overview

In this section the numerical model outlined in section 3 will be used to investigate the dynamics of a diamagnetic droplet confined by the diamagnetic force. The work in this section supplements the theoretical and numerical study for axisymmetric oscillations of a diamagnetic droplet, Easter, Bojarevics, and Pericleous (2009) and is an extension of the study presented in Easter, Bojarevics, and Pericleous (2011b). The numerical simulations are primarily designed to model the experiments on water droplets of Hill & Eaves (2010) and the theoretical comparisons are based on the model introduced in the same paper.

A solenoid magnet produces a force on a diamagnetic droplet, which with the right magnitude and spatial variation will balance the gravitational force resulting in small translational and surface shape oscillations about a stable equilibrium point. In §5.2 the changes to the numerical model required to incorporate the diamagnetic and gravitational forces are discussed. Then in §5.3 a generic form of the energy potential due to the diamagnetic and gravitational forces is introduced. In §5.4 the shift in oscillation frequency of the ($L = 2$) surface shape modes due to an ($L = 2$) mode energy potential are studied. In §5.5 the calculation of the magnetic field from a solenoid and the resulting magneto-gravitational potential are analysed and then in §5.6 and §5.7 the magnetic field calculation is used as part of the numerical model to simulate the experimental oscillations of a water droplet in both nitrogen and air atmospheres and then compared with the results of theoretical calculations.

5.2 Numerical Model Considerations

The numerical model outlined in section 3 requires some amendments to include the effects of the diamagnetic and gravitational forces. The interaction of a DC magnetic field with a diamagnetic droplet results in a repulsive force between the source of the magnetic field and the droplet, the force per unit volume is:

$$\mathbf{F}_{vol} = \frac{\chi_V \nabla(\mathbf{B}^2)}{2 \mu_0} \quad (5.1)$$

In terrestrial conditions the gravitational force is also present:

$$\mathbf{F}_{vol} = -\rho g \nabla z \quad (5.2)$$

These two forces are potential and are implemented in the numerical model by solving for a ‘modified’ pressure:

$$P_{mod} = P + \rho g z - \frac{\chi_V |\mathbf{B}|^2}{2 \mu_0} \quad (5.3)$$

This requires that the normal stress boundary condition be modified to include the additional terms:

$$\mathbf{e}_n \cdot \Pi_{mod} \cdot \mathbf{e}_n = \Gamma K + \rho g z - \frac{\chi_V |\mathbf{B}|^2}{2 \mu_0} \quad (5.4)$$

The modified stress tensor is:

$$\Pi_{i,j,mod} = 2 \nu \rho e_{i,j} - P_{mod} \delta_{i,j} \quad (5.5)$$

5.3 Magneto-Gravitational Potential Energy

Although the dynamics of the droplet considered will be three dimensional the magnetic forces considered will be axisymmetric. The combined diamagnetic and gravitational forces can be represented by the gradient of a potential energy function:

$$\mathbf{F} = -\nabla U(r, \theta) \quad (5.6)$$

This magneto-gravitational potential energy is assumed to be axisymmetric and so can be given as a series expansion of Legendre polynomials with radially dependent coefficients:

$$U(r, \theta) = \sum_{j \geq 0} C_j(r) P_j(\cos \theta) \quad (5.7)$$

Using this approach the coefficients can be determined for a given magnetic field and the impact on the oscillation frequencies can be determined using the theoretical model.

5.4 $L = 2$ Mode Energy Potential

The initial numerical simulation will be used to investigate the effect of an ($L = 2$) mode energy potential on the ($L = 2$) mode surface shape oscillations. Theoretical considerations based on the work of Hill & Eaves (2010) suggest that the energy potential will have a different effect on each of the three ($L = 2$) mode surface shapes. For freely oscillating droplets the frequency is degenerate but in the presence of the energy potential the degeneracy is lifted and the frequency of each of the three components is different. The theoretical model assumes the droplet has a surface shape, which consists of a small perturbation from a sphere with the perturbation consisting of an axisymmetric static deformation due to the magnetic field and a transient three-dimensional component:

$$r_s(\theta, \phi, t) = R_0 \left(1 + \sum_{L=1}^{L=\infty} x_L P_L(\cos \theta) + \sum_{L=0}^{L=\infty} \sum_{M=-L}^{M=L} s_L^M(t) Y_L^M(\theta, \phi) \right) \quad (5.8)$$

The time dependence of the three-dimensional coefficients are assumed to be harmonic $s_L^M(t) = \cos(\omega_L^M t)$. An approximation for the coefficients of the static deformation series expansion can be determined from the energy potential coefficients:

$$x_j = - \frac{C_j(R_0)}{(j-1)(j+2)} \frac{\rho R_0^2}{\Gamma} \quad (5.9)$$

The frequency of oscillation is given in terms of a shift from the normal mode frequency determined by Rayleigh (1879):

$$(\omega_L^M)^2 = \frac{L(L-1)(L+2)\Gamma}{\rho R_0^3} + \Delta\omega^2 \quad (5.10)$$

The frequency shift consists of two components; the first proportional to the force on the droplet and the second proportional to the static deformation:

$$\Delta\omega^2 = \frac{L}{R_0} \left(\frac{\partial C_0}{\partial r} + \frac{\partial C_j}{\partial r} \right) - \frac{\Gamma x_j q}{\rho R_0^4} \left[3L(L-1) + j(j+1) \left(2L + \frac{(L-1)(L+2)}{2} \right) \right] \quad (5.11)$$

The derivatives of the energy potential coefficients are evaluated at R_0 . The static deformation term is related to the energy potential (5.7) and constitutes the dominant component in the frequency shift. The q values are mode dependent and the values for the ($L = 2$) modes are:

	Y_2^0	Y_2^1	Y_2^2
q	$2/7$	$1/7$	$-2/7$
Table 5.1 – q values for the ($L = 2$) modes			

This gives everything that is needed to calculate the first order correction to the oscillation frequencies for the ($L = 2$) modes. These equations are part of an eigenvalue problem for the oscillation frequencies, which includes additional small terms. The higher order corrections can be calculated by the eigenfrequency analysis but only become significant when the potential is large. Figure 5.1 shows the eigenfrequency analysis for the ($L = 2$) modes in an ($L = 2$) mode energy potential.

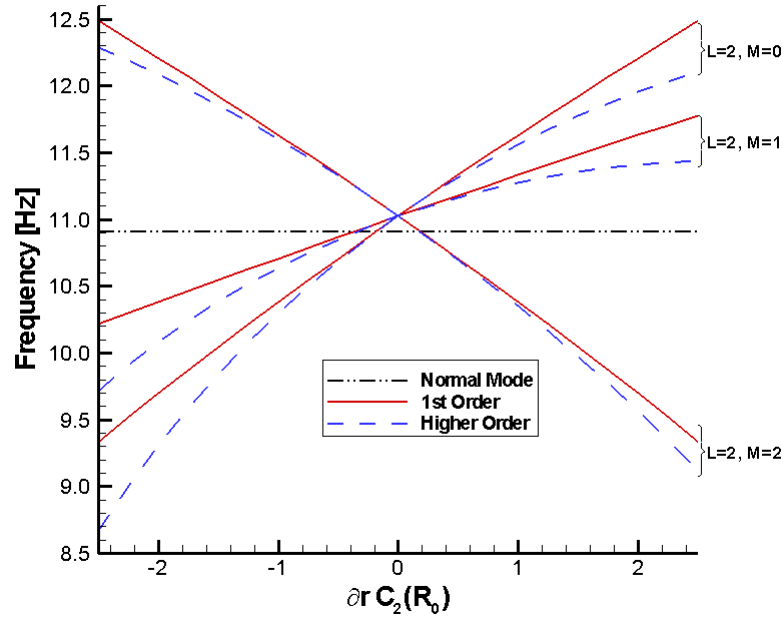


Figure 5.1 – Eigenfrequencies of the ($L = 2$) Modes

The potential chosen for the numerical simulation is:

$$U(r, \theta) = -150.0 r^2 P_2(\cos \theta) \quad (5.12)$$

This corresponds to $\partial C_2 / \partial r = -1.5$ for a droplet with unperturbed radius $R_0 = 5\text{mm}$, which is sufficient to observe splitting of the ($L = 2$) mode frequencies and a frequency shift that requires the higher order terms to be taken into account.

The numerical simulation uses a superposition of the ($L = 2$) surface shape modes for the initial condition:

$$r_s = R_0(1 + s_0^0 Y_0^0 + s_2^0 Y_2^0 + s_2^1 Y_2^1 + s_2^2 Y_2^2) \quad (5.13)$$

Where the spherical harmonics follow the definition given in section 3 and can be obtained using the recurrence relations used in the numerical model:

$$\begin{aligned}
Y_0^0 &= N_0^0 \\
Y_2^0 &= N_2^0 \frac{1}{2} (3 \cos^2 \theta - 1) \\
Y_2^1 &= -N_2^1 \sqrt{2} (3 \sin \theta \cos \theta) \cos \phi \\
Y_2^2 &= N_2^2 \sqrt{2} (3 \sin^2 \theta) \cos 2\phi
\end{aligned}
\tag{5.14}$$

The amplitudes for the non-axisymmetric modes are chosen to give a maximum deformation of 1% of the unperturbed radius. The axisymmetric mode has a larger amplitude coefficient, which is chosen to reduce the amplitude of oscillation based on the static deformation estimate. A constant component is also required to ensure the initial surface shape conserves the mass of the droplet based on the equilibrium spherical radius:

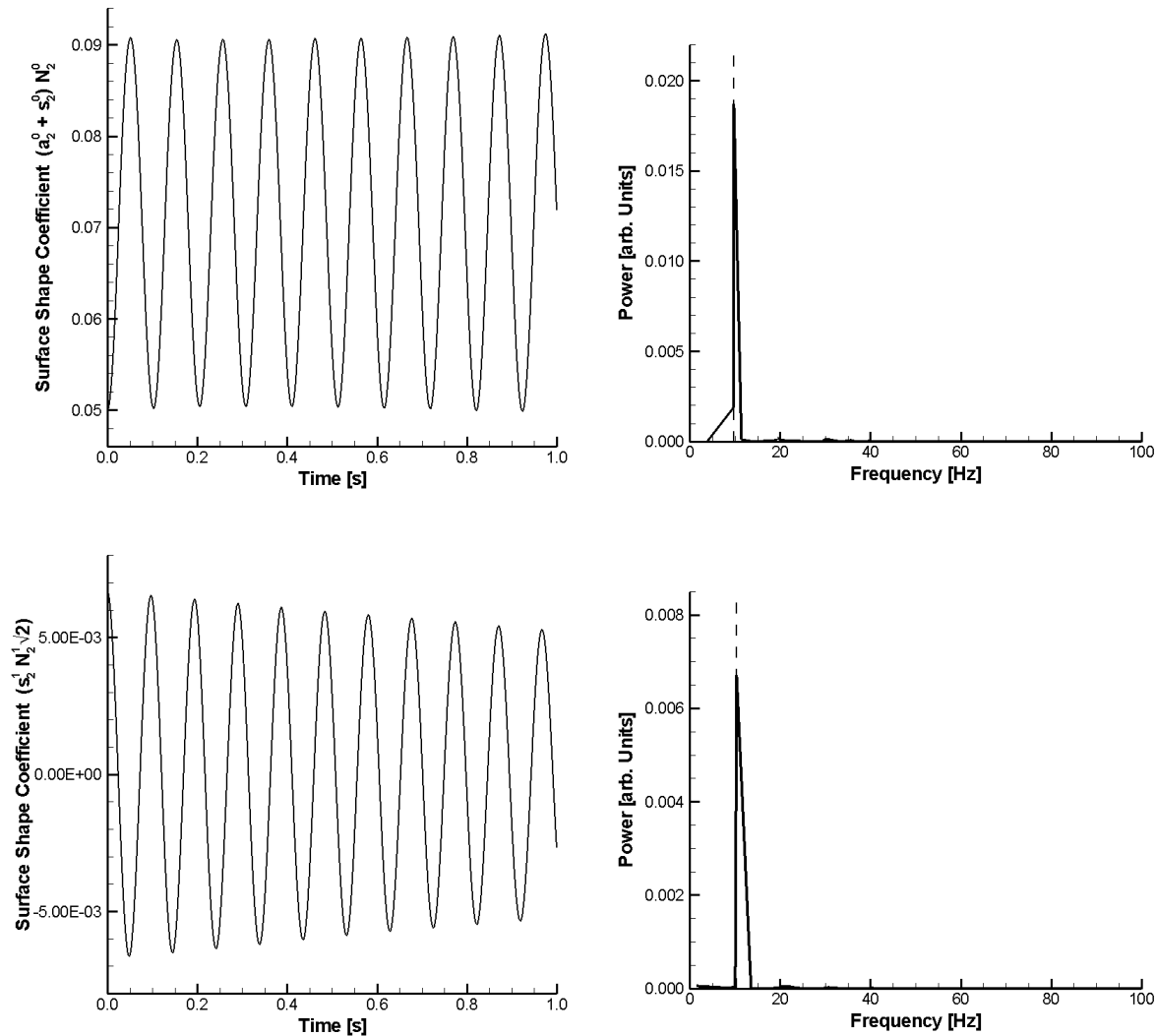
$s_0^0 N_0^0$	$s_2^0 N_2^0$	$s_2^1 N_2^1 \sqrt{2}$	$s_2^2 N_2^2 \sqrt{2}$
-5.56e-4	+5.00e-2	+6.67e-3	+3.33e-3
Table 5.1 – Initial Conditions, (Y_2^0, Y_2^1, Y_2^2)			

The material used for the simulations is water and the physical properties values used in the numerical model are:

Symbol	Quantity	Value	Units	Reference
Γ	Surface Tension Coefficient	+7.33e-2	N m ⁻¹	Hill and Eaves (2010)
ρ	Density	+9.99e+2	Kg m ⁻³	
ν	Kinematic Viscosity	+1.11e-6	m ² s ⁻¹	
χ_V	Volumetric Magnetic Susceptibility	-9.00e-6	-	
Table 5.2 – Material Properties (Water)				

The numerical procedure described in section 3 is used to analyse the surface shape at each time-step in order to determine the relative contribution of each mode. This results in a time dependent coefficient for each of the spherical harmonic modes. The dominant components are the ($L = 2$) modes with other small components that are present due to nonlinear effects. Figure 5.2 shows the transient coefficients for the ($L = 2$) modes with

their power spectra obtained using Prony's method (described in §3.6.6). The theoretical values for the modified frequencies are indicated in the power spectra with dashed lines.



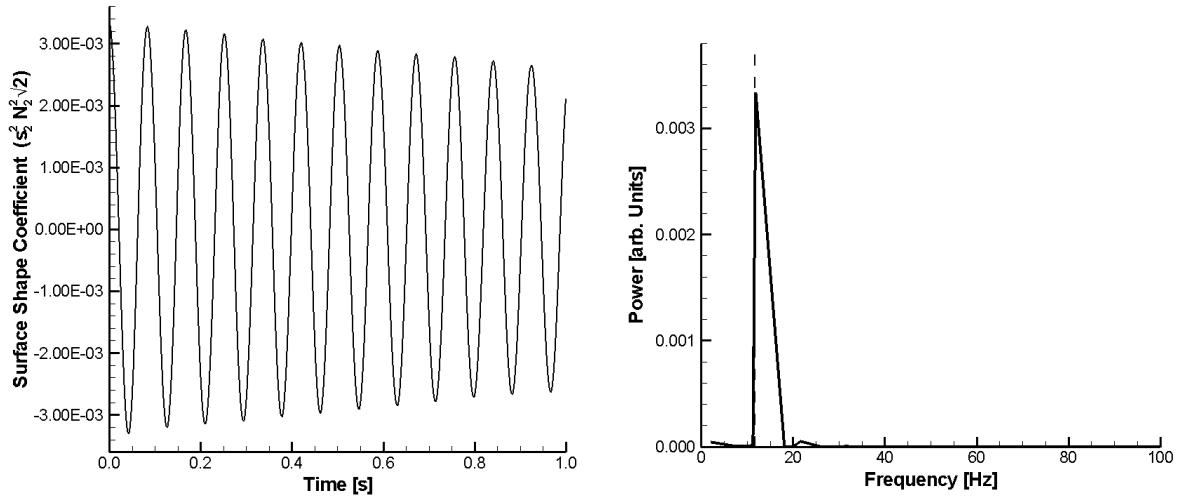


Figure 5.2 –Surface Shape Coefficients, (Y^0_2, Y^1_2, Y^2_2)

Table 5.3 shows the frequencies calculated using the theoretical formulae and the frequencies calculated numerically. There is reasonably good agreement between the theoretical and numerical values. The frequency shifts are small, but not insignificant when considered in the context of surface tension measurements.

	Y^0_1	Y^0_2	Y^1_2	Y^2_2
Normal Mode	N/A	+1.09e+1	+1.09e+1	+1.09e+1
Theoretical (First Order)	N/A	+9.92e+0	+1.04e+1	+1.18e+1
Theoretical (Higher Order)	N/A	+9.71e+0	+1.03e+1	+1.17e+1
Numerical	N/A	+9.74e+0	+1.03e+1	+1.19e+1

Table 5.3 – Frequency Calculations, (Y^0_2, Y^1_2, Y^2_2)

5.5 Solenoid Magnet Potential

The next test case considered is for a water droplet in the magnetic field of a solenoid. The magnetic field can be approximated as a superposition of the magnetic field generated by axisymmetric coils. The axisymmetric magnetic field in cylindrical coordinates, $\mathbf{B}(\rho, 0, z) = (B_\rho, 0, B_z)$, is obtained from the analytical formulae:

$$B_{\rho} = \frac{\mu_0 I}{2 \pi} \frac{z}{\rho \sqrt{(a + \rho)^2 + z^2}} \left[-K + \frac{a^2 + \rho^2 + z^2}{(a - \rho)^2 + z^2} E \right] \quad (5.15)$$

$$B_z = \frac{\mu_0 I}{2 \pi} \frac{1}{\sqrt{(a + \rho)^2 + z^2}} \left[K + \frac{a^2 - \rho^2 - z^2}{(a - \rho)^2 + z^2} E \right] \quad (5.16)$$

Where, a = coil radius, I = electric current, K , E are the complete elliptic integrals of the first and second kind respectively with argument, $k^2 = 4 a \rho [(a + \rho)^2 + z^2]^{-1}$. The formulae are taken from Smythe (1950).

The solenoid consists of a number of coil windings that can be viewed as a set of blocks with a filament placed in the centre of each block. The magnetic field components can then be summed over all blocks to give the field from all windings. The accuracy of the magnetic field calculation and the resulting frequency modification depends on the dimensions used for the windings and also the number of filaments used. Figure 5.3 shows a plot of the filament positions with the coil geometry designed to capture the characteristics of a commercial superconducting solenoid magnet used in experiments. Also indicated are the size of the bore of the magnet and a window surrounding the stable levitation zone.

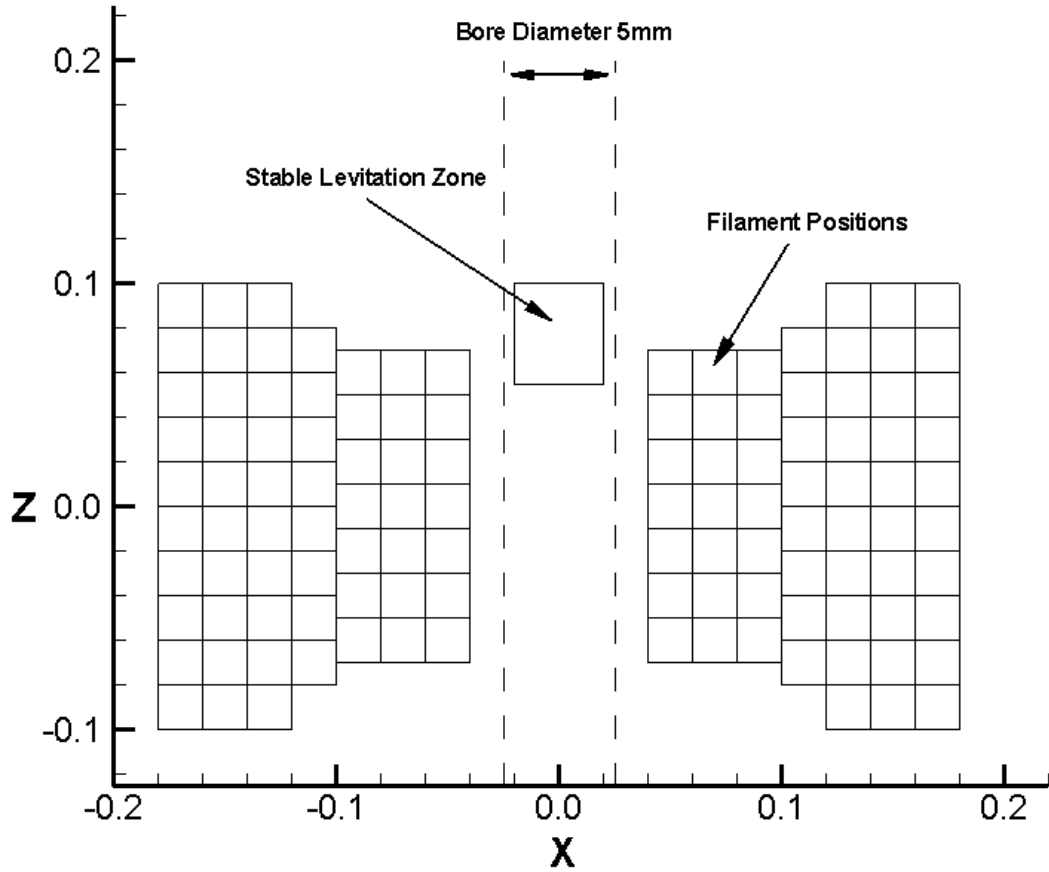


Figure 5.3 – Solenoid Magnet

The magneto-gravitational potential energy for the combined gravitational and diamagnetic potentials is given by:

$$U = g z - \frac{\chi_V |\mathbf{B}|^2}{2 \rho \mu_0} \quad (5.17)$$

The stable levitation conditions can be established by adjusting the electric current in the coils to form a minimum in the magneto-gravitational potential energy characterised by the magnetic field at the centre of the magnet (B_0). The energy is calculated using the magnetic field data scaled to give a field strength, $B_0 = 16.5$ T.

Figure 5.4 shows a contour plot of the magneto-gravitational potential with contour lines ($\nabla U = 0.05e^{-3} g$). The equilibrium shape of the droplet will follow the contour lines of the energy potential (axisymmetric shape) but gravity is not exactly compensated at all

points and so it is not straightforward to determine the stable levitation position. The stable levitation position will be on the z-axis due to axisymmetry of the coils and an initial approximation can be made by considering the energy minimum on the z-axis. The turning points are determined by the derivative of the energy along the z-axis ($U_z = 0$) and whether they are maxima or minima are then determined by sign of the second derivative (U_{zz}). The analysis shows that there is a local maxima (unstable levitation point) and local minima (stable levitation point). Figure 5.5 shows the energy on the z-axis with the local minima highlighted.

The energy expansion coefficients (C_j) and their derivatives are determined using a numerical procedure in a similar way to the determination of the surface expansion coefficients. The expansion is made about the estimated stable levitation point, ($z = 0.0744$ m, $\rho = 0$ m). Figure 5.6 shows the coefficients and Figure 5.7 the derivatives of the coefficients in the radial direction. The lower order modes are most dominant and the series is found to converge with the contribution of the higher order modes decreasing to zero.

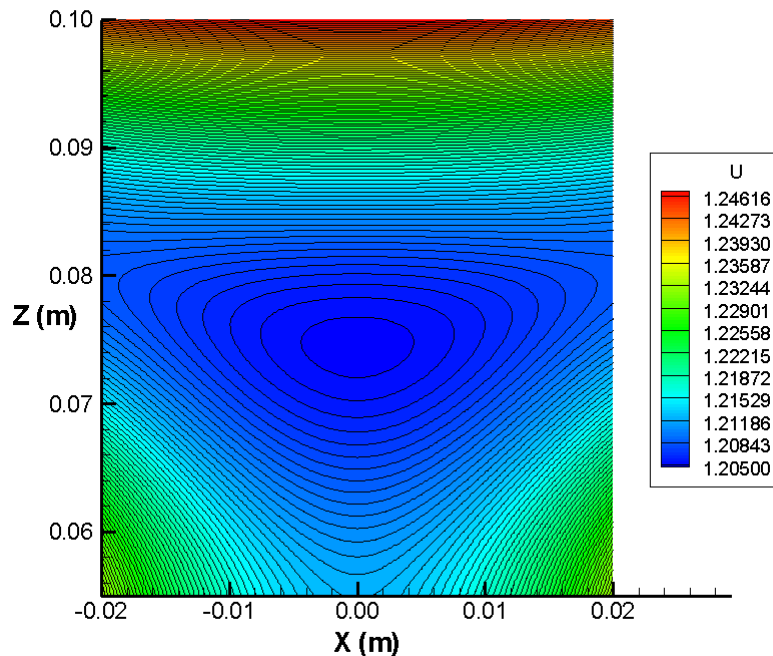


Figure 5.4 - Magneto-Gravitational Potential, (Nitrogen)

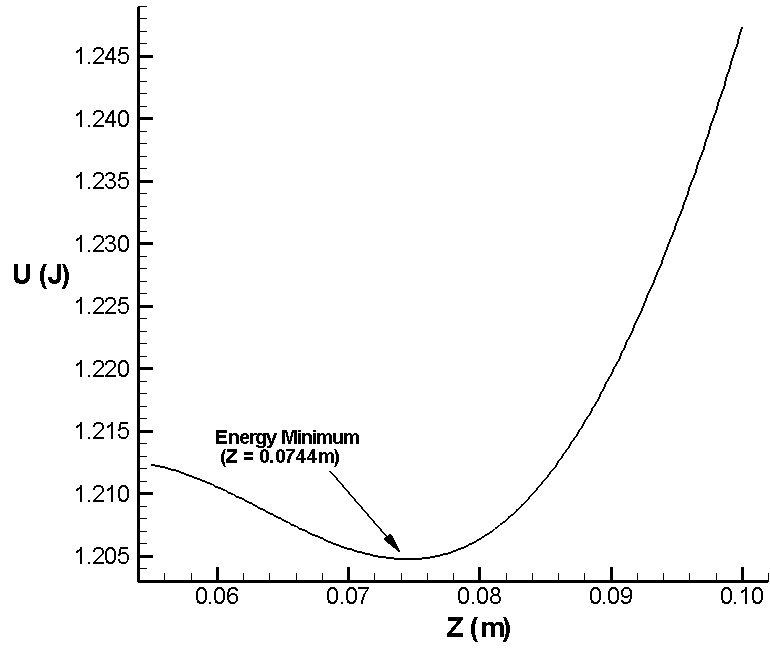


Figure 5.5 – Energy Potential (z-axis), (Nitrogen)

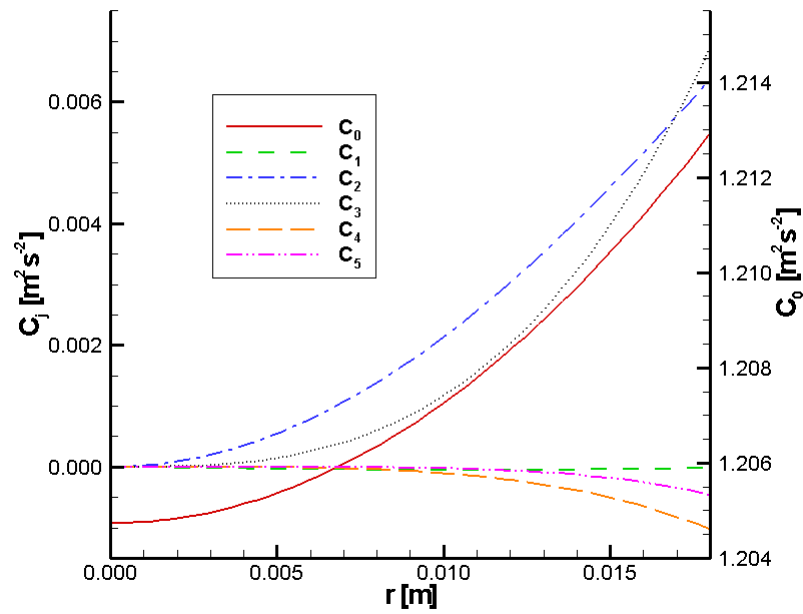


Figure 5.6 – Energy Expansion Coefficients, (Nitrogen)

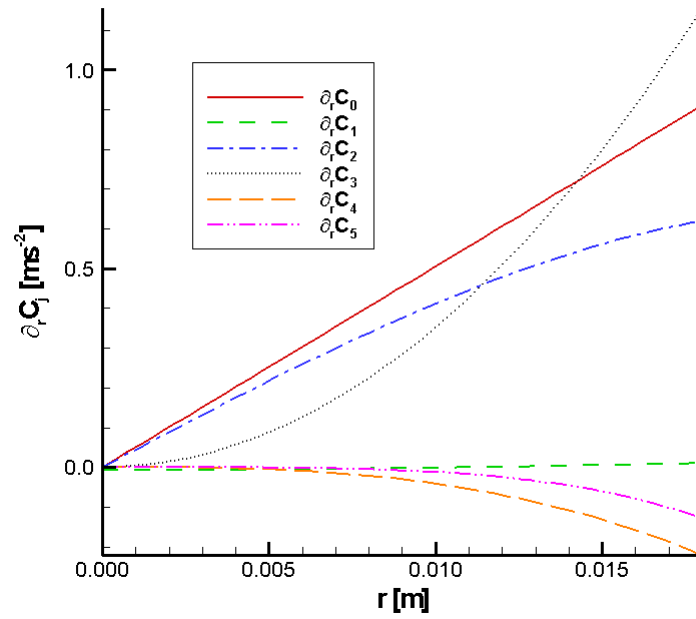


Figure 5.7 – Radial Derivative of the Energy Expansion Coefficients, (Nitrogen)

The frequency shift is dependent on both the energy expansion coefficients and the derivative of the coefficients in the radial direction. The derivative of the C_0 coefficient is positive and increasing with radial distance from the stable levitation point resulting in an increase in frequency. There is no static deformation for an incompressible fluid in a spherically symmetric potential ($j = 0$) as it would violate mass continuity, therefore there is no contribution to the frequency shift from the static deformation term related to this coefficient. The ($j = 2$) component is positive and contributes a small increase in frequency. The magnitude of the ($j = 3$) component is comparable to the ($j = 2$) component but there is no contribution to the frequency shift at first order. There is also very little variation in the ($j = 1$) coefficient, the source of vertical motion, confirming that the estimate for the stable levitation point was accurate.

5.6 Solenoid Magnet Potential, Nitrogen Atmosphere

The numerical simulation uses the Y_2^1 surface shape mode for the initial condition:

$$r_s = R_0(1 + s_0^0 Y_0^0 + s_2^1 Y_2^1) \quad (5.18)$$

The spherical harmonics follow the definition given in section 3 and can be obtained using the recurrence relations used in the numerical model:

$$\begin{aligned} Y_0^0 &= N_0^0 \\ Y_2^1 &= -N_2^1 \sqrt{2} (3 \sin \theta \cos \theta) \cos \phi \end{aligned} \quad (5.19)$$

The amplitude coefficient is chosen to give a maximum deformation of 1% of the unperturbed radius ($R_0 = 5\text{mm}$). A constant component is also required to ensure the initial surface shape conserves the mass of the droplet based on the equilibrium spherical radius:

$s_0^0 N_0^0$	$s_2^1 N_2^1 \sqrt{2}$
-2.67e-5	+6.67e-3
Table 5.4 – Initial Conditions, (Nitrogen)	

The material used for the simulations is water and the physical properties values used in the numerical model are given in Table 5.2. Figure 5.8 shows the droplet in the solenoid magnet and the initial condition used in the simulation.

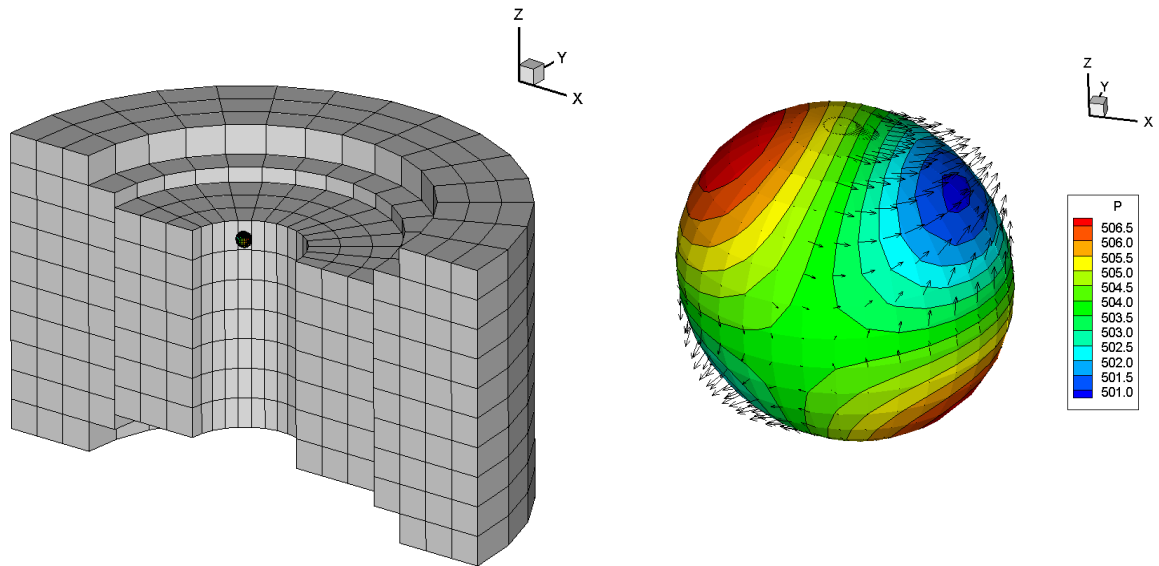
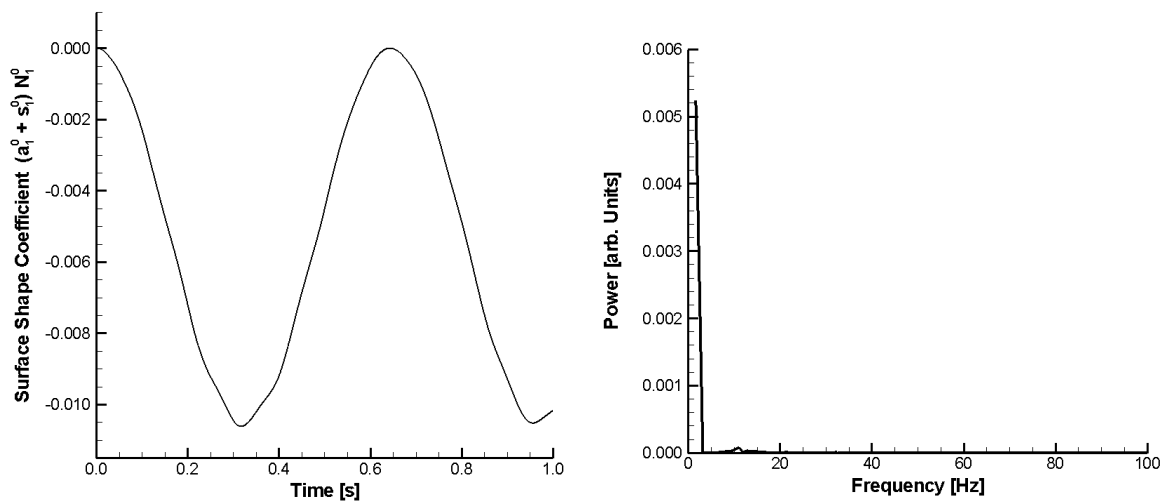


Figure 5.8 – Droplet in Solenoid Magnet, (Nitrogen)

The numerical procedure described in section 3 is used to analyse the surface shape at each time-step in order to determine the relative contribution of each mode. This results in a time dependent coefficient for each of the spherical harmonic modes. The dominant components are the Y^l_2 mode, which corresponds to the initial condition, axisymmetric modes Y^0_2 , and Y^0_3 , which are introduced by the external forces, and the Y^0_1 translational mode also introduced by the external forces. Other small components are also present due to nonlinearity. Figure 5.9 shows the transient coefficients for the dominant modes with their power spectra obtained using Prony's method (described in §3.6.6).



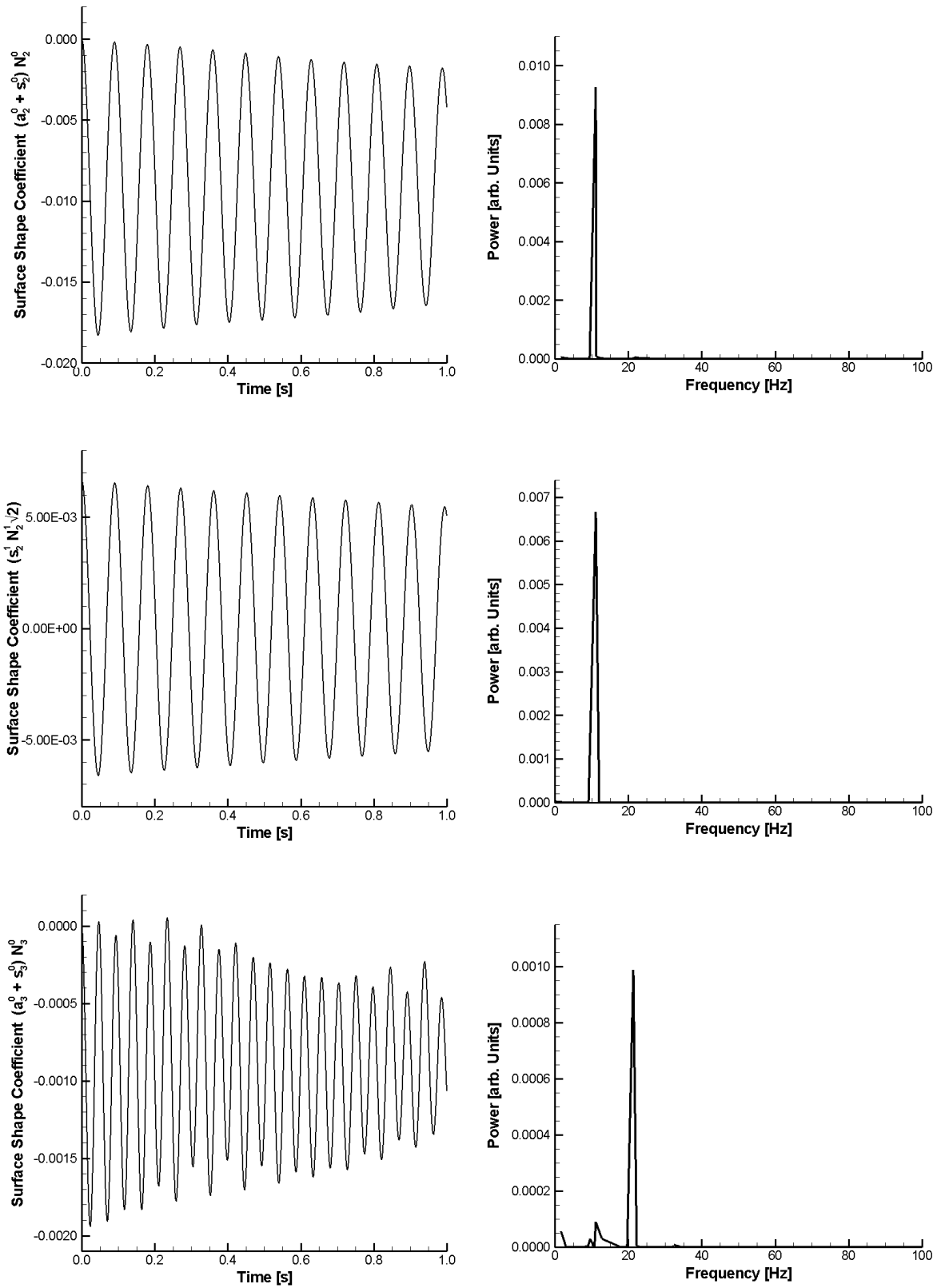


Figure 5.9 – Surface Shape Coefficients, (Nitrogen)

The power spectra are mostly dominated by a single peak, however additional small peaks can be seen in the in the power spectra for the Y_3^0 mode, which corresponds to the frequencies of the Y_1^0 and Y_2^0 modes.

The energy expansion coefficients calculated in section §5.5 provide the information required to determine the shift in frequency due to the gravitational and diamagnetic forces. The coefficients evaluated at the unperturbed droplet radius ($R_0 = 5\text{mm}$) are:

Mode No.	0	1	2	3	4	5
C	+1.21e+0	-3.26e-5	+5.49e-4	+1.46e-4	-6.49e-6	-7.14e-7
C_r	+2.53e-1	-5.55e-3	+2.18e-1	+8.80e-2	-5.20e-3	-7.30e-4

Table 5.5 – Series Expansion Coefficients and Derivative at R_0 , (Nitrogen)

Table 5.6 shows the frequencies calculated using the theoretical formulae and the frequencies calculated numerically. There is reasonably good agreement between the theoretical and numerical values. The frequency shifts are small, but not insignificant when considered in the context of surface tension measurements.

	Y_1^0	Y_2^0	Y_2^1	Y_3^0
Normal Mode	N/A	+1.09e+1	+1.09e+1	+2.11+1
Theoretical (First Order)	N/A	+1.12e+1	+1.11e+1	+2.14e+1
Numerical	+1.62e+0	+1.11e+1	+1.11e+1	+2.13e+1

Table 5.6 – Frequency Calculations, (Nitrogen)

5.7 Solenoid Magnet Potential, Air Atmosphere

The next numerical test case corresponds to the experiment conducted with a water droplet in an air atmosphere. When the droplet is surrounded by air, there is an additional force due to the paramagnetic properties of the air. The magneto-gravitational potential energy (per unit mass) in this case is given by:

$$U_{mass} = g z - \frac{\chi_V^{Water} |\mathbf{B}|^2}{2 \rho \mu_0} + \frac{\chi_V^{Air} |\mathbf{B}|^2}{2 \rho \mu_0} \quad (5.20)$$

The stable levitation conditions are again established by adjusting the electric current in the coils to form a minimum in the magneto-gravitational potential energy. The energy is calculated using the magnetic field data scaled to give a field strength of $B_0 = 16.5$ T. The change in energy due to the surrounding fluid is equivalent to a change in the magnetic susceptibility and has a different effect to just adjusting the electric current in the solenoid. It is possible that lower field strength could be used due to the additional force generated by the paramagnetic properties of the surrounding gas. This would result in a different stable levitation point and different variation in the energy field.

The magnetic susceptibility of air used in the energy calculation is:

Symbol	Quantity	Value	Units	Reference
χ_V	Volumetric Magnetic Susceptibility	+3.70e-7	-	Hill and Eaves (2010)
Table 5.7 – Material Properties (Air)				

Figure 5.10 shows a contour plot of the magneto-gravitational potential with contour lines ($\nabla U = 0.05e^{-3}$ g). The equilibrium shape of the droplet will follow the contour lines of the energy potential (axisymmetric shape) but gravity is not exactly compensated at all points and so it is not straightforward to determine the stable levitation position. The stable levitation position will be on the z-axis due to axisymmetry of the coils and an initial approximation can be made by considering the energy minimum on the z-axis. The turning points are determined by the derivative of the energy along the z-axis ($U_z = 0$) and whether they are maxima or minima are then determined by sign of the second derivative (U_{zz}). The analysis shows that there is a local maxima (unstable levitation point) and local minima (stable levitation point). Figure 5.11 shows the energy on the z-axis with the local minima highlighted.

The energy expansion coefficients (C_j) and their derivatives are determined using a numerical procedure in a similar way to the determination of the surface expansion

coefficients. The expansion is made about the estimated stable levitation point, ($z = 0.0782$ m, $\rho = 0$ m). The estimated stable levitation point is closer to the top of the solenoid in this case. Figure 5.12 shows the coefficients and Figure 5.13 the derivatives of the coefficients in the radial direction. The lower order modes are most dominant and the series is found to converge with the contribution of the higher order modes decreasing to zero. They show the same qualitative behaviour as the nitrogen case even though the expansion is taken about a different point.

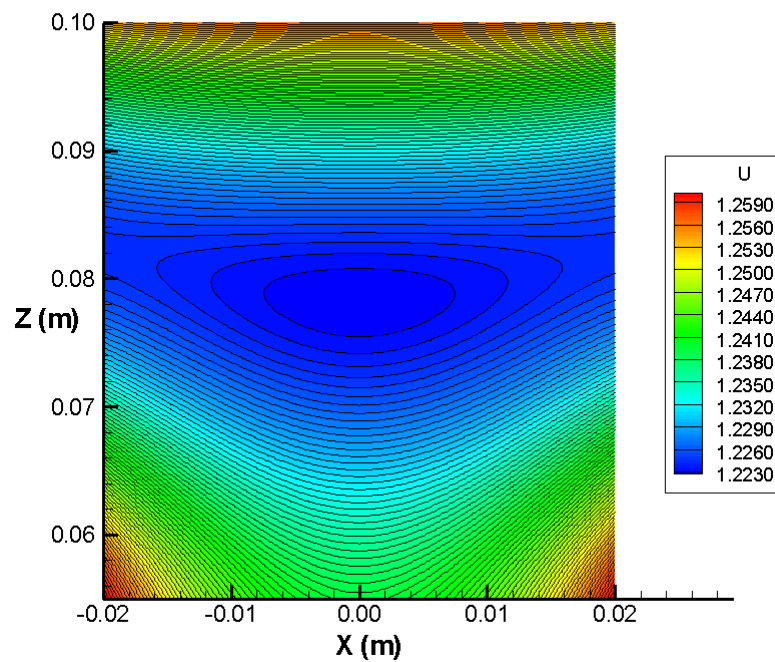


Figure 5.10 - Magneto-Gravitational Potential, (Air)

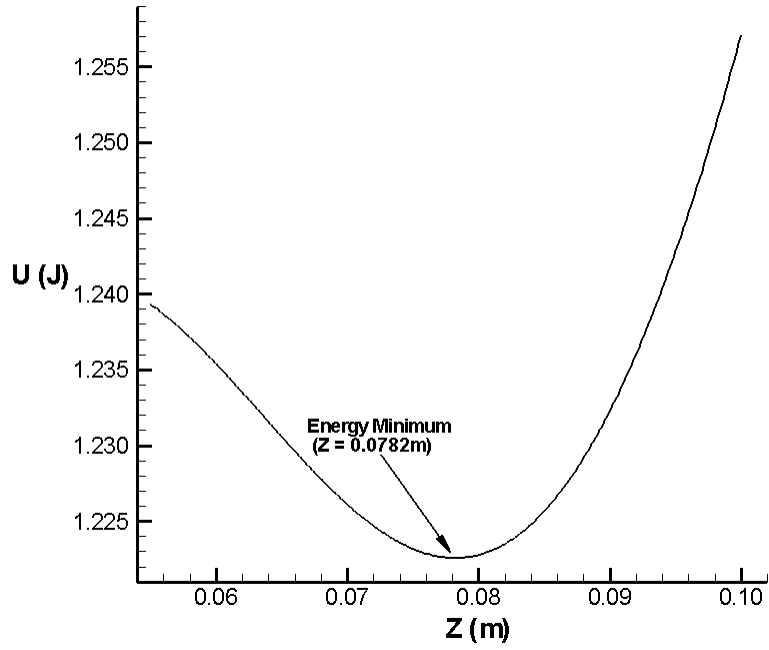


Figure 5.11 – Energy Potential (z-axis), (Air)

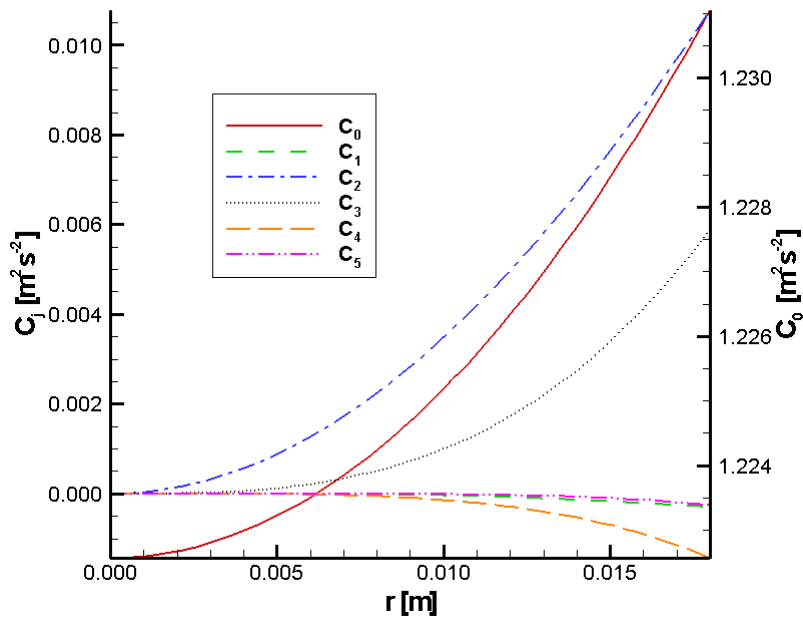


Figure 5.12 – Energy Expansion Coefficients, (Air)

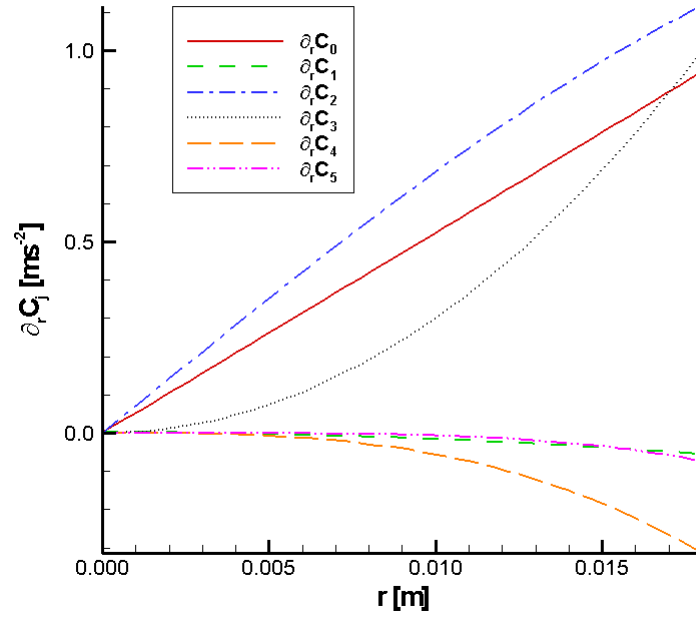


Figure 5.13 – Radial Derivative of the Energy Expansion Coefficients, (Air)

The frequency shift is dependent on both the energy expansion coefficients and the derivative of the coefficients in the radial direction. The derivative of the ($j = 0$) coefficient is positive and increasing with radial distance from the stable levitation point resulting in an increase in frequency. There is no static deformation for an incompressible fluid in a spherically symmetric potential ($j = 0$) as it would violate mass continuity, therefore there is no contribution to the frequency shift from the static deformation term related to this coefficient. The ($j = 2$) mode component is positive and contributes a small increase in frequency. The magnitude of the ($j = 3$) mode component is comparable to the ($j = 2$) mode component but there is no contribution to the frequency shift at first order. There is also very little variation in the ($j = 1$) coefficient, the source of vertical motion, confirming that the estimate for the stable levitation point was accurate.

The numerical simulation uses the Y_2^2 surface shape mode for the initial condition:

$$r_s = R_0(1 + s_0^0 Y_0^0 + s_2^2 Y_2^2) \quad (5.21)$$

The spherical harmonics follow the definition given in section 3 and can be obtained using the recurrence relations used in the numerical model:

$$Y_0^0 = N_0^0 \tag{5.22}$$

$$Y_2^2 = N_2^2 \sqrt{2} (3 \sin^2 \theta) \cos 2\phi$$

The amplitude coefficient is chosen to give a maximum deformation of 1% of the unperturbed radius ($R_0 = 5\text{mm}$). A constant component is also required to ensure the initial surface shape conserves the mass of the droplet based on the equilibrium spherical radius:

$s_0^0 N_0^0$	$S_2^2 N_2^2 \sqrt{2}$
-2.67e-5	+3.33e-3
Table 5.8 – Initial Conditions, (Air)	

The material used for the simulations is water and the physical properties values used in the numerical model are given in Table 5.2. Figure 5.14 shows the droplet in the solenoid magnet and the initial condition used in the simulation.

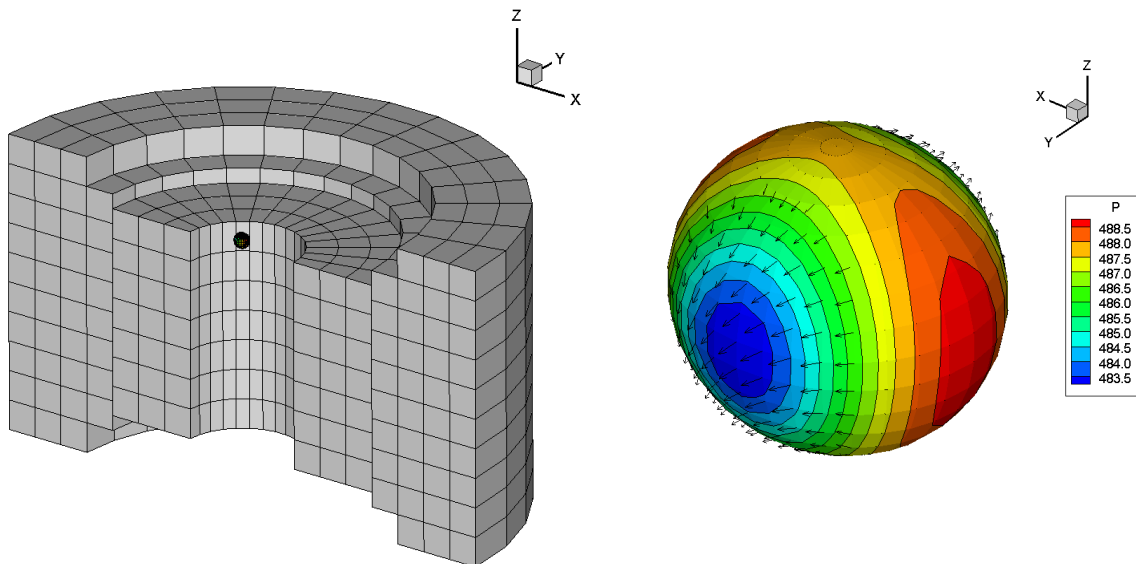
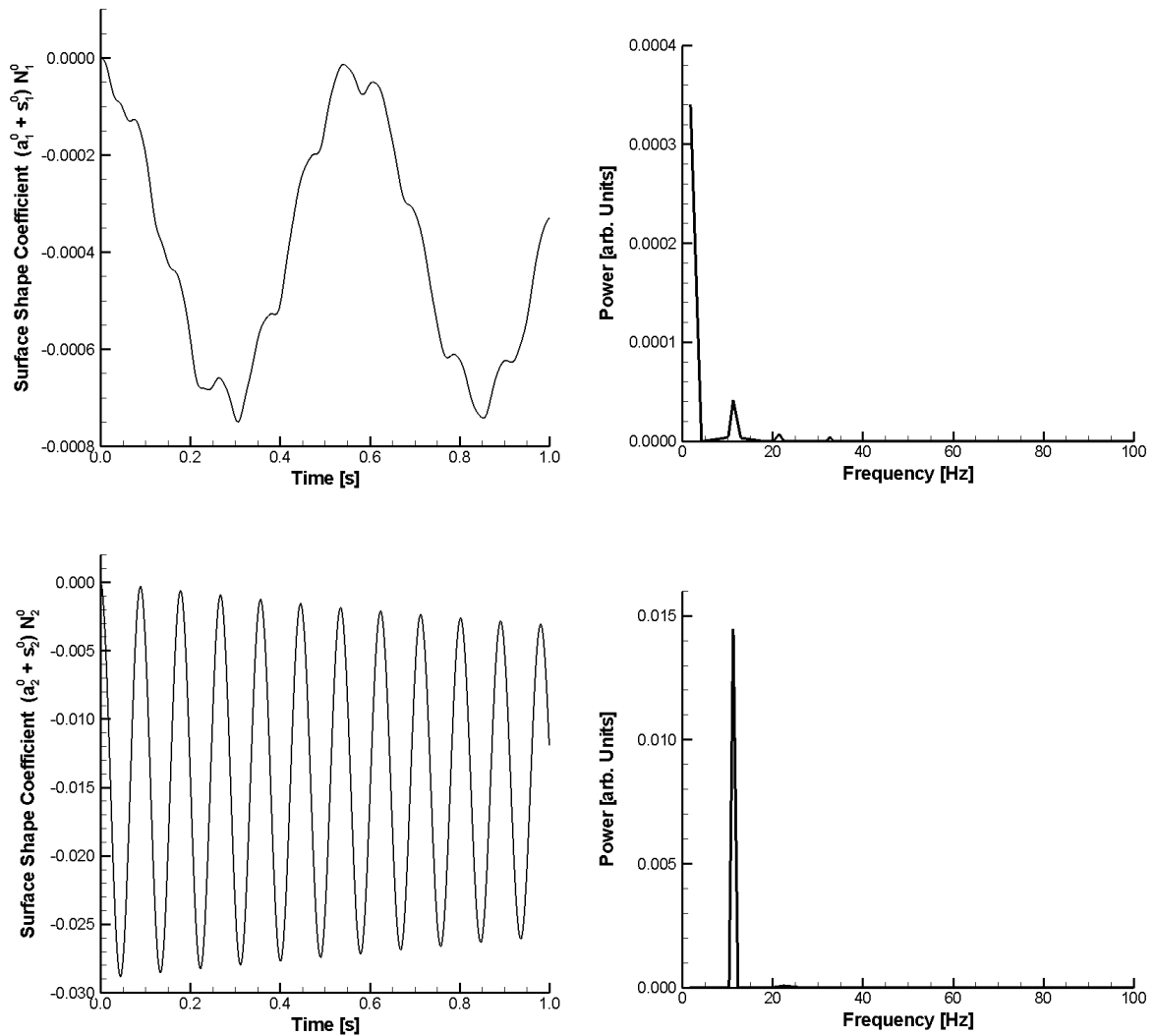


Figure 5.14 – Droplet in Solenoid Magnet, (Air)

A numerical procedure is used to analyse the surface shape at each time-step in order to determine the relative contribution of each mode. This results in a time dependent coefficient for each of the spherical harmonic modes. The dominant components are the Y_2^2 mode, which corresponds to the initial condition, axisymmetric modes Y_2^0 , and Y_3^0 , which are introduced by the external forces, and the Y_1^0 translational mode, which is also introduced by the external forces. Other small components are also present due to nonlinearity. Figure 5.15 shows the transient coefficients for the dominant modes with their power spectra obtained using Prony's method (described in §3.6.6).



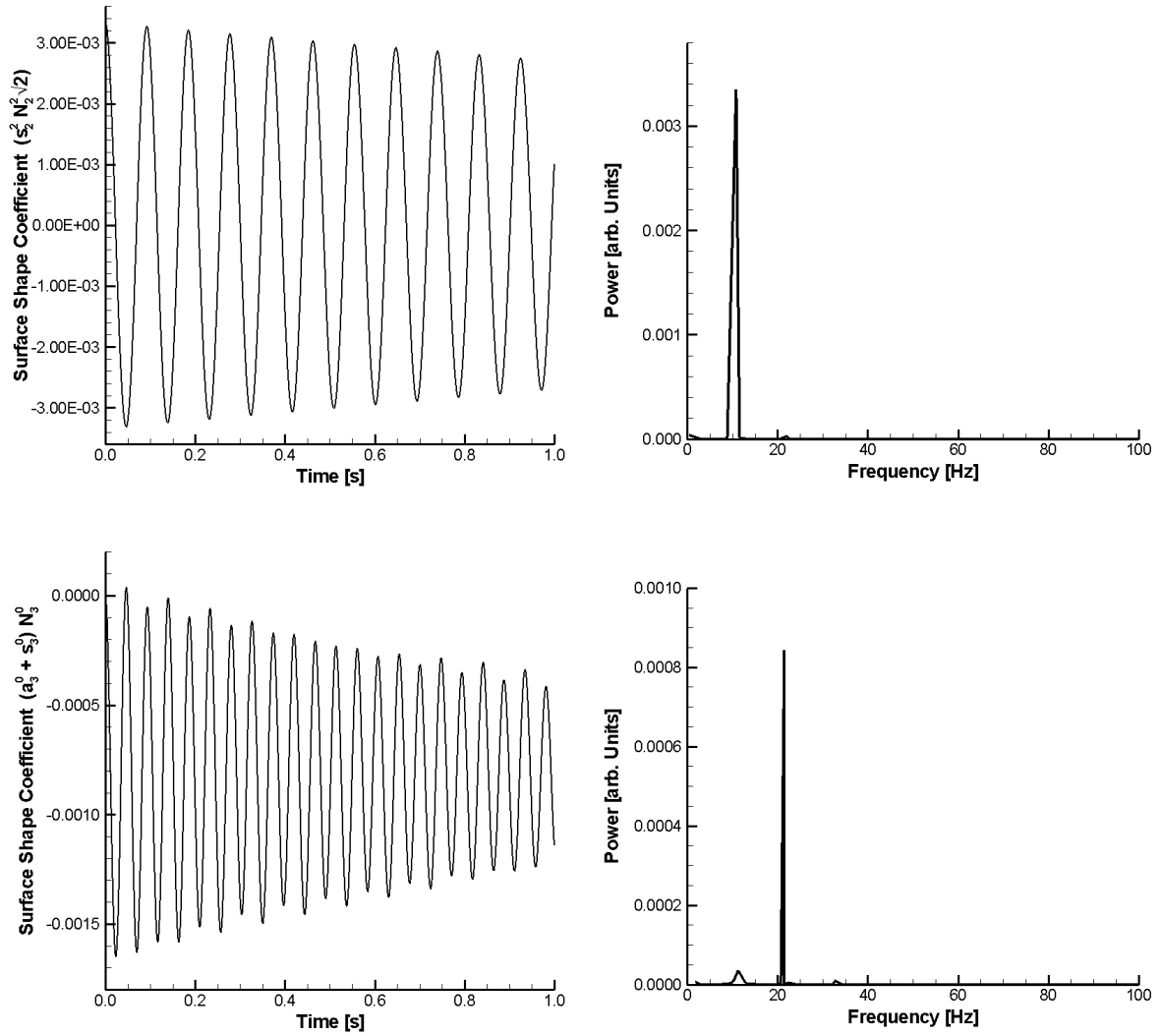


Figure 5.15 – Surface Shape Coefficients, (Air)

The power spectra are mostly dominated by a single peak, however additional small peaks can be seen in the power spectra for the Y_3^0 mode, which correspond to the frequencies of the Y_1^0 and Y_2^0 modes.

The energy expansion coefficients calculated above provide the information required to determine the shift in frequency due to the gravitational and electromagnetic forces. The coefficients evaluated at the unperturbed droplet radius ($R_0 = 5$ mm) are:

Mode No.	0	1	2	3	4	5
C	+1.22e+0	+4.23e-6	+8.85e-4	+1.24e-4	-8.78e-6	-3.63e-7
C_r	+2.62e-1	-2.17e-3	+3.52e-1	+7.46e-2	-7.05e-3	-3.80e-4

Table 5.9 – Series Expansion Coefficients and Derivative at R_0 , (Air)

Table 5.10 shows the frequencies calculated using the theoretical formulae and the frequencies calculated numerically. There is reasonably good agreement between the theoretical and numerical values. The frequency shifts are small, but not insignificant when considered in the context of surface tension measurements.

	Y_1^0	Y_2^0	Y_2^2	Y_3^0
Normal Mode	N/A	1.09e+1	1.09e+1	2.11+1
Theoretical (First Order)	N/A	1.12e+1	1.08e+1	2.15e+1
Numerical	1.78e+0	1.12e+1	1.08e+1	2.14e+1

Table 5.10 – Frequency Calculations, (Air)

5.8 Summary \ Conclusions

The results of the numerical simulations have shown good agreement with the calculations made using the theoretical model of Hill and Eaves (2010). This has revealed a number of interesting consequences for the use of the oscillating droplet technique for measuring surface tension using diamagnetic levitation. Accurate knowledge of the spatial variation in the magnetic field is required in order to determine the modification to the oscillation frequencies. While stable levitation is possible at a range of magnetic field strengths (electric current) the shape of the energy potential can vary over this range resulting in a different response in the oscillation frequency.

There are many approximations involved in determining the surface tension and viscous damping coefficients using the oscillating droplet method and the level of accuracy is strongly dependent on the level of these approximations. The change in frequency due to nonlinear effects at higher amplitudes can be more significant than the shift due to the

diamagnetic forces alone. The shift in frequency is small for small size droplets. However the static deformation and therefore the frequency shift is significantly increased for larger droplets due to the non-uniformity of the energy potential.

5.9 Further Work

The study conducted in this chapter could be extended by making further investigation of the effect of the gravitational and diamagnetic forces on the oscillation frequencies and damping rates. This would include the use of both the analytical model of Hill & Eaves (2010) and the numerical model to investigate further the dependence on the shift in frequency and damping rate depending on the spatial variation of the magnetic field and field strength. The relationship between surface and translation oscillations can be highly dependent on the initial conditions and so would provide further opportunities for investigation. Also the analytical model of Hill & Eaves (2010) could be extended to include the effects of viscosity so that direct comparisons could be made with the numerical model.

6. Conducting Droplets

6.1 Overview

In this section the numerical model outlined in section 3 will be used to investigate the dynamics of a conducting droplet in a constant static magnetic field. The main objective is to use the numerical model to obtain results than can be compared qualitatively and quantitatively with the theoretical predictions of Priede (2011). The work in this section is a continuation of the study presented in Easter, Bojarevics, and Pericleous (2011a).

In §6.2 the changes to the numerical model required to incorporate the electromagnetic force are discussed. In §6.3 - §6.6 a selection of surface shape modes $Y^0_2, Y^1_2, Y^2_2, Y^0_3$ will be used as initial conditions and the results will be used to investigate the internal fluid flow, oscillation frequency and damping rate. The material chosen for the numerical test cases is silicon and the material property values are given in Table 6.1.

Symbol	Quantity	Value	Units	Reference
Γ	Surface Tension Coefficient	8.65e-1	N m ⁻¹	Brandes and Brook (1992)
ρ	Density	2.51e+3	Kg m ⁻³	
ν	Kinematic Viscosity	3.75e-7	m ² s ⁻¹	
σ	Electric Conductivity	1.30e+6	S m ⁻¹	Schnyders and Van Zytveld (1996)

Table 6.1 – Material Properties (Silicon)

The initial conditions for the numerical simulations in this section consist of a deformed surface shape and an internal velocity of zero ($\mathbf{V} = 0$). The surface shape is given by a superposition of spherical harmonic surface shapes as described in the numerical modelling section. In all numerical cases the unperturbed droplet radius is ($R_0 = 5.0$ mm) and the constant magnetic field has strength ($B_0 = 2.5$ T). The general settings used in the numerical model are outlined in §3.6.7

6.2 Numerical Model Considerations

The numerical model outlined in section 3 includes a generic body force term that will be used for the electromagnetic force:

$$\mathbf{F}_{vol} = \mathbf{J} \times \mathbf{B} \quad (6.1)$$

The electromagnetic force requires an additional equation to be solved for the electric potential. The electric current density is given by:

$$\mathbf{J} = \sigma(-\nabla\phi_E + \mathbf{V} \times \mathbf{B}) \quad (6.2)$$

The equation for the electric potential is obtained from the charge conservation condition:

$$\nabla \cdot \mathbf{J} = 0 \quad (6.3)$$

Taking the divergence of the electric current density gives:

$$\nabla^2 \phi_E = \nabla \cdot (\mathbf{V} \times \mathbf{B}) \quad (6.4)$$

This equation is solved subject to the boundary condition:

$$\mathbf{J} \cdot \mathbf{e}_n = 0 \quad (6.5)$$

The same numerical method used for the momentum equations is used to solve the equation for the electric potential. The magnetic field is a constant static field aligned with the z-axis, given in spherical coordinates by:

$$\mathbf{B}(r, \theta, \phi) = (B_0 \cos \theta, -B_0 \sin \theta, 0) \quad (6.6)$$

6.3 Oscillation Mode: $L = 2, M = 0$

The first numerical test case considered is for the axisymmetric Y_2^0 mode. The amplitude of the Y_2^0 mode corresponds to a maximum deformation of 1% of the unperturbed droplet radius. As in previous cases the Y_0^0 mode coefficient is calculated and added to the initial condition to ensure mass conservation, the full initial condition is given by the superposition of these two spherical harmonic surface shapes:

$$r_s = R_0(1 + s_0^0 Y_0^0 + s_2^0 Y_2^0) \quad (6.7)$$

The spherical harmonics follow the definition given in section 3 and can be obtained using the recurrence relations used in the numerical model:

$$Y_0^0 = N_0^0$$

$$Y_2^0 = N_2^0 \frac{1}{2}(3 \cos^2 \theta - 1) \quad (6.8)$$

Taking into account the normalisation coefficients, the surface shape coefficients for the initial condition are:

$s_0^0 N_0^0$	$s_2^0 N_2^0$
-2.00e-5	+1.00e-2
Table 6.2 – Initial Conditions, (Y_2^0)	

The Y_2^0 mode is transversal ($L - M = \text{even}$) and the theoretical analysis shows that the mode is over-damped by the magnetic field, the oscillation frequency is zero and the magnetic damping constant is given by:

$$\gamma_2^0 = 12 \frac{\sigma B_0^2 R_0^3}{\Gamma} \quad (6.9)$$

The numerical results for the surface shape function are separated into their spherical harmonic components and the dominant Y_2^0 mode coefficient is shown in Figure 6.1 along with its power spectra obtained using Prony's method (described in §3.6.6).

The theoretical value for the frequency of a freely oscillating droplet is indicated in the power spectra with a dotted line. The theoretical frequency for the conducting droplet in a static magnetic field is zero. The behaviour of the droplet has clearly changed with the introduction of the magnetic field. The oscillation is heavily damped although it does make a small oscillation before reducing to zero.

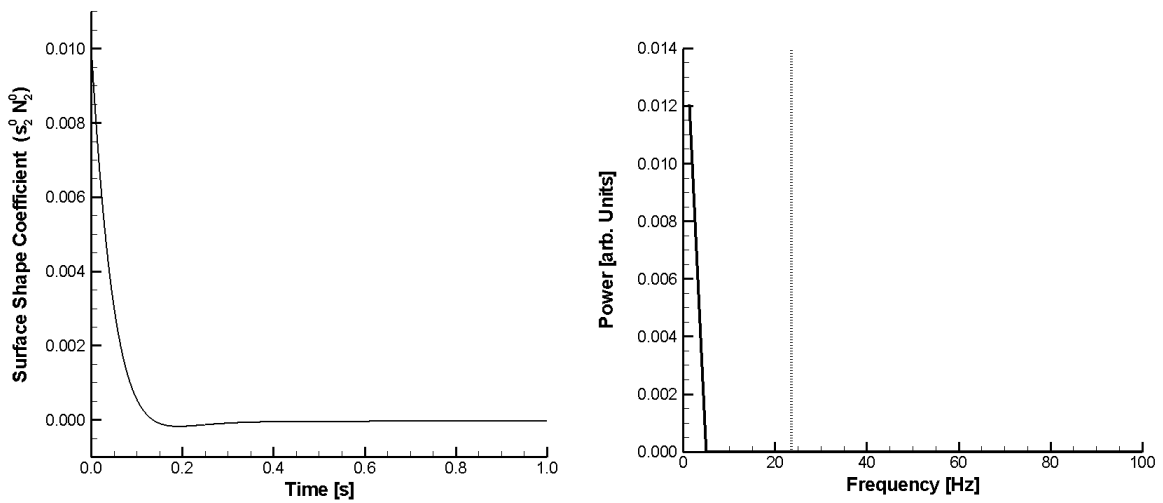


Figure 6.1 – Surface Shape Coefficient with Power Spectra, (Y_2^0)

A more quantitative comparison with the theoretical predictions can be made using further analysis of the surface shape coefficient generated by the numerical simulation. The theoretical formulae evaluated for this particular case produce the following results:

Surface Mode	Amplitude [m]	Frequency [Hz]	Viscous Damping [s^{-1}]	Magnetic Damping [s^{-1}]
Y_2^0	+1.00e-2	+0.00e+0	+0.00e+0	+1.02e+1

Table 6.3 – Theoretical Results, (Y_2^0)

Analysis of the numerical data using Prony's method produces the results given in Table 6.4. The two sets of data do not show good agreement in this case, with the numerical

results showing a small but non-zero frequency. The viscous and magnetic damping terms cannot be separated in the numerical data but the coefficient for the combined terms is much larger than the theoretical value. However no modification to the viscous damping is provided by the theoretical analysis and could explain the discrepancy.

Surface Mode	Amplitude [m]	Frequency [Hz]	Damping Coeff. [s ⁻¹]
Y_2^0	+1.21e-2	+1.37e+0	+1.93e+1
Table 6.4 – Numerical Results, (Y_2^0)			

The behaviour of the droplet in this case can be explained through observation of the flow profiles for the corresponding case for a freely oscillating droplet. The flow perpendicular to the z-axis is damped by the magnetic field leaving only flow parallel to the z-axis. Due to the symmetry of the flow in the x-y plane it is not possible to satisfy mass continuity with potential flow only in the z-direction.

6.4 Oscillation Mode: $L = 2$, $M = 1$

The next numerical test case considered is for the non-axisymmetric Y_2^1 mode. The amplitude of the Y_2^1 mode corresponds to a maximum deformation of 1% of the unperturbed droplet radius. As in previous cases the Y_0^0 mode coefficient is calculated and added to the initial condition to ensure mass conservation, the full initial condition is given by the superposition of these two spherical harmonic surface shapes:

$$r_s = R_0(1 + s_0^0 Y_0^0 + s_2^1 Y_2^1) \quad (6.10)$$

The spherical harmonics follow the definition given in section 3 and can be obtained using the recurrence relations used in the numerical model:

$$\begin{aligned} Y_0^0 &= N_0^0 \\ Y_2^1 &= -N_2^1 \sqrt{2} (3 \sin \theta \cos \theta) \cos \phi \end{aligned} \quad (6.11)$$

Taking into account the normalisation coefficients, the surface shape coefficients for the initial condition are:

$s_0^0 N_0^0$	$s_2^1 N_2^1 \sqrt{2}$
-2.67e-5	+6.67e-3
Table 6.5 – Initial Conditions, (Y_2^l)	

The Y_2^l mode is longitudinal ($L - M = \text{odd}$) and the theoretical analysis shows that the oscillation frequency and viscous damping coefficient are different from the free droplet case and are given by:

$$\omega_2^1 = 2 \sqrt{\frac{\Gamma}{\rho R_0^3}} \quad (6.12)$$

$$\gamma_2^1 = \frac{5}{2} \frac{\nu}{R_0^2} \quad (6.13)$$

There is also a magnetic damping coefficient, which is given by:

$$\gamma_2^1 = 4 \frac{\sigma B_0^2 R_0^3}{\Gamma} \quad (6.14)$$

The numerical results for the surface shape function are separated into their spherical harmonic components and the dominant Y_2^l mode coefficient is shown in Figure 6.2 along with its power spectra obtained using Prony's method (described in §3.6.6).

The theoretical values for the frequency of a freely oscillating droplet and conducting droplet in the static magnetic field are indicated in the power spectra with dotted and dashed lines respectively. There is a clear difference between the two cases, with the theoretical result for the conducting droplet showing good qualitative agreement with the numerical result.

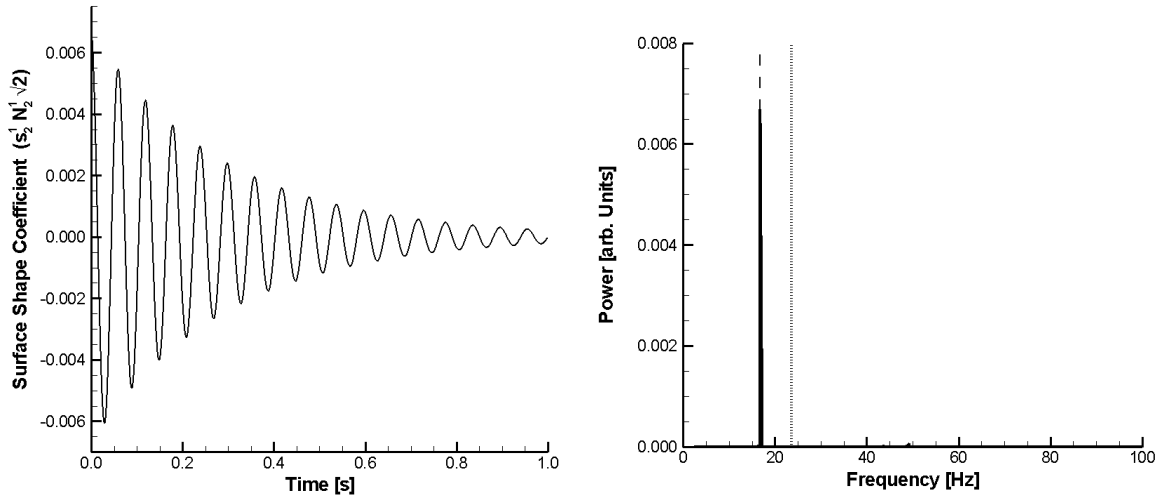


Figure 6.2 – Surface Shape Coefficient with Power Spectra, (Y^l_2)

A more quantitative comparison with the theoretical predictions can be made using further analysis of the surface shape coefficient generated by the numerical simulation. The theoretical formulae evaluated for this particular case produce the following results:

Surface Mode	Amplitude [m]	Frequency [Hz]	Viscous Damping [s^{-1}]	Magnetic Damping [s^{-1}]
Y^l_2	+6.67e-3	+1.67e+1	+3.75e-2	+3.41e+0

Table 6.6 – Theoretical Results, (Y^l_2)

Analysis of the numerical data using Prony’s method produces the results given in Table 6.7. The two sets of data show good agreement for the amplitude and frequency. The viscous and magnetic damping terms cannot be separated in the numerical data but the coefficient for the combined terms shows good agreement with the theoretical value.

Surface Mode	Amplitude [m]	Frequency [Hz]	Damping Coeff. [s^{-1}]
Y^l_2	+6.69e-3	+1.67e+1	+3.44e+0

Table 6.7 – Numerical Results, (Y^l_2)

The frequency can also be obtained from the Fourier transform and the damping coefficient using the logarithmic method (both methods described in §3.6.6). The values

obtained using these alternative approaches all give good agreement with the theoretical results.

The fluid flow for a droplet oscillating with the Y_2' mode surface shape occurs only in the x-z plane. The surface shape and fluid flow profiles are similar for any plane perpendicular to the y-axis, with magnitude depending on distance from the centre of the droplet. Figure 6.3 shows plots of the flow variables in a plane perpendicular to the y-axis in the centre of the droplet at four points in the oscillation cycle for a droplet with the given initial condition. The results presented are from a numerical simulation with a larger amplitude initial condition and an interpolated mesh is used to highlight the deformed surface shape and velocity profile. The qualitative behaviour is the same for low to moderate amplitude oscillations.

It is clear from the analysis conducted that the surface oscillation mode is unchanged by the external magnetic field. However when the internal flow is compared with the freely oscillating case there is a clear difference. The radial component of the flow is damped out and the fluid oscillates as columns along the direction of the magnetic field.

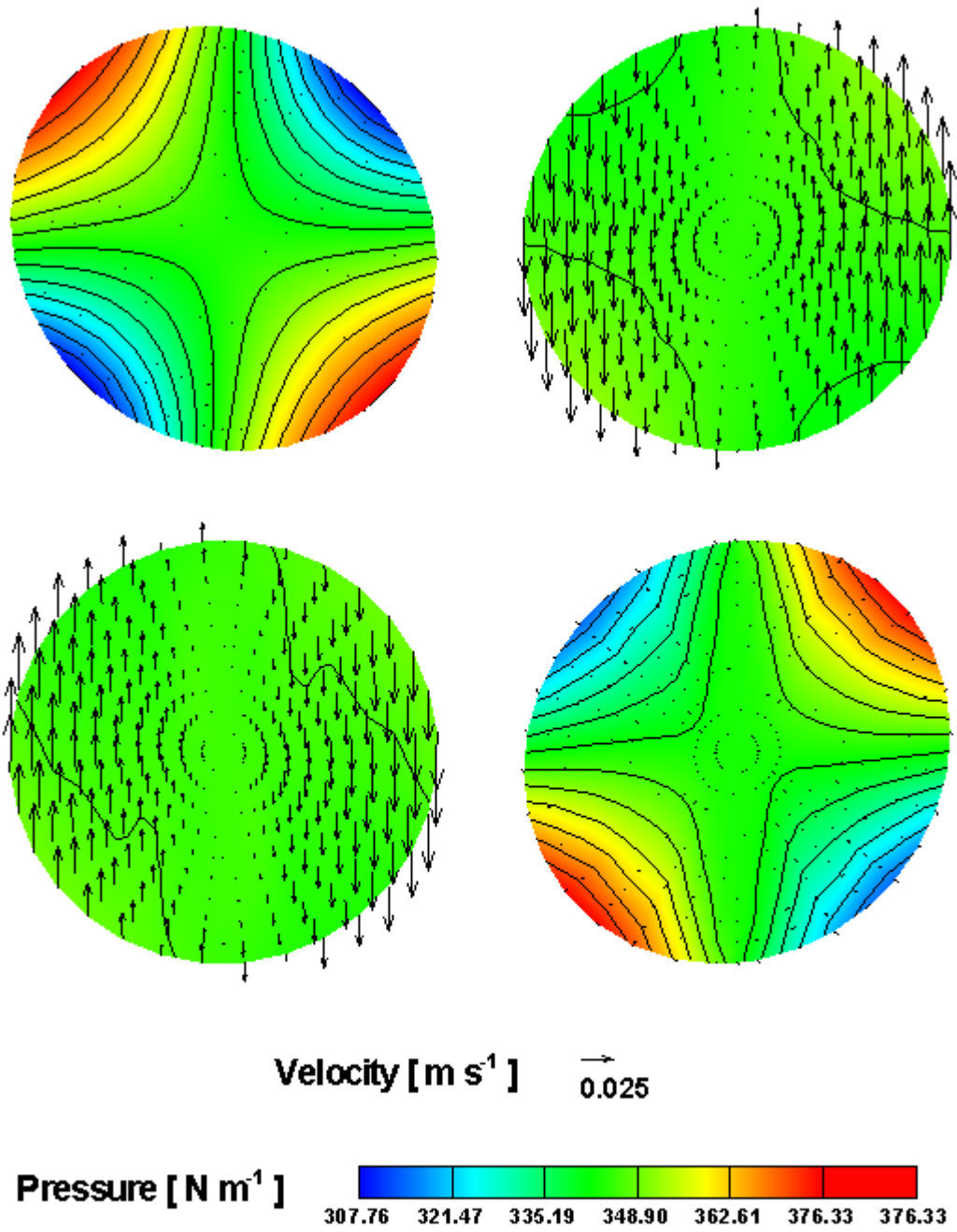


Figure 6.3 - Pressure Contour Lines and Velocity Vectors, (Y'_2)

6.5 Oscillation Mode: $L = 2, M = 2$

The next numerical test case considered is for the non-axisymmetric Y_2^2 mode. The amplitude of the Y_2^2 mode corresponds to a maximum deformation of 1% of the unperturbed droplet radius. As in previous cases the Y_0^0 mode coefficient is calculated and added to the initial condition to ensure mass conservation, the full initial condition is given by the superposition of these two spherical harmonic surface shapes:

$$r_s = R_0(1 + s_0^0 Y_0^0 + s_2^2 Y_2^2) \quad (6.15)$$

The spherical harmonics follow the definition given in section 3 and can be obtained using the recurrence relations used in the numerical model:

$$\begin{aligned} Y_0^0 &= N_0^0 \\ Y_2^2 &= N_2^2 \sqrt{2} (3 \sin^2 \theta) \cos 2\phi \end{aligned} \quad (6.16)$$

Taking into account the normalisation coefficients, the surface shape coefficients for the initial condition are:

$s_0^0 N_0^0$	$s_2^2 N_2^2 \sqrt{2}$
-2.67e-5	+3.33e-3
Table 6.8 – Initial Conditions, (Y_2^2)	

The Y_2^2 mode is transversal ($L - M = \text{even}$) and the theoretical analysis shows that the oscillation frequency and viscous damping coefficient are the same as the free droplet case and are given by:

$$\omega_2^2 = \sqrt{\frac{8 \Gamma}{\rho R_0^3}} \quad (6.17)$$

$$\gamma_2^2 = 5 \frac{\nu}{R_0^2} \quad (6.18)$$

The theoretical analysis shows that there is no magnetic damping.

The numerical results for the surface shape function are separated into their spherical harmonic components and the dominant Y_2^2 mode coefficient is shown in Figure 6.4 along with its power spectra obtained using Prony's method (described in §3.6.6). The theoretical value for the frequency of a freely oscillating droplet is indicated in the power spectra with a dashed line. There is good qualitative agreement with the numerical result, showing that the magnetic field does not affect the surface oscillation.

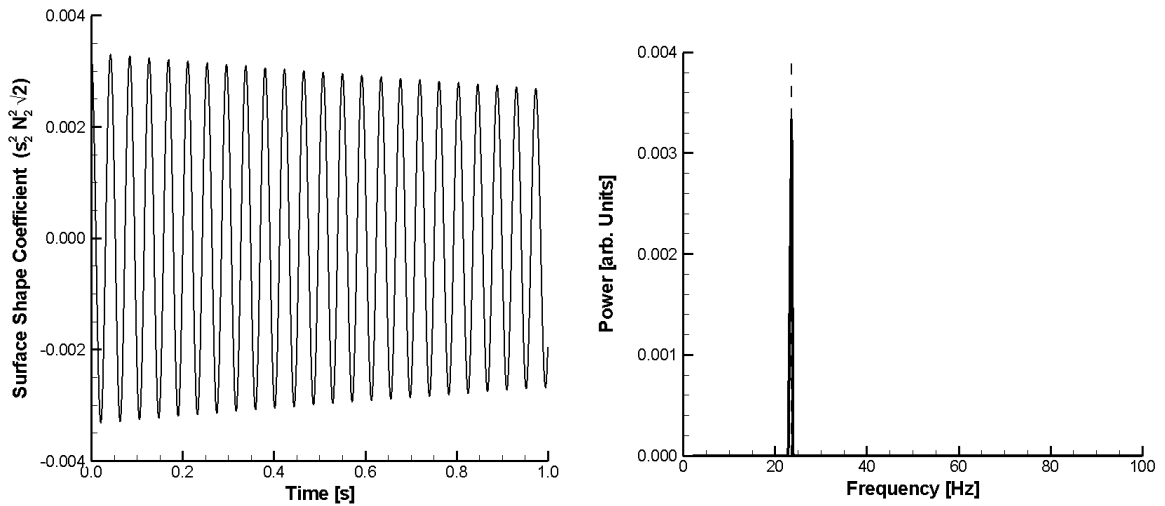


Figure 6.4 – Surface Shape Coefficient with Power Spectra, (Y_2^2)

A more quantitative comparison with the theoretical predictions can be made using further analysis of the surface shape coefficient generated by the numerical simulation. The theoretical formulae evaluated for this particular case produce the following results:

Surface Mode	Amplitude [m]	Frequency [Hz]	Viscous Damping [s^{-1}]	Magnetic Damping [s^{-1}]
Y_2^2	+3.33e-3	+2.36e+1	+7.50e-2	+0.00e+0

Table 6.9 – Theoretical Results, (Y_2^2)

Analysis of the numerical data using Prony's method produces the results given in Table 6.10. The two sets of data show good agreement for the amplitude and frequency. The viscous and magnetic damping terms cannot be separated in the numerical data but the coefficient for the combined terms is several times larger than the theoretical value.

Surface Mode	Amplitude [m]	Frequency [Hz]	Damping Coeff. [s ⁻¹]
Y_2^2	+3.34e-3	+2.36e+1	+2.19e-1
Table 6.10 – Numerical Results, (Y_2^2)			

The frequency can also be obtained from the Fourier transform and the damping coefficient using the logarithmic method (both methods described in §3.6.6). The values obtained using these alternative approaches give good agreement with the results obtained using Prony's analysis.

The reason for this behaviour can be clearly understood from the plots of the fluid flow variables for a freely oscillating droplet in §4.4. Fluid flow for this mode only occurs in the x-y plane resulting in an electric current $\sigma(\mathbf{V} \times \mathbf{B})$ perpendicular to the flow but also in the same plane. Due to the potential nature of the fluid flow, charge continuity cannot be satisfied and so an equal and opposite electric current $\sigma(-\nabla\phi_E)$ exists that results in zero net current and no damping of the flow by the electromagnetic force.

6.6 Oscillation Mode: $L = 3, M = 0$

The next numerical test case considered is for the axisymmetric Y_3^0 mode. The amplitude of the Y_3^0 mode corresponds to a maximum deformation of 1% of the unperturbed droplet radius. As in previous cases the Y_0^0 mode coefficient is calculated and added to the initial condition to ensure mass conservation, the full initial condition is given by the superposition of these two spherical harmonic surface shapes:

$$r_s = R_0(1 + s_0^0 Y_0^0 + s_3^0 Y_3^0) \quad (6.19)$$

The spherical harmonics follow the definition given in section 3 and can be obtained using the recurrence relations used in the numerical model:

$$Y_0^0 = N_0^0$$

$$Y_3^0 = N_3^0 \frac{1}{2} (5 \cos^3 \theta - 3 \cos \theta) \quad (6.20)$$

Taking into account the normalisation coefficients, the surface shape coefficients for the initial condition are:

$s_0^0 N_0^0$	$S_3^0 N_3^0$
-1.43e-5	+1.00e-2
Table 6.11 – Initial Conditions, (Y_3^0)	

The Y_3^0 mode is longitudinal ($L - M = \text{odd}$) and the theoretical analysis shows that the oscillation frequency and viscous damping coefficient are different to the free droplet case and are given by:

$$\omega_3^0 = \sqrt{\frac{10 \Gamma}{\rho R_0^3}} \quad (6.21)$$

$$\gamma_3^0 = \frac{35}{3} \frac{\nu}{R_0^2} \quad (6.22)$$

There is also a magnetic damping coefficient, which is given by:

$$\gamma_3^0 = \frac{50}{3} \frac{\sigma B_0^2 R_0^3}{\Gamma} \quad (6.23)$$

The numerical results for the surface shape function are separated into their spherical harmonic components and the dominant Y_3^0 mode coefficient is shown in Figure 6.5 along with its power spectra obtained using Prony's method (described in §3.6.6).

The theoretical values for the frequency of a freely oscillating droplet and conducting droplet in the static magnetic field are indicated in the power spectra with dotted and dashed lines respectively. There is a clear difference between the two cases, with the theoretical result for the conducting droplet showing good qualitative agreement with the numerical result.

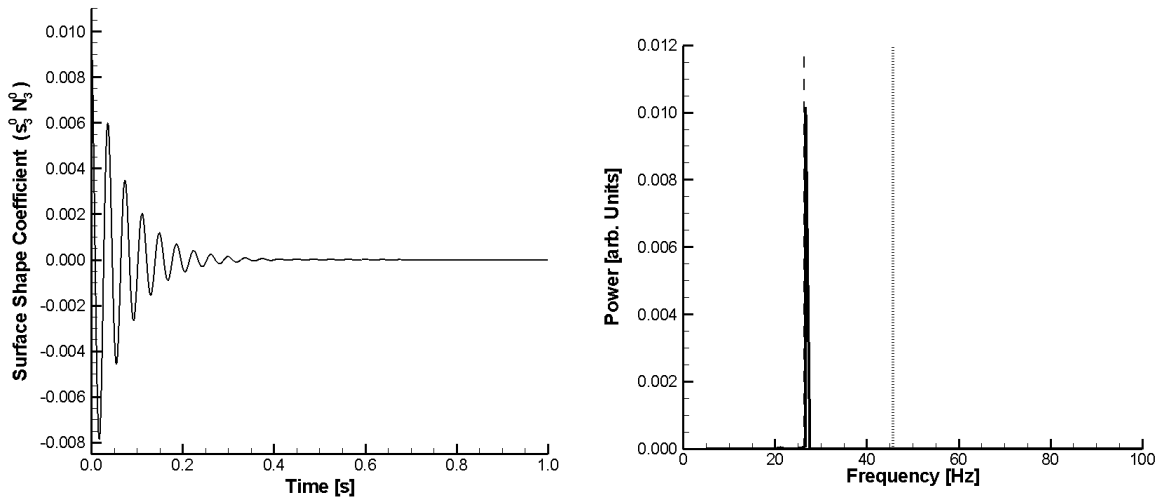


Figure 6.5 – Surface Shape Coefficient with Power Spectra, (Y_3^0)

A more quantitative comparison with the theoretical predictions can be made using further analysis of the surface shape coefficient generated by the numerical simulation. The theoretical formulae evaluated for this particular case produce the following results:

Surface Mode	Amplitude [m]	Frequency [Hz]	Viscous Damping [s ⁻¹]	Magnetic Damping [s ⁻¹]
Y_3^0	+1.00e-2	+2.64e+1	+1.75e-1	+1.42e+1
Table 6.12 – Theoretical Results, (Y_3^0)				

Analysis of the numerical data using Prony’s method produces the results given in Table 6.13. The two sets of data show good agreement for the amplitude and frequency. The viscous and magnetic damping terms cannot be separated in the numerical data but the coefficient for the combined terms shows good agreement with the theoretical value.

Surface Mode	Amplitude [m]	Frequency [Hz]	Damping Coeff. [s ⁻¹]
Y_3^0	+1.02e-2	+2.66e+1	+1.44e+1
Table 6.13 – Numerical Results, (Y_3^0)			

The frequency can also be obtained from the Fourier transform and the damping coefficient using the logarithmic method (both methods described in §3.6.6). The values obtained using these alternative approaches give reasonable agreement with the results obtained using Prony’s analysis.

The oscillation of this mode is axisymmetric and so the surface shape and fluid flow profiles are the same for any plane parallel to the z-axis. Figure 6.6 shows plots of the flow variables in a plane parallel to the z-axis in the centre of the droplet at four points in the oscillation cycle for a droplet with the given initial condition. The results presented are from a numerical simulation with a larger amplitude initial condition and an interpolated mesh is used to highlight the deformed surface shape and velocity profile. The qualitative behaviour is the same for low to moderate amplitude oscillations.

It is clear from the analysis conducted that the surface oscillation mode is unchanged by the external magnetic field. However when the internal flow is compared with the freely oscillating case there is a clear difference. The radial component of the flow is damped out and the fluid oscillates as columns along the direction of the magnetic field.

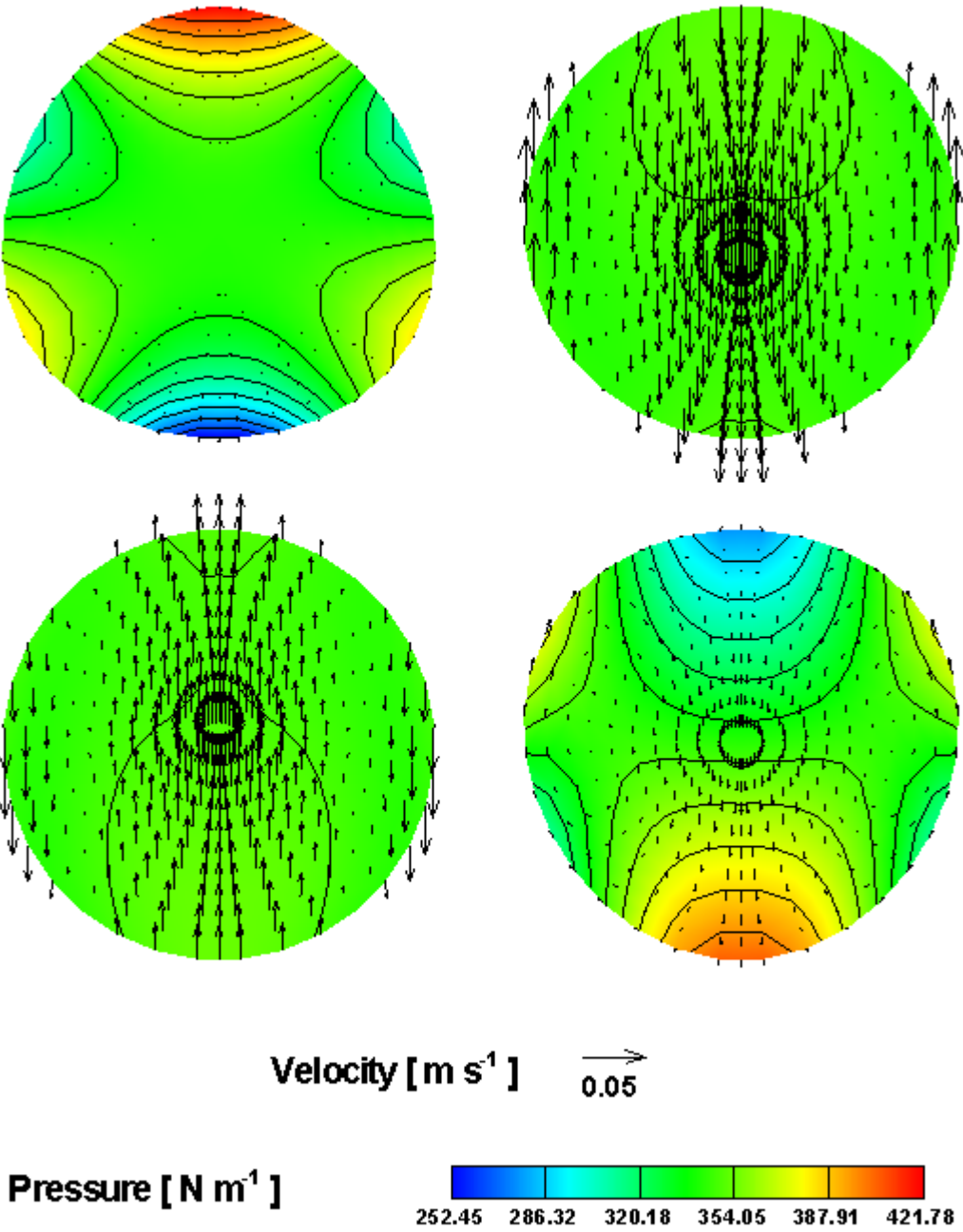


Figure 6.6 - Pressure Contour Lines and Velocity Vectors, (Y_3^0)

6.7 Summary \ Conclusions

Numerical results have been presented that confirm the theoretical results relating surface tension and viscosity to frequency and damping rates for conducting droplets in a constant magnetic field. The behaviour of a conducting droplet in a static magnetic field is strongly dependent on the internal fluid flow that results from different surface oscillation modes. In the majority of cases there is a considerable difference in internal flow, as well as surface oscillation frequency and damping rate when compared with the corresponding case for a freely oscillating droplet.

6.8 Further Work

There are a number of interesting extensions to this study that could include droplets of different sizes with different material properties and also variation in the magnitude of the static magnetic field.

The analysis of a freely oscillating droplet in section 4 highlighted that nonlinear effects are present in the droplet oscillations even at low amplitude. These nonlinear effects included mode coupling that is required to conserve the mass of the droplet and that becomes more prominent as the amplitude of oscillation increases. This presents an interesting question for conducting droplets because of the difference in behaviour of the different surface oscillation modes. For example the Y^2_2 mode is unaffected by the magnetic field, however this mode is coupled with the Y^0_2 mode at second order, which is heavily damped by the magnetic field.

The analysis in section 5 considered the application of the oscillating droplet technique to a non-conducting droplet in the magnetic field of a solenoid. It is interesting to consider the application to a conducting droplet. The magnetic field from the solenoid has a constant component but also a large gradient component that is required to balance gravity along with additional higher order spatial variation. Therefore the dynamics of a conducting droplet in the magnetic field of a solenoid is expected to be different from the cases considered so far and has no theoretical model, which can be applied to the results.

7. Research Summary and Further Work

7.1 Research Summary

A three-dimensional numerical code has been designed, implemented, and applied to a study of the dynamics of a liquid droplet oscillating in free space and in the presence of electromagnetic and gravitational forces. The numerical code uses the spectral collocation method with coordinate transformation in order to achieve the high level of accuracy required to model the free surface motion associated with the oscillating droplet technique.

In the case of a freely oscillating droplet the study of different surface mode oscillations demonstrates the accuracy of the numerical code through comparison with theoretical results and various methods of oscillation analysis provide new insight into the free surface dynamics. The three-dimensional numerical modelling of surface oscillations with a model incorporating the full Navier-Stokes equations has provided an extension to the existing axisymmetric studies that have been conducted. The results presented are beyond the limit of theoretical work available and so provide new insight into the three-dimensional dynamics of a freely oscillating droplet.

In the case of a diamagnetic droplet the study is the first of its kind to validate the theoretical model of liquid droplet oscillations in both high DC magnetic and gravitational fields. The results suggest that it is important to obtain an accurate representation of the spatial variation of the magnetic field in order to determine the modification to the oscillation frequency and damping rates.

In the case of a conducting droplet in a constant high DC magnetic field the study is the first of its kind to validate the theoretical model for this type of droplet dynamics. The magnetic field makes a considerable difference to the internal fluid flow, as well as the surface oscillation frequency and damping rates.

7.2 Further Work

There are many opportunities for further research, in addition to the suggestions made for extending each of the studies conducted, there are other opportunities which would require improvements to the accuracy and efficiency of the numerical model and extensions to include additional physical processes.

The oscillating drop technique is most commonly used in association with electrostatic and electromagnetic forces. The model could be extended to include a more detailed and accurate calculation of these forces. This would require the force at the surface to be determined by solving the electromagnetic equations subject to a far field boundary condition. In previous work that includes these forces the calculation has been achieved using numerical methods that provide less accuracy of the surface position than the coordinate transformation method. An alternative that has been applied in some cases is the method of mutual inductance, which only requires the field to be calculated within the droplet but to the best of my knowledge it has only been applied to axisymmetric cases and would need expanding to a full three-dimensional formulation.

Extending the model to study interaction with a surrounding fluid is also possible; however the most straightforward method of achieving this would be a finite-element model for the surrounding fluid, which would again have an impact on the accuracy of the surface oscillations.

The coordinate transformation method currently prevents the study of rotating droplets due to deformation of the mesh; however it is possible to modify the equations modelled to include the effects of uniform rotation. Also the model is currently limited to small amplitude translation oscillations because the coordinate transformation used results in mesh deformation with translation. This could be overcome by separating the translation motion from the internal fluid motion.

The variation in surface tension with temperature results in Marangoni flow effects, which could be studied with the introduction of the energy equation to the numerical model.

The presence of surfactants is known to seriously affect the surface tension of a material and also the damping of the surface oscillations.

The present study has been restricted to laminar flow, but with the inclusion of a turbulence model(s) the transition from the laminar to turbulence regimes could be studied.

There is a large amount of theoretical work available but there are also many unexplored areas. The link to experimental results would benefit most from theoretical work that provides clear formulae and the limits of their application.

Appendix A – Derivative Operators

A.1 Coordinate Transformation

$$\bar{r} = \frac{r}{R_0 [1 + S(\theta, \phi, t)]} \quad \bar{\theta} = \theta \quad \bar{\phi} = \phi \quad \bar{t} = t \quad (\text{A.1})$$

A.2 First Radial Derivative

$$\frac{\partial}{\partial r} = \frac{\partial \bar{r}}{\partial r} \frac{\partial}{\partial \bar{r}} + \frac{\partial \bar{\theta}}{\partial r} \frac{\partial}{\partial \bar{\theta}} + \frac{\partial \bar{\phi}}{\partial r} \frac{\partial}{\partial \bar{\phi}} + \frac{\partial \bar{t}}{\partial r} \frac{\partial}{\partial \bar{t}} \quad (\text{A.2})$$

$$\frac{\partial \bar{r}}{\partial r} = \frac{1}{R_0 (1 + S)} \quad \frac{\partial \bar{\theta}}{\partial r} = 0 \quad \frac{\partial \bar{\phi}}{\partial r} = 0 \quad \frac{\partial \bar{t}}{\partial r} = 0 \quad (\text{A.3})$$

$$\frac{\partial}{\partial r} = \frac{1}{R_0 (1 + S)} \frac{\partial}{\partial \bar{r}} \quad (\text{A.4})$$

A.3 First Theta Derivative

$$\frac{\partial}{\partial \theta} = \frac{\partial \bar{r}}{\partial \theta} \frac{\partial}{\partial \bar{r}} + \frac{\partial \bar{\theta}}{\partial \theta} \frac{\partial}{\partial \bar{\theta}} + \frac{\partial \bar{\phi}}{\partial \theta} \frac{\partial}{\partial \bar{\phi}} + \frac{\partial \bar{t}}{\partial \theta} \frac{\partial}{\partial \bar{t}} \quad (\text{A.5})$$

$$\frac{\partial \bar{r}}{\partial \theta} = -\frac{r}{R_0 (1 + S)^2} \frac{\partial S}{\partial \bar{\theta}} \quad \frac{\partial \bar{\theta}}{\partial \theta} = 1 \quad \frac{\partial \bar{\phi}}{\partial \theta} = 0 \quad \frac{\partial \bar{t}}{\partial \theta} = 0 \quad (\text{A.6})$$

$$\frac{\partial}{\partial \theta} = \frac{\partial}{\partial \bar{\theta}} - \frac{\bar{r}}{(1 + S)} \frac{\partial S}{\partial \bar{\theta}} \frac{\partial}{\partial \bar{r}} \quad (\text{A.7})$$

A.4 First Phi Derivative

$$\frac{\partial}{\partial \phi} = \frac{\partial \bar{r}}{\partial \phi} \frac{\partial}{\partial \bar{r}} + \frac{\partial \bar{\theta}}{\partial \phi} \frac{\partial}{\partial \bar{\theta}} + \frac{\partial \bar{\phi}}{\partial \phi} \frac{\partial}{\partial \bar{\phi}} + \frac{\partial \bar{t}}{\partial \phi} \frac{\partial}{\partial \bar{t}} \quad (\text{A.8})$$

$$\frac{\partial \bar{r}}{\partial \phi} = -\frac{r}{R_0 (1 + S)^2} \frac{\partial S}{\partial \bar{\phi}} \quad \frac{\partial \bar{\theta}}{\partial \phi} = 0 \quad \frac{\partial \bar{\phi}}{\partial \phi} = 1 \quad \frac{\partial \bar{t}}{\partial \phi} = 0 \quad (\text{A.9})$$

$$\frac{\partial}{\partial \phi} = \frac{\partial}{\partial \bar{\phi}} - \frac{\bar{r}}{(1+S)} \frac{\partial S}{\partial \bar{\phi}} \frac{\partial}{\partial \bar{r}} \quad (\text{A.10})$$

A.5 First Time Derivative

$$\frac{\partial}{\partial t} = \frac{\partial \bar{r}}{\partial t} \frac{\partial}{\partial \bar{r}} + \frac{\partial \bar{\theta}}{\partial t} \frac{\partial}{\partial \bar{\theta}} + \frac{\partial \bar{\phi}}{\partial t} \frac{\partial}{\partial \bar{\phi}} + \frac{\partial \bar{t}}{\partial t} \frac{\partial}{\partial \bar{t}} \quad (\text{A.11})$$

$$\frac{\partial \bar{r}}{\partial t} = -\frac{r}{R_0 (1+S)^2} \frac{\partial S}{\partial \bar{t}} \quad \frac{\partial \bar{\theta}}{\partial t} = 0 \quad \frac{\partial \bar{\phi}}{\partial t} = 0 \quad \frac{\partial \bar{t}}{\partial t} = 1 \quad (\text{A.12})$$

$$\frac{\partial}{\partial t} = \frac{\partial}{\partial \bar{t}} - \frac{\bar{r}}{(1+S)} \frac{\partial S}{\partial \bar{t}} \frac{\partial}{\partial \bar{r}} \quad (\text{A.13})$$

A.6 Second Radial Derivative

$$\frac{\partial^2}{\partial r^2} = \frac{\partial}{\partial r} \left(\frac{\partial}{\partial r} \right) = \frac{1}{R_0^2 (1+S)^2} \frac{\partial^2}{\partial \bar{r}^2} \quad (\text{A.14})$$

A.7 Second Theta Derivative

$$\frac{\partial^2}{\partial \theta^2} = \frac{\partial}{\partial \theta} \left(\frac{\partial}{\partial \theta} \right) = \frac{\partial}{\partial \bar{\theta}} - \frac{\bar{r}}{(1+S)} \frac{\partial S}{\partial \bar{\theta}} \frac{\partial}{\partial \bar{r}} \left(\frac{\partial}{\partial \bar{\theta}} - \frac{\bar{r}}{(1+S)} \frac{\partial S}{\partial \bar{\theta}} \frac{\partial}{\partial \bar{r}} \right) \quad (\text{A.15})$$

$$\begin{aligned} \frac{\partial^2}{\partial \theta^2} &= \frac{\partial^2}{\partial \bar{\theta}^2} + \left(-\frac{\bar{r}}{(1+S)} \frac{\partial^2 S}{\partial \bar{\theta}^2} \frac{\partial}{\partial \bar{r}} \right) + \left(-\frac{\bar{r}}{(1+S)} \frac{\partial S}{\partial \bar{\theta}} \frac{\partial}{\partial \bar{r}} \frac{\partial}{\partial \bar{\theta}} \right) \\ &\quad + \left(\frac{\bar{r}}{(1+S)^2} \left(\frac{\partial S}{\partial \bar{\theta}} \right)^2 \frac{\partial}{\partial \bar{r}} \right) - \frac{\bar{r}}{(1+S)} \frac{\partial S}{\partial \bar{\theta}} \frac{\partial}{\partial \bar{r}} \frac{\partial}{\partial \bar{\theta}} \\ &\quad + \left(\frac{1}{(1+S)} \frac{\partial S}{\partial \bar{\theta}} \right)^2 \left(\frac{\partial}{\partial \bar{r}} + \bar{r} \frac{\partial^2}{\partial \bar{r}^2} \right) \end{aligned} \quad (\text{A.16})$$

A.8 Second Phi Derivative

$$\frac{\partial^2}{\partial \phi^2} = \frac{\partial}{\partial \phi} \left(\frac{\partial}{\partial \phi} \right) = \frac{\partial}{\partial \bar{\phi}} - \frac{\bar{r}}{(1+S)} \frac{\partial S}{\partial \bar{\phi}} \frac{\partial}{\partial \bar{r}} \left(\frac{\partial}{\partial \bar{\phi}} - \frac{\bar{r}}{(1+S)} \frac{\partial S}{\partial \bar{\phi}} \frac{\partial}{\partial \bar{r}} \right) \quad (\text{A.17})$$

$$\begin{aligned}
\frac{\partial^2}{\partial \phi^2} &= \frac{\partial^2}{\partial \bar{\phi}^2} + \left(-\frac{\bar{r}}{(1+S)} \frac{\partial^2 S}{\partial \bar{\phi}^2} \frac{\partial}{\partial \bar{r}} \right) + \left(-\frac{\bar{r}}{(1+S)} \frac{\partial S}{\partial \bar{\phi}} \frac{\partial}{\partial \bar{r}} \frac{\partial}{\partial \bar{\phi}} \right) \\
&\quad + \left(\frac{\bar{r}}{(1+S)^2} \left(\frac{\partial S}{\partial \bar{\phi}} \right)^2 \frac{\partial}{\partial \bar{r}} \right) - \frac{\bar{r}}{(1+S)} \frac{\partial S}{\partial \bar{\phi}} \frac{\partial}{\partial \bar{r}} \frac{\partial}{\partial \bar{\phi}} \\
&\quad + \left(\frac{1}{(1+S)} \frac{\partial S}{\partial \bar{\phi}} \right)^2 \left(\frac{\partial}{\partial \bar{r}} + \bar{r} \frac{\partial^2}{\partial \bar{r}^2} \right)
\end{aligned} \tag{A.18}$$

Appendix B – Preconditioned Bi-Conjugate Gradient Stabilised Method

The 'Preconditioned Bi-Conjugate Gradient Stabilised Method' is a generic routine for solving the matrix vector problem ($A*x = b$) and is used in the numerical model to solve individually the momentum equation for each of the velocity components and the Poisson equation for pressure. The algorithm is summarised here and further details can be found in Kopriva (2009). The algorithm is formed mainly of elementary operations including the dot product of two vectors $\langle a, b \rangle$. The input parameters are the vector b and the LU decomposition of the finite difference pre-conditioner matrix, which is used in steps 5.4 and 5.8 (represented in the algorithm by K^{-1}). Steps 1, 5.5, and 5.9 include the multiplication of the spectral derivatives matrix representing the momentum or Poisson equation with the solution vector (velocity component or pressure), which is carried out by a number of subroutines.

- 1 $r_0 = b - A x_0$
- 2 $\hat{r}_0 = r_0$
- 3 $\rho_0 = \alpha = \omega_0 = 1$
- 4 $v_0 = p_0 = 0$
- 5 For $i = 1, 2, 3$
 - 5.1 $\rho_i = \langle \hat{r}_i, r_{i-1} \rangle$
 - 5.2 $\beta = \frac{\rho_i}{\rho_{i-1}} \frac{\alpha}{\omega_{i-1}}$
 - 5.3 $p_i = r_{i-1} + \beta(p_{i-1} - \omega_{i-1} v_{i-1})$
 - 5.4 $y = K^{-1} p_i$ {Pre-conditioner Step}
 - 5.5 $v_i = A y$
 - 5.6 $\alpha = \frac{\rho_i}{\langle \hat{r}_0, v_i \rangle}$
 - 5.7 $s = r_{i-1} - \alpha v_i$

$$5.8 \quad z = K^{-1} s \quad \{\text{Pre-conditioner Step}\}$$

$$5.9 \quad t = A z$$

$$5.10 \quad \omega_i = \frac{\langle t, s \rangle}{\langle t, t \rangle}$$

$$5.11 \quad x_i = x_{i-1} + \alpha y + \omega_i z$$

5.12 If x_i is accurate enough then quit

$$5.13 \quad r_i = s - \omega_i t$$

Appendix C – Publications Produced by this Research

- Bojarevics V, Easter S, Roy A and Pericleous K 2009 “Magnetic Damping of Levitated Liquid Droplets in AC and DC Field” *Proceedings of the 6th International Conference on the Electromagnetic Processing of Materials* 699-702.
- Bojarevics V, Easter S and Pericleous K 2009 “Levitated Liquid Droplets in AC and DC Magnetic Field” *Proceedings of the International Symposium on Liquid Metal Processing and Casting* 319-326.
- Bojarevics V, Easter S and Pericleous K 2010 “Direct current magnetic levitation of a liquid droplet: numerical solutions” *Proceedings of the Seventh International Conference on Engineering Computational Technology* 1-10
- Bojarevics V, Easter S and Pericleous K 2012 “Liquid droplet dynamics in gravity compensating high magnetic field” Accepted for presentation at ‘The Minerals, Metals & Materials Society (TMS) Annual Meeting & Exhibition 2012’
- Easter S, Bojarevics V and Pericleous K 2009 “Determining Surface Tension Using DC Magnetic Levitation” *Proceedings of the 6th International Conference on the Electromagnetic Processing of Materials* 723-726
- Easter S, Bojarevics V and Pericleous K 2011a “Numerical Modelling of Liquid Droplet Dynamics in Microgravity” *J. Phys.: Conf. Ser (International Symposium on Physical Sciences in Space)*. **327** (1) 012027
- Easter S, Bojarevics V and Pericleous K 2011b “3D Numerical Modelling of Liquid Droplet Dynamics in a High DC Magnetic Field” *Proceedings of the 8th International PAMIR Conference on Fundamental and Applied MHD* 927-931
- Roy A A, Easter S, Bojarevics V and Pericleous K 2011 “Use of a Static Magnetic Field in Measuring the Thermal Conductivity of a Levitated Molten Droplet” *Journal of Algorithms and Computational Technology* **6** (1) 37-49

References

- Abe Y, Hyuga D, Yamada S, and Aoki K 2006 “Study on internal flow and surface deformation of large droplet levitated by ultrasonic wave” *Ann. N.Y. Acad. Sci.* **1077** 49-62
- Adachi M, Aoyagi T, Mizuno A, Watanabe M, Kobatake H and Fukuyama H 2008 “Precise density measurements for electromagnetically levitated liquid combined with surface oscillation analysis” *Int. J. Thermophys.* **29** 2006-2014
- Adornato P M and Brown R A 1983 “Shape and stability of electro-statically levitated drops” *Proc. R. Soc. Lond. A* **389** 101-117
- Alonso C T 1974 “The dynamics of colliding and oscillating drops” *Proc. Intern. Colloq. on Drops & Bubbles* 139-157
- Azuma H and Yoshihara S 1999 “Three dimensional large amplitude drop oscillations: experiments and theoretical analysis” *J. Fluid Mech.* **393** 309-332
- Bardet B, Bojarevics V, Pericleous K and Etay J 2006 “Numerical simulation of free surface behaviour of a molten liquid metal Droplet with and without electromagnetic induction” *Pro. 5th Int. Symp. Electromagnetic Proc. Mat.* 306-310
- Basaran O A 1992 “Nonlinear oscillations of viscous liquid drops” *J. Fluid Mech.* **241** 169-198
- Batchelor G K 1967 An Introduction to Fluid Dynamics Cambridge University Press, England
- Beaugnon E and Tournier R 1991a “Levitation of organic materials” *Nature* **349** 470
- Beaugnon E and Tournier R 1991b “Levitation of water and organic substances in high static magnetic fields” *J. Phys. III France* **1** 1423-1428
- Beaugnon E, Bourgault D, Braithwaite D, de Rango P, Perrier de la Bathie R, Sulpice A and Tournier R 1993 “Material processing in high static magnetic field. A review of an experimental study on levitation, phase separation, convection and texturation” *J. Phys. I France* **3** 399-421
- Beaugnon E, Fabregue D, Billy D, Nappa J and Tournier R 2001 “Dynamics of magnetically levitated droplets” *Physica B* **294-295** 715-720

- Becker E, Hiller W J and Kowalewski T A 1991 “Experimental and theoretical investigation of large-amplitude oscillations of liquid droplets” *J. Fluid Mech.* **231** 189-210
- Becker E, Hiller W J and Kowalewski T A 1994a, “Nonlinear dynamics of viscous droplets” *J. Fluid Mech.* **258** 191-216
- Becker E, Brosa U and Kowalewski T A 1994b “Reduction of nonlinear dynamic systems by phase space analysis” *Comp. Assisted Mech. Eng. Sci.* **1** (1/2) 39-48
- Berry M V and Geim A K 1997 “Of flying frogs and levitrons” *Eur. J. Phys.* **18** 307-313
- Berry S R, Hyers R W, Racz L M and Abedian B 2005 “Surface oscillations of an electromagnetically levitated droplet” *Int. J. Thermophys.* **26** (5) 1565-1581
- Bojarevics V and Pericleous K 2003 “Modelling electromagnetically levitated liquid droplet oscillations” *ISIJ Int.* **43** (6) 890-898
- Bojarevics V and Pericleous K 2007a “Liquid metal induction heating modelling for cold crucible applications” *Int. J. Materials and Product Technology* **29** (1-4) 70-83
- Bojarevics V and Pericleous K 2007b Chapter “Numerical modelling for electromagnetic processing of materials” In: Molokov S, Moreau R and Moffatt H K Magnetohydrodynamics Springer, England 357-374
- Bojarevics V and Pericleous K 2009a “Droplet oscillations in high gradient static magnetic field” *Microgravity Sci. Technol.* **21** 119-122
- Bojarevics V and Pericleous K 2009b “Levitated droplet oscillations: effect of internal flow” *Magnetohydrodynamics* **45** (3) 267-276
- Boyd J P 2000 Chebyshev and Fourier Spectral Methods 2nd Edition, Dover Publications, USA
- Brandes E A and Brook G B 1992 Smithells Metals Reference Book Seventh Edition, Butterworth-Heinemann, England
- Bratz A and Egry I 1995 “Surface oscillations of electromagnetically levitated viscous metal droplets” *J. Fluid Mech.* **298** 341-359
- Braunbeck W 1939 “Free suspension of bodies in electric and magnetic fields” *Zeitschrift für Physik* **112** 753-763
- Brillo J and Egry I 2007 “Density and surface tension of electromagnetically levitated Cu-Co-Fe alloys” *Int. J. Thermophys.* **28** (3) 1004-1016

- Brooks R F and Day A P 1999 “Observations of the effects of oxide skins on the oscillations of electromagnetically levitated metal droplets” *Int. J. Thermophys.* **20** (4) 1041-1050
- Brooks R F, Dinsdale A T and Queded P N 2005 “The measurement of viscosity of alloys - a review of methods, data and models” *Meas. Sci. Technol.* **16** 354-362
- Brooks R F and Queded P N 2005 “The surface tension of steels” *J. Mater. Sci.* **40** 2233-2238
- Busse F H 1984 “Oscillations of a rotating liquid drop” *J. Fluid Mech.* **142** 1-8
- Canuto C, Hussaini M Y, Quarteroni A and Zang T A 2007 Spectral Methods, Evolution to Complex Geometries and Applications to Fluid Dynamics Springer, Germany
- Chapelle P, Jardy A, Ablitzer D, Pomarin Yu M and Grigorenko G M 2008 "High-speed imaging and CFD simulations of a deforming liquid metal droplet in an electromagnetic levitation experiment" *J. Mater. Sci.* **43** (9) 3001-3008
- Chandrasekhar S 1959 “The oscillations of a viscous liquid globe” *Proc. London Math. Soc.* **3-9** (1) 141-149
- Chandrasekhar S 1981 Hydrodynamic and hydromagnetic stability Dover Publications, England
- Chen S F and Overfelt R A 1988 “Effects of sample size on surface-tension measurements of nickel in reduced-gravity parabolic flights” *Int. J. Thermophys.* **19** (3) 817-826
- Cummings D L and Blackburn D A 1991 “Oscillations of magnetically levitated aspherical droplets” *J. Fluid Mech.* **224** 395-416
- Earnshaw S 1842 “On the nature of the molecular forces which regulate the constitution of the luminiferous ether” *Trans. Camb. Phil. Soc.* **7** 97-112
- Egry I, Lohoefer G, Jacobs G 1995 “Surface tension of liquid metals results from measurements on ground and in space” *Phys. Rev. Lett.* **75** (22) 4043-4046
- Egry I, Langen M and Lohoefer G 1998a “Measurements of thermophysical properties of liquid metals relevant to marangoni effects” *Phil. Trans. R. Soc. Lond. A* **356** 845-856
- Egry I, Schwartz E, Szekely J, Jacobs G, Lohoefer G and Neuhaus P 1998b “Surface tension measurements on liquid metals in microgravity” *Metall. Mater. Trans. B* **29B** 1031-1035
- Egry I, Lohoefer G, Seyhan I, Schneider S and Feuerbacher B 1999 “Viscosity and surface tension measurements in microgravity” *Int. J. Thermophys.* **20** (4) 1005-1015

- Egry I, Diefenbach A, Dreier W and Piller J 2001 “Containerless processing in space - thermophysical property measurements using electromagnetic levitation” *Int. J. Thermophys.* **22** (2) 569-578
- Egry I, Giffard H and Schneider S 2005a “The oscillating drop technique revisited” *Meas. Sci. Technol.* **16** 426-431
- Egry I 2005b “The oscillation spectrum of a compound drop” *J. Mater. Sci.* **40** 2239-2243
- Faraday M 1846 Experimental “Researches in Electricity Twentieth Series” *Phil. Trans. R. Soc. Lond.* **136** 21-40
- Faraday M 1855 Experimental Researches in Electricity Volume III, London
- Foote G B 1973 “A numerical method for studying liquid drop behaviour: simple oscillation” *J. Comput. Phys.* **11** 507-530
- Fornberg B 1996 A Practical Guide to Pseudospectral Methods Cambridge University Press, England
- Fujii H, Matsumoto T and Nogi K 2000a “Analysis of surface oscillation of droplet under microgravity for the determination of its surface tension” *Acta Mater.* **48** 2933-2939
- Fujii H, Matsumoto T, Hata N, Nakano T, Kohno M and Nogi K 2000b “Surface tension of molten silicon measured by the electromagnetic levitation method under microgravity” *Metall. Mater. Trans. A* **31A** 1585-1589
- Geim A 1998 “Everyone's magnetism” *Physics Today*
- Happel J and Brenner H 1965 Low Reynolds Number Hydrodynamics Prentice-Hall, USA
- Hauer J F, Demeure C J and Scharf L L 1990 “Initial results in Prony analysis of power system response signals” *IEEE Trans. Power Systems* **5** (1) 80-89
- Hill R J A and Eaves L 2010 “Vibrations of a diamagnetically levitated water droplet” *Phys. Rev E* **81** (5) 056312
- Hiller W J and Kowalewski T A 1989 “Surface tension measurements by the oscillating droplet method” *Phys. Chem. Hydrodyn.* **11** 103-112
- Hughes W F, Brighton J A and Winowich N 1999 Schaum's Outline of Fluid Dynamics (Schaum's Outline Series) McGraw Hill, USA
- Kopriva D A 2009 Implementing Spectral Methods for Partial Differential Equations Springer, Germany
- Kowalewski T A and Bruhn D 1994 “Nonlinear oscillations of viscous droplets” *Japan-Central Europe Joint Workshop on Adv. Comp. in Eng.*

- Lamb H 1881 “On the oscillations of a viscous spheroid” *Proc. Lond. Math. Soc.* **1-13** (1) 51-66
- Lamb H 1975 Hydrodynamics 6th Edition Cambridge University Press, England
- Landau L D and Lifshitz E M 1987 Fluid Mechanics 2nd Edition Pergamon Press, England
- Li B Q 2006 “Effect of convection on the measurement of thermophysical properties using levitated droplets” *Ann. N.Y. Acad. Sci.* **1077** 1-32
- Lundgren T S and Mansour N A 1988 “Oscillations of drops in zero gravity with weak viscous effects” *J. Fluid Mech.* **194** 479-510
- Matsumoto T, Fujii H, Ueda T, Kamai M and Nogi K 2005 “Measurement of surface tension of molten copper using the free-fall oscillating drop method” *Meas. Sci. Technol.* **16** 432-437
- Meradji S, Lyubimova T P, Lyubimov D V, and Roux B 2001 “Numerical simulation of a liquid droplet freely oscillating” *Cryst. Res. Technol.* **36** (7) 729-744
- Millot F, Rifflet J C, Wille G, Sarou-Kanian V and Glorieux B 2002 “Analysis of surface tension from aerodynamic levitation of liquids” *J. Am. Ceram. Soc.* **85** (1) 187-192
- Natarajan R and Brown R A 1986 “Quadratic resonance in the three-dimensional oscillations of inviscid drops with surface tension” *Phys. Fluids* **29** (9) 2788-2797
- Natarajan R and Brown R A 1987 “Third-order resonance effect and the nonlinear stability of drop oscillations” *J. Fluid Mech.* **183** 95-121
- Paradis 2005 “Electrostatic levitation research & development at JAXA past & present activities in thermophysics” *Int. J. Thermophys.* **26** (4) 1031-1049
- Patzek T W, Benner R E, Basaran O A and Scriven L E 1991 “Nonlinear oscillations of inviscid free drops” *J. Comput. Phys.* **97** 489-515
- Pericleous K and Bojarevics V 2007 “Pseudo-spectral solutions for fluid flow and heat transfer in electro-metallurgical applications” *Progress in Computational Fluid Dynamics* **7** (2-4) 118-127
- Pozrikidis C 2001 “Three-dimensional oscillations of inviscid drops induced by surface tension” *Comput. Fluids* **30** 417-444
- Press W H, Teukolsky S A, Vetterling W T and Flannery B P 2007 Numerical Recipes 3rd Edition Cambridge University Press, England
- Priede J 2011 “Oscillations of weakly viscous conducting liquid drops in a strong magnetic field” *J. Fluid Mech.* **671** 399-416

- Prosperetti A 1980 “Free oscillations of drops and bubbles the initial-value problem” *J. Fluid Mech.* **100** (2) 333-347
- Rayleigh 1879 “On the capillary phenomena of jets” *Proc. R. Soc. Lond. A* **29** 71-97
- Rayleigh 1882 “On the equilibrium of liquid conducting masses charged with electricity” *Philosophical Magazine Series 5* **14** (87) 184-186
- Reid W H 1960 “The oscillations of a viscous liquid drop” *Q. Appl. Math.* **18** 86-89
- Rhim W K, Chung S K, Hyson M T, Trinh E H, and Elleman D D 1987 “Large charged drop levitation against gravity” *IEEE Trans. Ind. Appl.* **IA-23** (6) 975-979
- Rhim W K, Ohsaka K, and Paradis P F 1999 “Noncontact technique for measuring surface tension and viscosity of molten materials using high temperature electrostatic levitation” *Rev. Sci. Instrum.* **70** (6) 2796-2801
- Geim A 1997 “Molecular magnetism takes off” *Physics World*
- Schetelat P, Bojarevics V, Pericleous K, and Etay J 2007 “Basic principles of non-contact thermo-physical property measurements in reduced gravity using inductive levitation” *Proc. Biennial Int. Symp. Eur. Low Gravity Res. Assoc. (ELGRA)*
- Schnyders H S and Van Zytveld J B 1996 “Electrical resistivity and thermopower of liquid Ge and Si” *J. Phys.: Condens. Matter.* **8** 10875-10883
- Schwartz E M 1995 “Measurement of the surface tension of electromagnetically-levitated droplets in microgravity” PhD Thesis Massachusetts Institute of Technology, USA
- Simon M D and Geim A K 2000 “Diamagnetic levitation: flying frogs and floating magnets (invited)” *J. Appl. Phys.* **87** (9) 6200-6204
- Smythe W R 1950 Static and Dynamic Electricity, McGraw-Hill, London
- Stein A, Rutten M, and Wunsch O 2009 “Numerical investigation of laminar fluid flow in an oscillating sphere” *PAMM Proc. Appl. Math. Mech.* **9** 487-488
- Stuckrad B, Hiller W J, and Kowalewski T A 1993 “Measurement of dynamic surface tension by the oscillating droplet method” *Exp. Fluids* **15** 332-340
- Suryanarayana P V R and Bayazitoglu Y 1991 “Effect of static deformation and external forces on the oscillations of levitated droplets” *Phys. Fluids A* **3** (5) 967-977
- Tang H H K and Wong C Y 1974 “Vibration of a viscous liquid sphere” *J. Phys. A: Math. Gen* **7** (9) 1038-1050
- Thomson W 1863a “On the rigidity of the earth” *Phil. Trans. R. Soc. Lond.* 153 573-582
- Thomson W 1863b “Dynamical problems regarding elastic spheroidal shells and spheroids of incompressible liquid” *Phil. Trans. R. Soc. Lond.* **153** 583-616

- Thomson W 1890 Mathematical and Physical Papers Volume III, Elasticity, Heat, Electro-Magnetism, Cambridge University Press, Cambridge
- Trefethen L N 2000 Spectral Methods in Matlab Society for Industrial and Applied Mathematics (SIAM), USA
- Trinh E and Wang T G 1982 “Large-amplitude free and driven drop-shape oscillations: experimental observations” *J. Fluid Mech.* **122** 315-338
- Trinh E, Thiessen D B, and Hold R G 1998 “Driven and freely decaying nonlinear shape oscillations of drops and bubbles immersed in a liquid: experimental results” *J. Fluid Mech.* **364** 253-272
- Tsamopoulos J A and Brown R A 1983 “Nonlinear oscillations of inviscid drops and bubbles” *J. Fluid Mech.* **127** 519-537
- Wang T G, Anilikumar A V, and Lee C P 1996 “Oscillations of liquid drops: results from USML-1 experiments in Space” *J. Fluid Mech.* **308** 1-14
- Watanabe T 2006 “Oscillation and rotation of levitated liquid droplet” *European Conference on Computational Fluid Dynamics ECCOMAS*
- Watanabe T 2008 “Numerical simulation of oscillations and rotations of a free liquid droplet using the level set method” *Comput. Fluids* **37** 91-98
- Watanabe T 2009 “Frequency shift and aspect ratio of a rotating-oscillating liquid droplet” *Phys. Lett. A* **373** 867-870
- Weilert M A, Whitaker D L, Maris H J and Seidel G M 1996 “Magnetic levitation and noncoalescence of liquid helium” *Phys. Rev. Lett.* **77** (23) 4840-4843
- Weilert M A, Whitaker D L, Maris H J and Seidel G M 1997 “Magnetic levitation of liquid helium” *J. Low Temp. Phys.* **106** (1/2) 101-131
- Whitaker D L, Weilert M A, Vicente C L, Maris H J and Seidel G M 1998a “Oscillations of charged helium II drops” *J. Low Temp. Phys.* **110** (1/2) 173-178
- Whitaker D L, Kim C, Vicente C L, Weilert M A, Maris H J and Seidel G M 1998b “Shape oscillations in levitated He II drops” *J. Low Temp. Phys.* **113** (3/4) 491-499
- Whitaker D L, Kim C, Vicente C L, Weilert M A, Maris H J and Seidel G M 1999 “Theory of the small amplitude shape oscillations of a helium-II drop” *J. Low Temp. Phys.* **114** (5/6) 523-545